Interaction of the STM tip with adatoms and molecules on metal surfaces: ab initio studies

Dissertation

zur Erlangung des akademischen Grades
doctor rerum naturalium (Dr. rer. nat.)
vorgelegt der
Mathematisch-Naturwissenschaftlich-Technischen Fakultät
(mathematisch-naturwissenschaftlicher Bereich) der
Martin-Luther-Universität Halle-Wittenberg

von Herrn **Kun Tao**
geb. am: 4 August 1976 in Anhui,
China

Gutachterin/Gutachter:

1. Prof. Dr. I. Mertig
2. Prof. Dr. W. Hergert
3. Prof. Dr. G. Pastor

Halle (Saale), den 12.12.2008 verteidigt am 12.10.2009

Contents

Zusammenfassung **1**

1 Introduction **3**

1.1 Theory of the STM 3
1.2 Manipulation of atoms and molecules with STM 6
  1.2.1 Positing single atoms with the STM 6
  1.2.2 Single molecule manipulation 8
1.3 Probing magnetic properties of adatoms and molecules with STM 10
  1.3.1 Probing magnetism of single adatoms 10
  1.3.2 Tailoring magnetic exchange coupling between adatoms 11
  1.3.3 Controlling magnetic properties of a single molecule 12
  1.3.4 Manipulating magnetism of a molecule by changing its structure . . 14

Goals of the work **18**

2 Methods of the calculation **21**

2.1 Density functional theory 21
  2.1.1 Hohenberg-Kohn Theorems 21
  2.1.2 Kohn-Sham equations 22
  2.1.3 LDA and GGA 23
2.2 Solving the Kohn-Sham equation 24
2.3 Pseudopotential methods 25
  2.3.1 Vienna Ab-initio Simulation Package (VASP) 25
  2.3.2 The SIESTA method 27
2.4 Nonequilibrium Green function method-Smeagol code 29
2.5 Molecular dynamics 31
  2.5.1 Many-body interatomic potentials 31
  2.5.2 Algorithm for atomic relaxation 32

3 Molecule-adatom junctions on a metal surface **35**

3.1 Interaction of magnetic atoms with a benzene molecule 35
3.2 Molecule-magnetic adatom sandwiches on Cu(001) 38
  3.2.1 Adsorption of a benzene molecule on a Cu(001) surface 39
  3.2.2 Single magnetic adatoms on Cu surfaces 40
  3.2.3 Benzene-adatom sandwich on Cu(001) 40
3.3 Manipulating magnetism of a molecule-adatom junction on a metal surface 45
  3.3.1 Vertical manipulation 46
  3.3.2 Lateral manipulation 51

4 Interaction of the STM tip with single adatoms on metal surfaces 53
4.1 Controlling the Kondo temperature with the STM tip: experimental motivation 53
4.2 Atomic-scale simulations and ab initio studies of the effect of the STM tip on the electronic properties of magnetic adatoms 56
4.3 Interaction between the STM tip and adatoms at the atomic scale: tailoring an adatom dynamics 61

5 Tailoring a single spin on metal surfaces by a magnetic STM tip 67
5.1 Description of ab initio calculations 68
5.2 Exchange interaction between the tip and adatoms 69
5.3 Spin-dependent charge transfer in the magnetic junction 73

Conclusions 81

Bibliography 83

Zusammenfassung

Die Wechselwirkung der magnetischen Spitze eines Rastertunnelmikroskops (RTM) mit Atomen und Molekülen auf metallischen Oberflächen wurde mit Hilfe der *ab initio* Rechnungen studiert. Alle Berechnungen wurden im Rahmen der Dichtefunktionaltheorie unter Berücksitigung der kompletten Systemrelaxation durchgeführt. Wir konzentrieren uns auf die Wechselwirkungen zwischen den einzelnen magnetischen Atomen adsorbierten auf metallischen Oberflächen und magnetischen bzw. nichtmagnetischen RTM-Spitzen. Das Zusammenspiel zwischen den Strukturrelaxationen und magnetischen Eigenschaften von einer einatomiger Junktion wurde aufgedeckt, das die experimentelle Ergebnisse hervorragend erklärt. Es wurde nachgewiesen, da"s die Ausrichtung des Spins vom einzelnen magnetischen Atom der 3*d*-Reihe kann mit Hilfe der RTM-Spitze durch Variation des Abstandes zwischen der RTM-Spitze und dem Substrat gesteuert werden. Es wurde festgestellt, da"s die Ursache für dieses Effekt die Austauschwechselwirkung zwischen der RTM-Spitze und dem adsorbierten Atom ist. Basierend auf der Methode der Nicht-Gleichgewicht-Greens-Funktionen haben wir die Berechnungen zum spinabhängigen Transport durchgeführt und bei kleineren Abständen zwischen der RTM-Spitze und dem Substrat einen Magnetowiderstandseffekt von etwa 70% beobachtet. Au"serdem haben wir unsere Untersuchungen auf Molekül-Atom-Sandwiches auf Metalloberflächen erweitert, wobei unsere Studien klar gezeigt haben, da"s der Magnetismus und die Leitfähigkeit in den Molekül-Atom-Junktionen mit Hilfe der RTM-Spitze beeinflu"st werden kann. Zum Beispiel, indem man den Abstand zwischen der RTM-Spitze und dem Substrat variiert, kann das magnetische Moment adsorbierten eines Co-atoms ein- und ausschalten werden.

The interaction of the scanning tunnelling microscopy (STM) tip with adatoms and molecules on metal surfaces is studied with *ab initio* calculations. All the Calculations are performed within the framework of the density functional theory in fully relaxations. We focus on the interaction between single magnetic adatoms on metal surfaces and magnetic or non-magnetic STM tip. The interplay between structural relaxations and magnetic properties of a single-atomic junction is revealed, which explains the experimental results very well. It is demonstrated that the spin direction of a single *3d* magnetic adatom can be controlled with a magnetic STM tip by varying the tip-substrate distance, the exchange interaction between the tip and the adatom is found to be the driving force for this effect. Based on the non-equilibrium Green function method, we perform spin-dependent transport calculations and find a magnetoresistance of about 70% at short tip-substrate distances. We also extend our studies to molecule-atom sandwiches on metal surface, our studies give clear evidence that magnetism and conductance in molecule-atom junctions can be tailored by the STM tip. Varying the tip-substrate distance the magnetic moment of the Co adatom can be switched on/off.

Chapter 1

Introduction

Since the invention of scanning tunneling microscopy (STM) by Binnig and Rohrer in 1981[1, 2], STM has become a powerful tool in the field of surface science, nanoscience and nanotechnology. It offered for the first time the possibility of direct, reals-space determination of surface structure in three dimensions. And it earned its inventors, G. Binnig and H. Rohrer, the Nobel Prize in Physics in 1986. Here, we briefly review the theory of the scanning tunneling microscopy/spectroscopy (STM/STS) and demonstrate that STS data are proportional to the calculated density of states of the tip and the sample as a function of the tip-substrate separation. It helps us to understand physics behind the observed experimental phenomena, and to compare the experimental data with the theoretical results obtained from the first principle calculations. In the chapter, we also concentrate on the interaction of the STM tip with adatoms and molecules on metal surfaces. Several important experiments on the electronic and magnetic properties of the adatoms and molecules are shortly reviewed. At first, we show the ability to manipulate a single atom and a molecule with the STM tip. Then, the possibility to tailor the magnetic properties of adatoms and molecules is demonstrated.

1.1 Theory of the STM

The physics of the STM is based on the quantum tunneling effect. In classic mechanics, an electron facing a potential barrier of an arbitrary form *U(x)* has no possibility to overcome it without obtaining an extra energy. According to quantum mechanics, the electron can directly tunnel through the potential barrier. The tunneling probability is described as :

$$T(E) \sim exp\left[-\frac{2}{\hbar}\int_{x_1}^{x_2}\sqrt{2m(U(x)-E)}dx\right] \tag{1.1}$$

where x_1 and x_2 bound the region of the nonzero barrier *U(x)*.

Fig.1.1 shows an energy level diagram for the system consisting of the sample and the tip[3]. When the tip and the sample are separated far away, they are independent and their vacuum levels are equal. The Fermi level of the sample and tip lie below the vacuum level E_{vacuum} by their respective work functions Φ_s and Φ_t, as shown in Fig.1.1 (a). If the STM tip and the sample are in thermodynamic equilibrium, their Fermi levels are equal, as shown in Fig.1.1 (b). When a voltage V is applied to the sample, its energy level will be rigidly shifted upward or downward in energy by the amount $|eV|$, depending on whether the polarity is negative or positive. With a positive bias, the net tunneling current arises

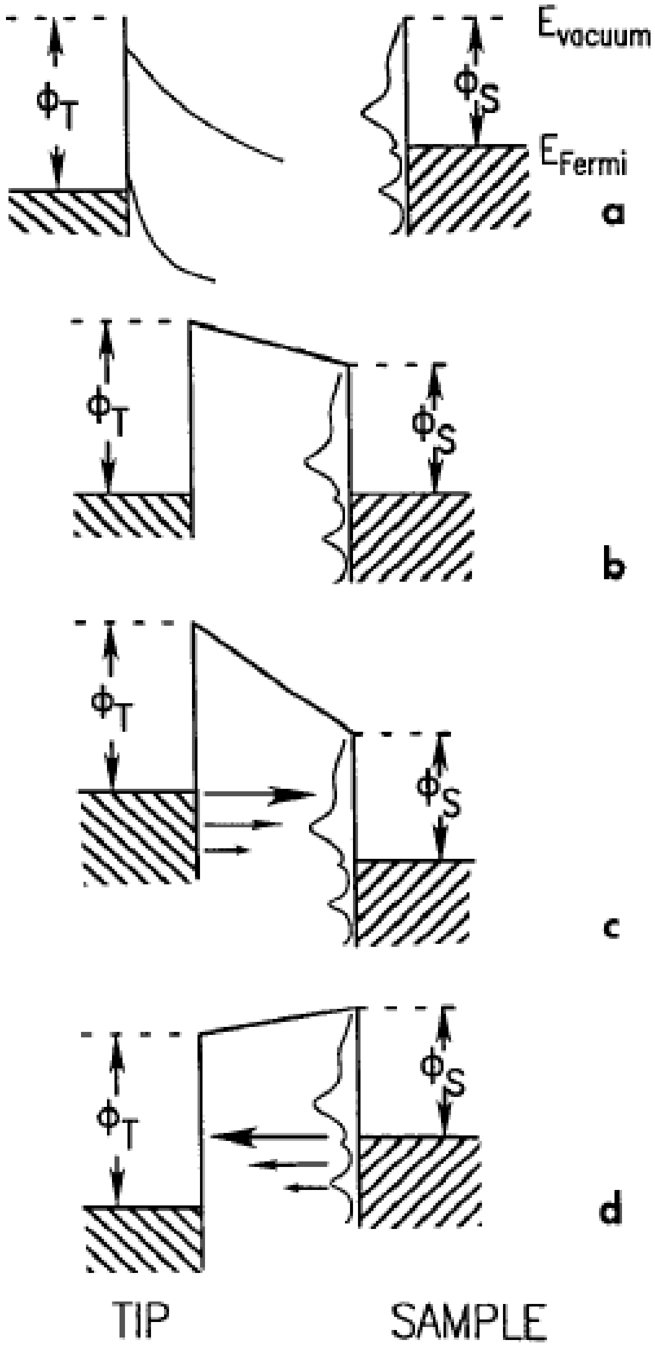

Figure 1.1: Energy level diagram for sample and tip. (a) Independent sample and tip. (b) Sample and tip at thermodynamic equilibrium, separated by small vacuum gap. (c) Positive sample bias: electrons tunnel from the tip to the sample. (d) Negative bias: electrons tunnel from the sample into the tip. The figure is adopted from [3].

from electrons that tunnel from the occupied states of the tip into the unoccupied states of the sample, as shown in Fig.1.1 (c). With a negative sample bias, the situation is reversed, and electrons tunnel from occupied states of the sample into the unoccupied states of the tip, as shown in Fig.1.1 (d).

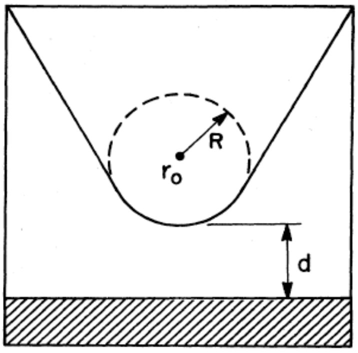

Figure 1.2: Schematic picture of tunneling geometry. Probe tip has arbitrary shape but is assumed locally spherical with radius of curvature R, where it approaches nearest the surface (shaded). Distance of nearest approach is d. Center of curvature of tip is labelled r_0. The figure is taken from [4]

.

Tersoff and Hamann proposed a simple model to describe the STM theoretically[4]. In their model, the tip is assumed to be spherical with radius of R at point r_0, as shown in Fig.1.2. The distance between the tip and the surface is d. The tunneling current is given in Bardeen's formalism by[5]:

$$I = \frac{2\pi e}{\hbar} \sum_{\mu,\nu} f(E_\mu)[1 - f(E_\nu + eV)] \left|M_{\mu\nu}\right|^2 \delta(E_\mu - E_\nu) \tag{1.2}$$

where *f(E)* is the Fermi function, V is the applied voltage, $M_{\mu\nu}$ is the tunneling matrix element between states Ψ_μ of the tip and Ψ_ν of the surface, and E_μ is the energy of state Ψ_μ in the absence of tunneling. The tip can be replaced by a point probe, following Tersoff and Hamann, which represents the idea of a nonintrusive measurement of the surface, with the maximum possible resolution. Matrix element and the tunneling current is proportional to the surface local density of states (LDOS) at the position of the tip.

To calculate matrix element $M_{\mu\nu}$, Bardeen has shown that[5]:

$$M_{\mu\nu} = \frac{\hbar^2}{2m} \int (\Psi_\mu^* \nabla \Psi_\nu - \Psi_\nu \nabla \Psi_\mu^*) \boldsymbol{ds} \tag{1.3}$$

where the integral is over any surface lying entirely within the vacuum region separating the two sides. To calculate $M_{\mu\nu}$, the sample (surface) wavefunction is expanded in the form

$$\Psi_\nu = \frac{1}{\sqrt{\Omega_s}} \sum_G a_G exp[z\sqrt{(\kappa^2 + \left|\mathbf{k}_\parallel + \mathbf{G}\right|^2)} + i(\mathbf{k}_\parallel + \mathbf{G}) \cdot \mathbf{x}] \tag{1.4}$$

Here Ω_s is sample volume, $\kappa = \hbar^{-1}\sqrt{2m\Phi_{sample}}$ is the minimum inverse decay length for the wavefunction in vacuum, Φ_{sample} is the work function, $\boldsymbol{k}_\parallel$ is the surface Bloch wave vector of the state, and $\boldsymbol{G}$ is a surface reciprocal-lattice vector.

The wavefunctions of the tip are taken to have the asymptotic spherical form

$$\Psi_{\mu} = \frac{1}{\sqrt{\Omega_t}} c_t \kappa R e^{\kappa R} \frac{1}{\kappa \left|\mathbf{r} - \mathbf{r}_0\right|} e^{-\kappa\left|\mathbf{r}-\mathbf{r}_0\right|} \tag{1.5}$$

where Ω_t is the tip volume. We assume for simplicity that work function Φ for the tip is equal to that of the surface.

Finally, Tersoff and Hamann obtained matrix elements:

$$M_{\mu\nu} = \frac{\hbar^2}{2m} 4\pi\kappa^{-1} \frac{1}{\sqrt{\Omega_t}} \kappa R e^{\kappa R} \Psi_{\nu}(\mathbf{r}_0) \tag{1.6}$$

and the tunneling current:

$$I = \frac{32\pi^3 e^2}{\hbar} V \rho_{tip}(E_F) \frac{\phi^2}{\kappa^4} R^2 e^{2\kappa R} \rho_{sample}(\mathbf{r}_0, E) \tag{1.7}$$

where $\rho_{tip}(E_F)$ is the density of states per unit volume of the tip, and $\rho_{sample}(\mathbf{r}_0, E)$ is the surface local density of states at the point r_o. Note that in the formula the tunneling current exponentially depends on the tip-surface separation. Therefore, a small change in the tip-adatom distance would induce a strong increase in the tunneling current, which will be discussed in detail later.

1.2 Manipulation of atoms and molecules with STM

STM can be used to fabricate nanostructures, which was demonstrated for the first time by Eigler and Schweizer. Nowadays, atomic manipulation is an ordinary experiment technique employed in a large number of studies[6, 7, 8, 9, 10, 11, 12, 13, 14, 15, 16, 17, 18, 19, 20].

1.2.1 Positing single atoms with the STM

The tip of the STM always exerts a finite force on an adsorbed atom. The force contains both Van der Waals and electrostatic contributions. Both of the magnitude and the direction of the force can be tuned by adjusting the position and the voltage of the tip. There are two procedures of the STM manipulation: lateral manipulation and vertical manipulation. Generally, it requires less forces to move an atom along a surface (lateral manipulation) than to pull it away from the surface (vertical manipulation). Thus it is possible to use the STM tip to pull the atom across the surface while the atom still remains bound to the surface. Therefore, special nanostructures can be fabricated with the STM.

Eigler and Schweizer[7], for the first time, used the STM at low temperature to control the position of individual xenon atoms on a single-crystal nickel surface and formed the logo of the IBM company. They placed the tip directly above the xenon atom to be moved, then lowered the tip towards the atom to increase the interaction between the tip and the atom until attractive forces between them are sufficient large to keep the atom located beneath the tip when the tip is subsequently moved across the surface. The atom was dragged to the desired destination. Then the tip was withdrawn by reducing the tunnel current, which effectively terminates the attraction between the atom and the tip, leaving the xenon atom bound to the surface at the desired location. Repeating the procedure several times, a new nanostructure was fabricated, as shown in Fig.1.3. With the method, it is possible to construct nanostructures on our own design, atom by atom. Different shapes of the nanostructure on flat surface has been made with such method.

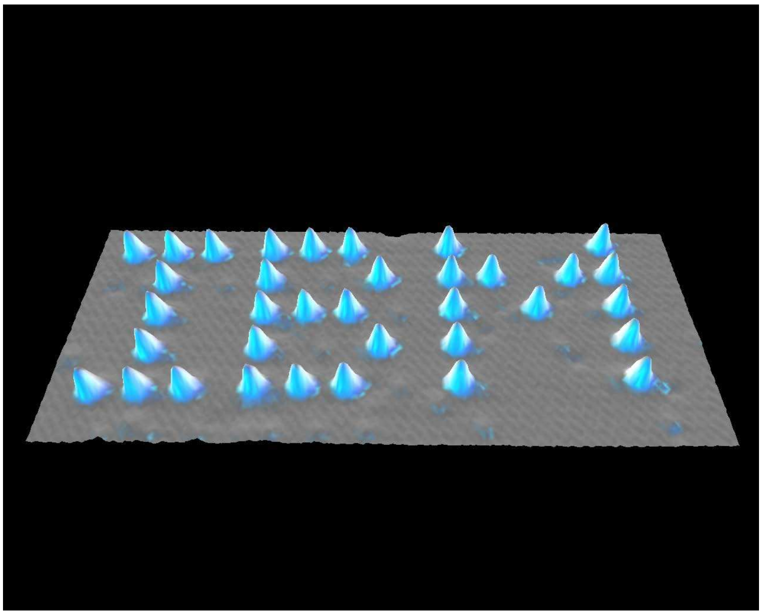

Figure 1.3: Xenon atom on a Ni(110) surface at low temperature 4 K. Each letter is 50 Å from top to bottom. The figure is adopted from [7].

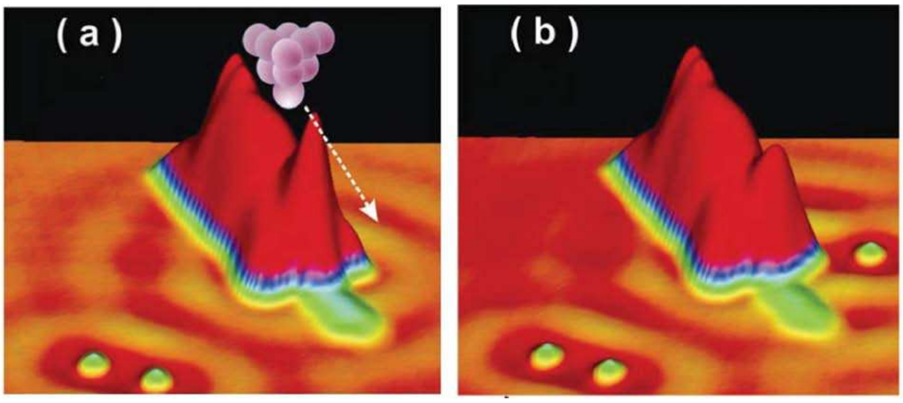

Figure 1.4: Atom extraction. (a) A 3D STM image of a silver nanocluster deposited by tip-surface contact. The tip is brought close to the protruded part of the cluster and then moved laterally towards a destination on the surface. (b) The STM image acquired after this shows a height reduction of the cluster protrusion and the extracted atom on the surface destination. The figure is taken from [21].

Recently, Deshpande *et al.*, demonstrated the ability of extraction and manipulation of individual atoms on three dimensional nanoclusters [21]. A silver cluster was deposited on a large terrace on a Ag(111) surface. The irregularities in the cluster, seen as protrusions in three-dimensional images, were chosen to be the ideal target zone to extract the atoms with ease, as shown in Fig.1.4 (a). For the atom extraction, the tip was initially positioned near a protrusion of the cluster, and the tip height was then reduced to increase the tip-cluster interaction. The tip was laterally moved from one side of the cluster towards the terrace for a short distance in constant current mode. Fig.1.4 (b) shows the STM image after the manipulation confirming the successful atom extraction. The atom-extraction process is different from the atom manipulation on a flat surface because it involves removing the topmost cluster atom and then moving it along a rough terrain on a three-dimensional cluster surface. Combined total energy calculations and molecular dynamics, it was demonstrated that the energy barrier for a silver atom to diffuse over the Ag(111) step edge was greatly reduced (less than 50 meV) during approaching the tip to the cluster. The work of Deshpande *et al.,* not only provided a fundamental understanding of the influence of distance-dependent tip-cluster interaction but also opens a novel route to produce single atoms for future nanoscale experiments or for atomistic constructions.

1.2.2 Single molecule manipulation

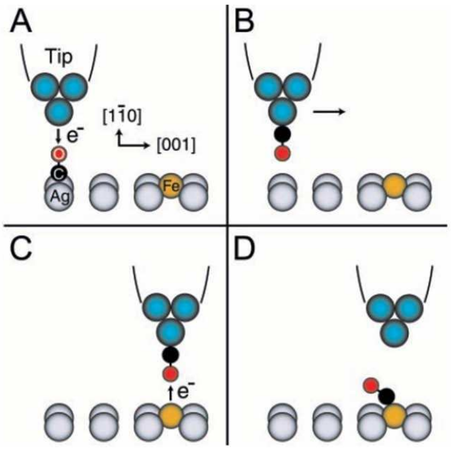

Figure 1.5: Schematic diagrams showing the different steps in the formation of a single bond with the STM. The binding sites are determined by imaging the adsorbed species with a CO molecule attached to the tip. The sizes of the circles are scaled to the atomic covalent radii. A) The tip is positioned over a single CO molecule to induce the detachment of CO from Ag and its bonding to the tip. Because CO forms a bond predominantly through the carbon, a 180^o rotation of the CO occurs in the transfer. (B) The tip with the attached single CO molecule is translated (indicted by the arrow) and positioned over an Fe atom. (C) The bias voltage and the flow of electrons are reversed, inducing the transfer of CO from the tip to the Fe. (D) A single Fe-CO bond is formed. The figure is taken from [22].

STM allows to manipulate single molecules adsorbed on surfaces in the same way as it is performed for adatoms. STM/STS can provide an insight into the properties of molecules

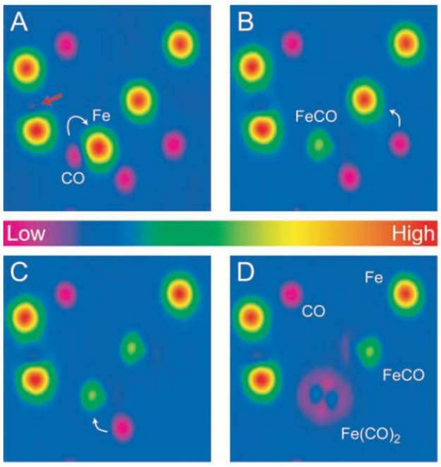

Figure 1.6: A sequence of STM topographical images recorded at U = 70 mV and I = 0.1 nA tunneling current, and 13 K to show the formation of Fe-CO bond with the prescribed method (Fig.1.5). The size of each image is 63 Å by 63 Å. Fe atoms image as protrusions and CO molecules as depressions. The white arrows indicate the pair of adsorbed species involved in each bond formation step. (A) Five Fe atoms and five CO molecules are adsorbed in this area of the Ag(110) surface. One CO is very close to an Fe atom (indicated by the red arrow). (B) A CO molecule has been manipulated and bonded to an Fe atom to form Fe(CO). (C) Another Fe(CO) is formed by binding CO to a second Fe atom. (D) An additional CO has been bonded to Fe(CO) to form $Fe(CO)_2$. A 180^o flip is observed for the remaining Fe(CO). The figure is adopted from [22].

governed by quantum effects, like bonding, adsorption orientation, and magnetic properties [19, 22, 23, 24, 25, 26, 27, 28, 29].

Vibrational spectroscopy is a powerful tool for the analysis of molecules adsorbed on surfaces. Knowledge of the active vibrational modes of a molecules, as well as the vibrational energies, can lead to an understanding of its adsorption site, orientation, and changes in bonding upon adsorption. The vibrational spectra can be obtained from molecules adsorbed at the buried metal-oxide interface of a metal-oxide-metal tunneling junction[30]. However, it is difficult to characterize the molecule because it is buried within the junction in a complex environment.

The metal-oxide-metal junction can be replaced by a STM tunnel junction: a sharp tip, a vacuum gap of several angstroms, and a surface with the adsorbed molecules[19]. The combination of atomic resolution and vibrational spectroscopy also allows the creation of atomic-scale spatial images of the inelastic tunneling channel for each vibrational mode, in a manner similar to that used to map out the electronic density of state with the STM. Lee *et al.,* used a STM to manipulate the bonding of a carbon monoxide (CO) molecule on an iron (Fe) adatom on silver (110) surface and to analyze the structure and vibrational properties of individual products[22]. They positioned the tip over a single CO molecule, with a vertical manipulation, the molecule was transferred from the surface to the STM tip, then with the lateral manipulation the molecule is bonded with an Fe atom forming Fe(CO) complex, as shown in Fig.1.5. A second CO molecule was similarly transferred and bonded with Fe(CO) to form $Fe(CO)_2$, see Fig.1.6. Using the single-molecule vibrational spectra, the C-O stretch of Fe(CO) and Fe(CO)$_2$ was obtained, and the isotope effect can also be distinguished. The ability to control step-by-step bond formation of adsorbed chemical species at the single-molecule level provides a real-space understanding and direct visualization of the nature of the chemical bond.

1.3 Probing magnetic properties of adatoms and molecules with STM

There are a lot of experimental techniques allowing to probe an average magnetism of the surface system. STM/STS provides an unique possibility to access local magnetic properties of single adatoms, small clusters and molecules. Here we describe techniques exploiting the Kondo effect.

The Kondo effect appears[31] when a magnetic atom is put in a nonmagnetic metal host forming a smallest magnetic structure. The Kondo effect is caused by the coupling between spins of the impurity magnetic atom with spins of the surrounding conduction electrons. At high temperature, the spins of the conduction electrons in the host metal weakly interact with the spin of the impurity magnetic atom. For temperature below a characteristic Kondo temperature (T$_K$), there is a strong coupling between the spins of the impurity atom and the spins of the surrounding host metal, and the magnetic moment of the impurity magnetic atom is screened entirely by the spins of the electrons in the host metal.

1.3.1 Probing magnetism of single adatoms

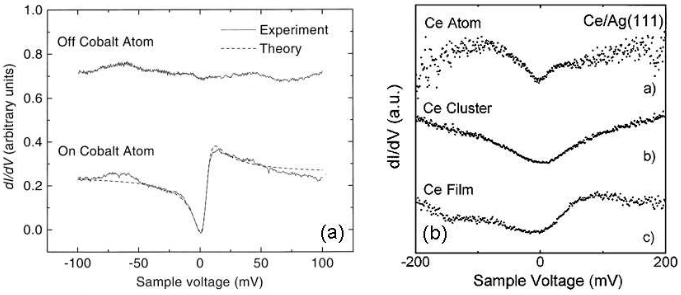

Figure 1.7: (a) A pair of dI/dV spectra taken with the STM tip held over a single Co atom and over the nearby bare Au surface. The feature identified as a Kondo resonance appears over the Co atom (the ratio of the amplitude of the resonance feature to the overall conductivity is 0.3). Dashed curve shows a fit to the data with a modified Fano theory, the figure is taken from [32]. (b) dI/dV spectra: (a) on a single Ce adatom at T = 5 K, (b) on a Ce cluster at T = 50 K, and (c) on a Ce film of more than 10 monolayer thickness at T = 50 K. Tunneling parameters prior to opening the feedback: (a) V = 200 mV, I = 0.1 nA, (b) V = 500 mV, I = 1 nA, (c) V = 350 mV, I = 1 nA. The figure is adopted from [33].

For the first time the Kondo resonance on a single magnetic adatom on metal surface was observed by Madhavan *et al.*, [32] for Co on Au(111) and Li *et al.*, [33] for Ce on Ag(111). Their STM/STS studies of individual magnetic atoms coupled to the nonmagnetic substrate demonstrated a spectral feature with an asymmetric line shape at the Fermi level, that was identified as the Kondo resonance (an example of such a feature is demonstrated in Fig.1.7.). The non-Lorentzian shape of the feature was understood as a Fano resonance for an interacting discrete state coupled to a continuum of conduction electrons [33, 32]. Theory unambiguously linked the shape of Fano resonance to the Kondo temperature of the system, i.e. the energy difference between the correlated singlet and the corresponding doubled states [34]. Madahavan *et al.*, obtained the Kondo temperature equal to 70 K for Co on Au(111) [32]. Experiments performed for Co on Cu(111) and Cu(001) yield comparable values ≈ 54 K and 88 K respectively [13, 35]. Both for Cu(001) and Cu(111) systems, the Kondo resonance is detectable only close to the adatoms for $r < 10$ Å, indicating that the electrons of the Cu(111) surface state play only a minor role in forming the Kondo resonance [35]. However, the surface state confinement in the elliptical resonator was demonstrated to cause the coherent projection of the Kondo resonance at the Co atom placed in the ellipse focus onto the empty focus[13, 36] , as shown in Fig.1.8 and Fig.1.9.

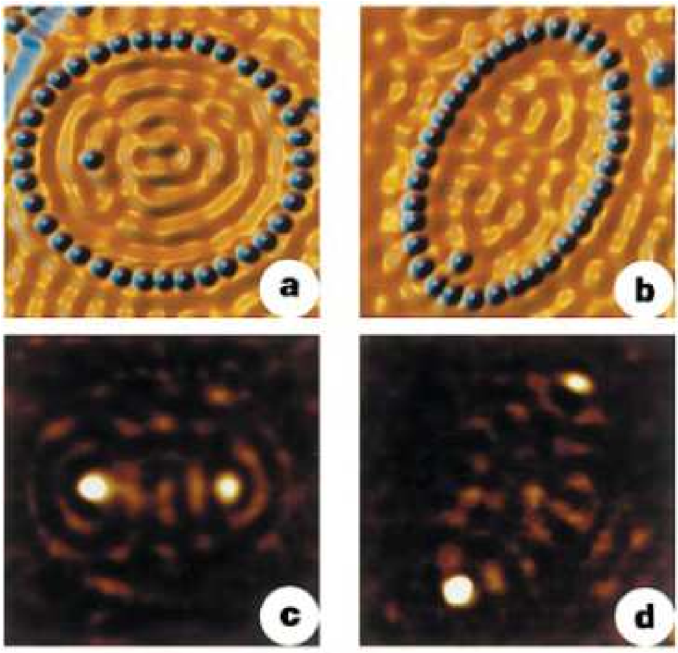

Figure 1.8: (a), (b), Topographs showing the e=1/2 (a) and e=0.786 (b) ellipse each with a Co atom at the left focus. (c), (d), Associated dI/dV difference maps showing the Kondo effect projected to the empty right focus, resulting in a Co atom mirage. The figure is adopted from [13].

1.3.2 Tailoring magnetic exchange coupling between adatoms

The Kondo effect can be utilized to determine the exchange interaction between adatoms on surfaces. The indirect RKKY coupling between adatoms is involved in the formation of the correlated singlet state[37, 38, 39]. Theory predicts several realizations of such a problem depending on the adatom-adatom exchange interaction value J. A new correlated state with the new Kondo temperature $T'_K = (T_K)^2/|J|$ appears when the ferromagnetic (FM) interaction J between two adatoms is much stronger than the Kondo binding energy $k_B T_K$ [11, 38]. This phenomenon was reported by Chen et al., for Co dimers on Au(111) substrate [11]. They observed abrupt disappearance of the Kondo resonance when Co-Co

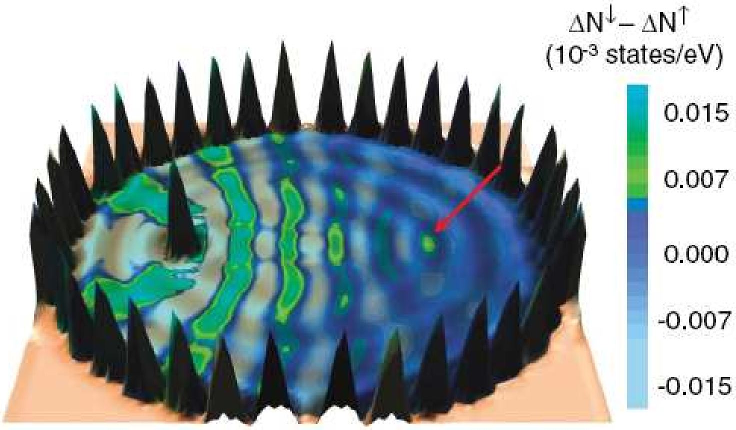

Figure 1.9: The LDOS at the Fermi energy on the Co adatom and the Co atoms of the corral walls are shown. The spin polarization of surface-state electrons inside the Co corral is presented in color: $\Delta N \uparrow$ and $\Delta N \downarrow$ are determined by the difference between LDOS near the Fermi energy (+10 meV) of the Co corral with the Co adatom, the empty Co corral, and the single Co adatom on the open Cu(111). The mirage in the empty focus is marked by the red arrow. The geometrical parameters of the corral are the same as in the experimental setup of , i.e., semiaxis a=71.3 Å and eccentricity ε=0.5. The figure is taken from [36].

separation became less than 6 Å. Recent investigations of Wahl et al [37]., have provided a better insight in the matter of the problem, as shown in Fig.1.10. Oscillating behavior of RKKY interaction between two Co adatoms on Cu(100) substrate permits to obtain the antiferromagnetically (AFM) coupled Co dimer at certain separation [37]. If the antiferromagnetic interaction J is very strong, a net dimer singlet state is formed abolishing the Kondo effect [38, 39, 40]. Intermediate AFM coupling results in the split of the Kondo resonance, so a singlet state is formed between the impurities and two peaks at energies $\pm J/2$ arise in the impurity density of states [39]. Even for smaller antiferromagnetic interactions a single-impurity Kondo resonance is recovered but its width is increased. Wahl et al. clearly demonstrated that the exchange interaction value could be extracted from Fano resonances in STS spectra. Their experimental values for Co on Cu(100) are reported to be in a very good agreement with *ab initio* calculations. *Ab initio* calculations predicted that the exchange interaction between magnetic impurities on noble metal substrates at large adatom-adatom separations is mediated by surface states electrons [36], but to our knowledge no experiments have been conducted yet.

1.3.3 Controlling magnetic properties of a single molecule

Recently, Iancu *et al.,* demonstrated that the Kondo temperature of a single molecule can be tuned by changing the conformation of the molecule with a STM[41]. The TBrPP-Co (where TBrPP is 5,10,15,20-tetrakis(4-bromophenyl)porphyrin) molecule is composed of a porphyrin unit with a Co atom caged at the center and four bromophenyl groups at the end part. It has two conformations: saddle (the adsorption height of the center part is higher than other parts) and planar (the surface of the molecule is parallel to the substrate), as shown in Fig.1.11. The interaction between the spin of the cobalt atom and free electrons

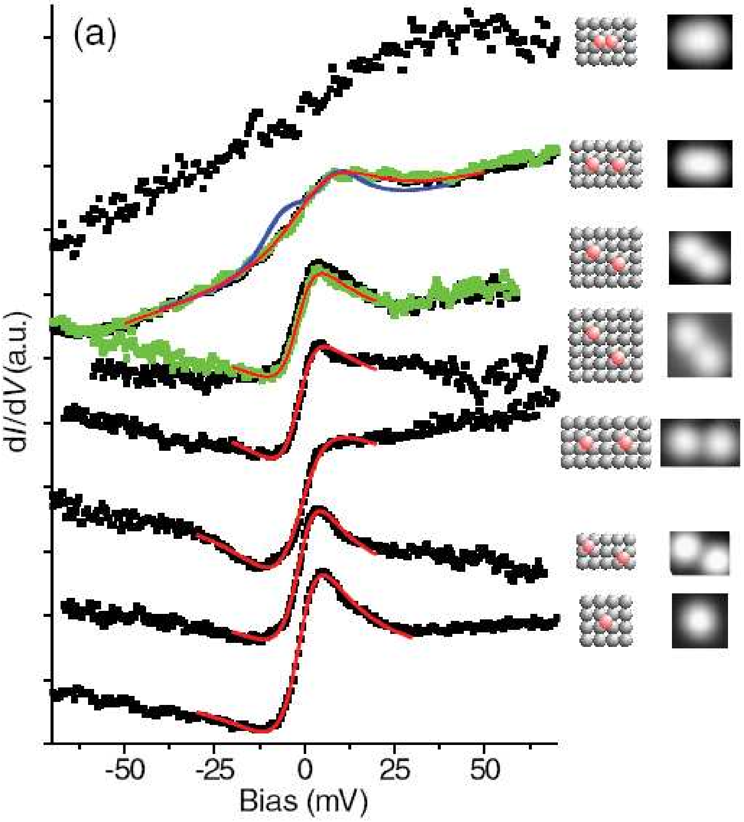

Figure 1.10: Kondo resonance of cobalt dimers on Cu(100) measured by STS at 6 K. As a consistency check, spectra taken on both ends of the dimers are shown (green and black dots) to be equivalent. (a) Model, topography, and spectra for (from top to bottom) a compact dimer (2.56Å), a dimer at 5.12, at 5.72, at 7.24, at 7.68, at 8.10Å, and for a single adatom at infinite distance ($>$ 20Å) are depicted. The spectra are shown together with fits of a Fano function (red solid line), for the dimer at 5.12Å also a simulated curve with J=15 meV and $\Gamma = 1.2T_K^0$ is plotted (blue solid line). For the dimer at 5.12Å, a linear background had to be taken into account to obtain a reasonable fit for a Fano function (spectra shifted vertically for clarity). The figure is adopted from [37].

from the Cu(111) substrate can cause a Kondo resonance. Two conformations of isolated single TBrPP-Co molecules on a Cu(111) surface are switched by applying +2.2 V voltage pulses from a STM tip at 4.6 K. Tunneling spectroscopy data reveal that switching from the saddle to the planar molecular configuration enhances spin-electron coupling, which increases the associated Kondo temperature from 130 to 170 K.

Nearly one year later, Hla *et al.*, has grown the TBrPP-Co molecule (planar conformation) on Cu(111) surface, which self-assembled molecule ribbon on the surface[42] (see Fig.1.12). As we know, the Kondo temperature is related to the density of the conducting electrons ρ and the exchange coupling J at the magnetic impurity as:

$$T_K \propto exp[-(1/\rho J)] \tag{1.8}$$

Thus, variation of ρ or J or both would change the Kondo temperature. The center TBrPP-Co molecule is surrounded by six neighbors (see Fig.1.12). By removing the nearest neighbor

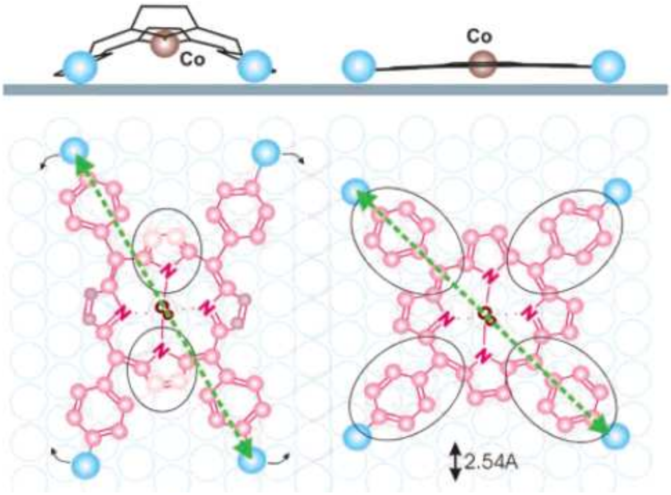

Figure 1.11: Two conformations of the TBrPP-Co molecule: saddle (left) and planar (right). Blue and pink color balls represent bromine and carbon atoms, respectively. The figure is taken from [41].

molecules one by one, from 6 to 0, the center molecule is increasingly exposed to the surface state electrons. This should increase ρ, and thus the associated Kondo temperature should rise.

1.3.4 Manipulating magnetism of a molecule by changing its structure

The ability to control and manipulate individual spins and the coupling of single spins to their environment is at the basis of prospective quantum technologies, where miniaturization reaches the atomic level. Recently, Wahl *et al.,* demonstrated the ability to tune the coupling between the spin of individual cobalt adatoms with their surrounding by controlled attachment of molecular ligands[43]. It has been demonstrated that it is possible to put carbon monoxide molecule on magnetic atoms, as shown in Fig.1.5. By increasing the number of ligand CO molecules on a Co adatom from two to four, the Kondo temperature changes from 88 K for a single Co adatom to 283 K for $Co(CO)_4$ complex, as shown in Fig.1.13. Since the Kondo resonance is a signature of the spin of the complexes, it can be exploited as a sensor for its magnetic properties. The behavior of the Kondo temperature of the complexes as a function of the number of ligands can be understood in the Kondo model. The bonds between the CO molecules and the cobalt adatom would increase the coupling to the substrate conduction electrons. Therefore the Kondo temperature increases with the number of ligand CO molecules.

Zhao *et al.,* demonstrated that the Kondo temperature of a cobalt phthalocyanine (CoPc) molecule adsorbed on a Au(111) surface can be controlled by modifying the structure of the molecule[44]. In experiments, they cut eight hydrogen atoms away from the molecule with voltage pulses from a STM tip (dehydrogenation process, as shown in Fig.1.14), and the center of the dehydrogenated CoPc (d-CoPc) molecule increase 0.8 Å in height. A very strong Kondo resonance appears near the Fermi level for the d-CoPc molecule, see Fig.1.15. In theoretical calculations, the magnetic moment of the CoPc molecule is quenched to 0 μ_B when it adsorbs on the Au(111) surface. After dehydrogenation process, four lobes of the molecule chemically bond to the gold substrate and the magnetic moment of the d-CoPc

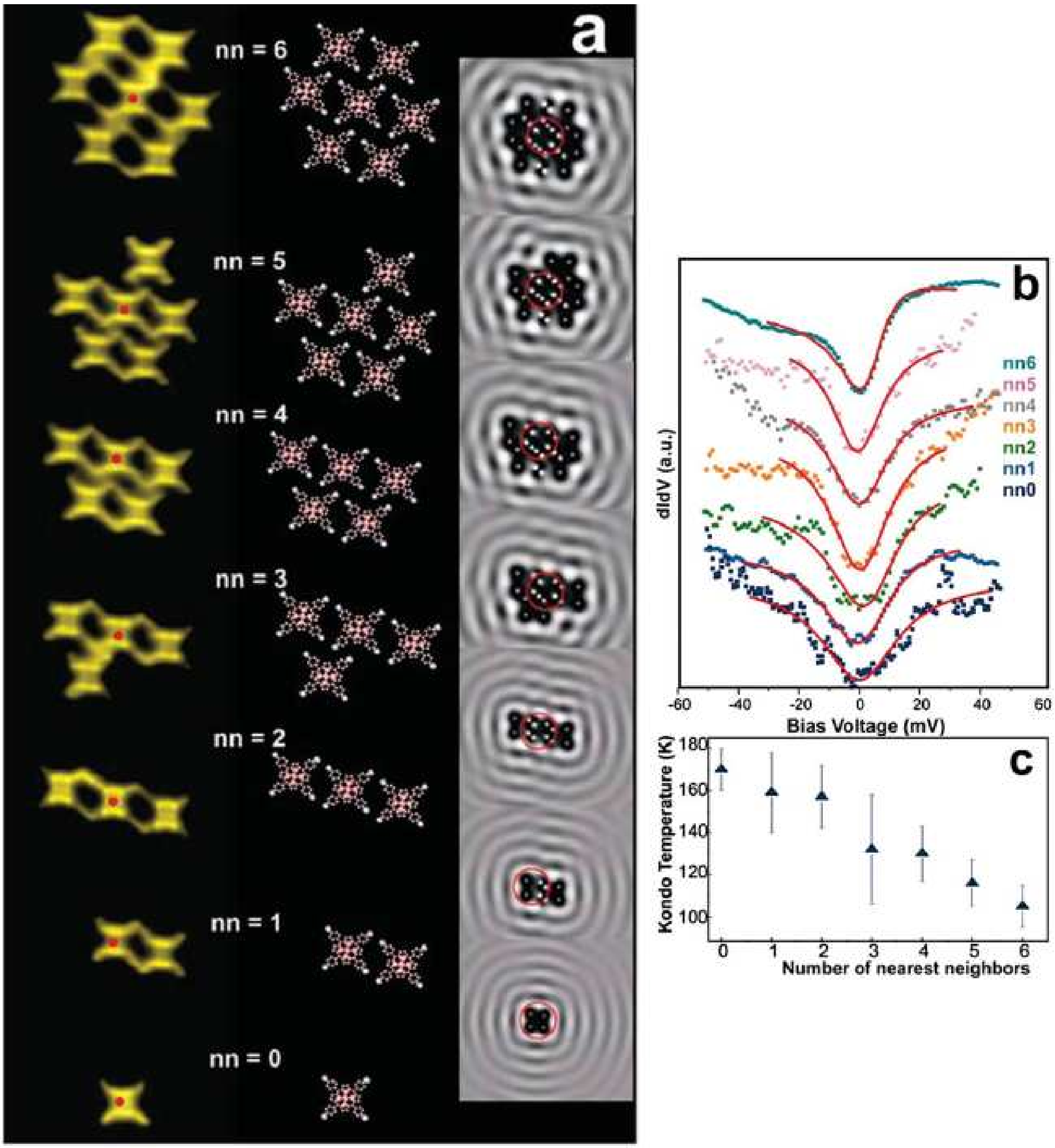

Figure 1.12: Kondo temperature tuning. (a) A sequence of STM images of different nn molecules created by removing one molecule at a time with the STM tip (left) from the hexagon and corresponding models (middle). The calculated electron standing wave patterns reveal a gradual exposing of the center molecule (indicated with a red circle) to the surface state electrons. Here white and black colors in the calculated images represent higher and lower electron densities, respectively. The black region under the molecular clusters indicates a reduction of surface electronic charge density. (b) The dI/dV spectra are measured at each step by positioning the tip above the center molecule (indicated with red dot). The spectra are vertically and horizontally displaced for clarity. Horizontal displacements of 3 to 10 meV are taken for the spectra representing nn6, nn5, nn4, nn2, and nn1. (c) The plot of Kondo temperature as a function of the number of nearest neighbors. The figure is taken from [42].

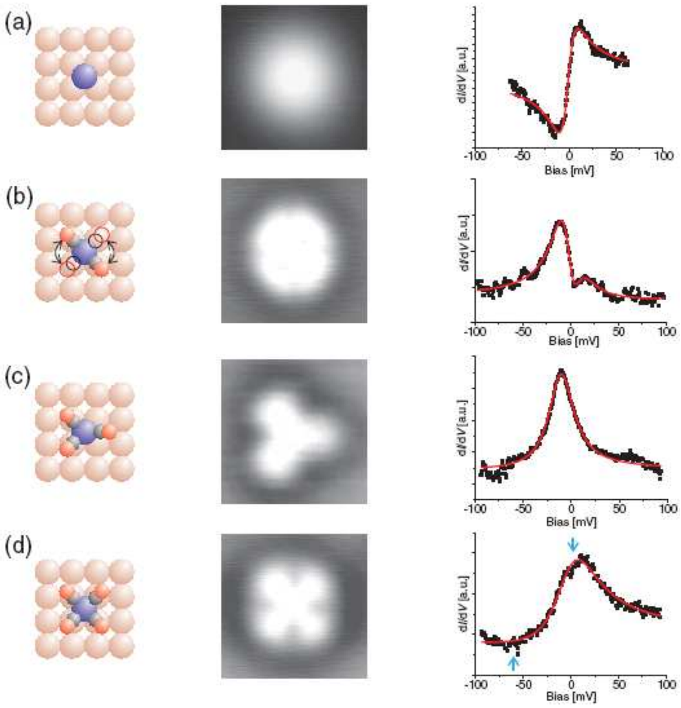

Figure 1.13: Models, STM topographies, and STS spectra in the center of the Co adatoms and complexes under investigation: (a) Cobalt adatom, (b) $Co(CO)_2$ (constantly flipping; from the spectrum a linear background has been removed), (c) $Co(CO)_3$, (d) $Co(CO)_4$. Models and topographies in (a)-(d) drawn to the same scale. The solid lines in the spectra are fits of a Fano function. The figure is adopted from [43].

molecule is nearly recovered to that of its free standing state. This paper demonstrates an ability to change the magnetic states of a molecule by directly modifying its structure via single-molecule manipulation and it gives direct microscopic evidence of how specific, well-characterized molecule contact configuration leads to different electronic and spin behaviors. Later on, a number of studies dealing with MPc (where M denotes magnetic atom) molecules have been performed[45, 46, 47, 48].

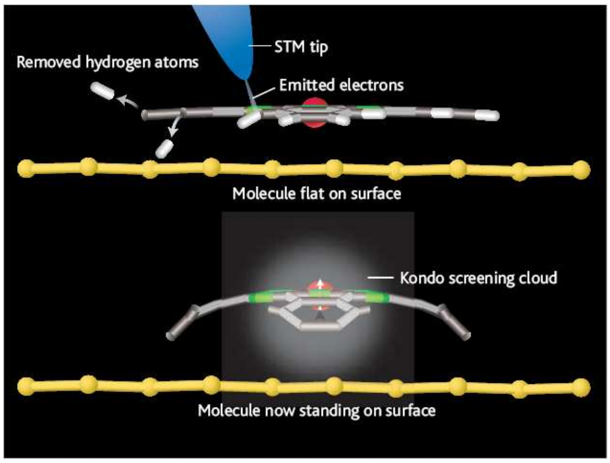
STM tip
Removed hydrogen atoms
Emitted electrons
Molecule flat on surface
Kondo screening cloud
Molecule now standing on surface

Figure 1.14: (Top) An STM tip is used to snip hydrogen atoms from a single cobalt phthalocyanine (CoPc) molecule lying on a gold surface. (Bottom) The trimmed molecule protrudes from the surface and is surrounded by a cloud of electrons that represent the Kondo screening cloud about the cobalt ion spin. The figure is taken from [49].

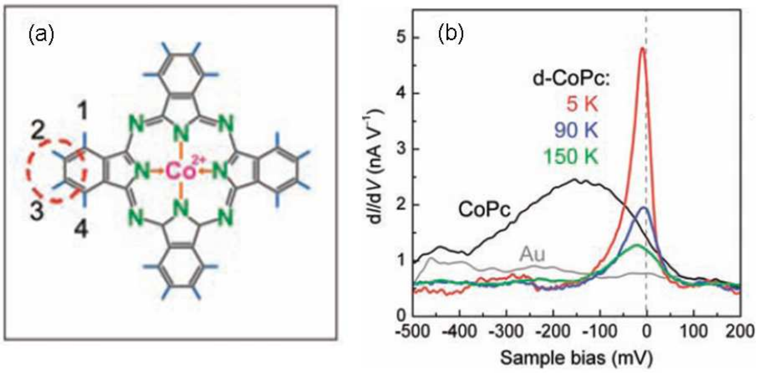

Figure 1.15: (a) Structural formula of the CoPc. Hydrogen atoms 2 and 3 of one lobe were dissociated in our experiments. (b) Kondo resonance of d-CoPc at different temperatures. Typical dI/dV spectra measured at the center of a CoPc molecule at 5 K (black line), showing a d_Z^2 orbital-mediated tunneling resonance, and a d-CoPc molecule at 5, 90, and 150 K (colored lines), showing strong resonance near E_F. Spectra from bare Au(111) (gray line) is shown for comparison. The figure is adopted from [44].

Goals of the work

In this work we concentrate on the interaction of the STM tip with adatoms and molecules on metal surfaces.

The following problems are addressed:

- The effect of the STM tip on electronic and magnetic properties of the magnetic adatoms and molecules on metal surfaces.
- The effect of the STM tip on an atomic diffusion on surfaces.
- The possibility to manipulate single spins on metal surfaces by a spin polarized STM tip.
- Interplay between structure and magnetism in a single atom junction.

Chapter 2

Methods of the calculation

2.1 Density functional theory

During two past decades, computer simulations, which are based on a quantum-mechanical description of interactions between atoms have strongly influenced the development of material science. All the calculations presented in this work are based on the density function theory (DFT). DFT is a quantum mechanical theory used in physics and chemistry to investigate the electronic structure (principally the ground state) of many-body systems, in particular atoms, molecules and condensed phases. Within this theory, the properties of a many-electron system can be determined by using functionals, i.e. functions of another function, which in this case is the spatially dependent electron density. The DFT has been proposed in 1960s by Hohenberg, Kohn and Sham [50, 51]. This theory is based on two theorems, which demonstrate that electron density $\rho(\mathbf{r})$ plays a central role and can be used as a fundamental variable for the description of any many-body electronic system. Within the framework of the DFT, the intractable many-body problem of interacting electrons in a static external potential is reduced to a tractable problem of non-interacting electrons moving in an effective potential. Usually DFT calculations for solid-state systems describe experimental data quite satisfactorily. Quantum-mechanical many-body effects are taken into account using different exchange-correlation potentials. Since the exact form of exchange-correlation potential is not known, there are several approaches for its construction. In this work, two wide-spread approaches are used: local-density approximation (LDA) and generalized-gradient approximation (GGA).

2.1.1 Hohenberg-Kohn Theorems

Following Ref. [50], below we concentrate on a system of N electrons confined in a volume at the presence of an external potential $v(r)$. The Hamiltonian of this system $\hat{H}$ takes the following form:

$$\hat{H} = \hat{T} + \hat{V} + \hat{U}, \tag{2.1}$$

where $\hat{T}$ is the operator of kinetic energy, $\hat{V}$ is the operator of interaction energy of the electron gas and the external potential $v(r)$, $\hat{U}$ is the operator of electron-electron (Coulomb) interaction:

$$\hat{T} = -\sum_{i}^{N} \nabla^2, \tag{2.2}$$

$$\hat{V} = V(\mathbf{r}), \tag{2.3}$$

$$\hat{U} = -\sum_{i \neq j}^{N} \frac{1}{|\mathbf{r}_i - \mathbf{r}_j|}, \tag{2.4}$$

The following system of atomic units are used: $\hbar$=1, m_e=0.5, e^2=2 and a_0=0.5292 $\mathring{A}$ - Bohr radii.

According to the first theorem the total energy E of the ground state of an arbitrary electronic system is a universal functional $E[\rho]$ of the electronic density $\rho(\mathbf{r})$. Additionally, one can always separate the term responsible for the interaction of electronic gas with the external potential $v(\mathbf{r})$ from $E[\rho]$:

$$E[\rho] = \int d\mathbf{r} v(\mathbf{r})\rho(\mathbf{r}) + F[\rho], \tag{2.5}$$

where $F[\rho]$ is the functional of $\rho(\mathbf{r})$ only. $E[\rho]$ equals to the ground-state energy E_0 for the correct $\rho(\mathbf{r})$.

According to the second theorem, $E[\rho]$ assumes its minimum for the correct value of $\rho(\mathbf{r})$, if the admissible functions are restricted by the condition:

$$N[\rho] \equiv \int d\mathbf{r}\rho(\mathbf{r}) = N, \tag{2.6}$$

here N is the total number of particles in the system.

Let us denote (i) $\rho_0(\mathbf{r})$ - the electronic density of the ground state of the system of N electrons in an external field $v(\mathbf{r})$ and (ii) $\hat{F} = \hat{T} + \hat{U}$. Then two following conditions are satisfied [52]:

$$\int d\mathbf{r} v(\mathbf{r})\rho(\mathbf{r}) + F[\rho] \geq E_0, \tag{2.7}$$

$$\int d\mathbf{r} v(\mathbf{r})\rho_0(\mathbf{r}) + F[\rho] = E_0. \tag{2.8}$$

Thus, electronic density of the ground state $\rho_0(\mathbf{r})$ is defined by minimization of the functional (2.5). The electronic density corresponding to the minimal value of the total energy of the system E_0 is the electronic density of the ground state.

2.1.2 Kohn-Sham equations

Two theorems discussed in the previous section are very important, since they allow to reduce an intractable many-body problem of interacting electrons in a static external potential to a tractable problem of non-interacting electrons moving in an effective potential. According to the results of the previous section, our goal is to minimize $E[\rho]$. Taking μ as a Lagrange coefficient, and using (i) condition (2.7) and (ii) the functional minimization principle [53], we obtain the Euler equation

$$\frac{\delta E[\rho]}{\delta \rho(\mathbf{r})} = \mu. \tag{2.9}$$

Since the explicit form of the functional $E[\rho]$ is unknown, let us transform it to the following form

$$E[\rho] = T_s[\rho] + \frac{1}{2}\int d\mathbf{r}d\mathbf{r}'\frac{\rho(\mathbf{r})\rho(\mathbf{r}')}{|\mathbf{r}-\mathbf{r}'|} + \int d\mathbf{r}v(\mathbf{r})\rho(\mathbf{r}) + E_{xc}[\rho], \tag{2.10}$$

here T_s is the functional of kinetic energy of non-interacting electronic gas, the second term describes electron-electron Coulomb interactions, the third term-interactions with the external potential, the fourth term, so called exchange-correlation functional is defined as:

$$E_{xc}[\rho] = F[\rho] - T_s[\rho] - \frac{1}{2}\int d\mathbf{r}d\mathbf{r}'\frac{\rho(\mathbf{r})\rho(\mathbf{r}')}{|\mathbf{r}-\mathbf{r}'|}. \tag{2.11}$$

This equation is derived from Eq.(2.5), if one picks out Coulomb and kinetic energy from $F[\rho]$. The Euler equation (2.9) takes the following form:

$$\frac{\delta T_s[\rho]}{\delta\rho(\mathbf{r})} + v_{eff}(\mathbf{r}) = \mu, \tag{2.12}$$

where

$$v_{eff}(\mathbf{r}) = v(\mathbf{r}) + 2\int d\mathbf{r}\frac{\rho(\mathbf{r})}{|\mathbf{r}-\mathbf{r}'|} + v_{xc}(\mathbf{r}), \tag{2.13}$$

$$v_{xc}(\mathbf{r}) \equiv \frac{\delta E_{xc}[\rho]}{\delta\rho(\mathbf{r})}. \tag{2.14}$$

Formulae (2.12) is the equation for non-interacting particles in an external potential $v_{eff}(\mathbf{r})$. Thus, considering $v_{eff}(\mathbf{r})$ we can calculate $\rho(\mathbf{r})$ and $T_s[\rho]$, when the single-particle Schroedinger equation with an external potential $v_{eff}(\mathbf{r})$ is solved:

$$[-\nabla^2 + v_{eff}(\mathbf{r})]\Psi_i(\mathbf{r}) = \varepsilon_i\Psi_i(\mathbf{r}), \tag{2.15}$$

$$\rho(\mathbf{r}) = \sum_{i=1}^{N}|\Psi_i(\mathbf{r})|^2. \tag{2.16}$$

Equations (2.15), (2.13) and (2.16) form self-consisted Kohn-Sham equation [51].

Since the term $v_{xc}(\mathbf{r})$ depends on $\rho(\mathbf{r})$, which depends on $\Psi(\mathbf{r})$, which in turn depends on $v_{xc}(\mathbf{r})$, the problem of solving the Kohn-Sham equation has to be done in a self-consistent (i.e. iterative) way. Usually one starts with an initial guess for $\rho(\mathbf{r})$, then calculates the corresponding $v_{xc}(\mathbf{r})$ and solves the Kohn-Sham equations for the $\Psi(\mathbf{r})$. From these one calculates a new density $\rho(\mathbf{r})$ and starts again. This procedure is then repeated until convergence is reached.

2.1.3 LDA and GGA

The main problem related to the Kohn-Sham equation is the absence of knowledge about the form of exchange-correlated functional $E_{xc}[\rho]$, and thus about $v_{xc}(\mathbf{r})$. Kohn and Sham have proposed the following method, so-called local spin density approximation (LDA), in order to solve this problem [51]. According to LDA, an inhomogeneous system is considered as a number of small volumes, and each small volume contains homogeneous interacting electron gas. Involving exchange-correlation energy per small volume $\varepsilon_{xc}(\rho_\uparrow,\ \rho_\downarrow)$ of the spin-polarized electron gas (with spin densities $\rho_\uparrow$ and $\rho_\downarrow$), the total exchange-correlation energy of the system can be written as

$$E_{xc}[\rho] = \int d\mathbf{r}\varepsilon(\rho_\uparrow, \rho_\downarrow)\rho(\mathbf{r}). \tag{2.17}$$

The total energy of the system is given by

$$E[\rho] = \sum_i \varepsilon - \frac{1}{2}\int d\mathbf{r}d\mathbf{r}'\frac{\rho(\mathbf{r})\rho(\mathbf{r}')}{|\mathbf{r}-\mathbf{r}'|} + \int d\mathbf{r}\rho(\mathbf{r})[\varepsilon_{xc}(\mathbf{r}) - v_{xc}(\mathbf{r})]. \tag{2.18}$$

As a result, the problem of exchange-correlation in an inhomogeneous system is reduced to the calculation of the density of exchange-correlation energy ε_{xc} for a homogeneous electron gas. A certain number of parameterizations have been developed in order to find this density [54, 55, 56, 57].

LDA gives exact solution of the Kohn-Sham equation in the limit of the slow changing spin densities. One could expect that this approximation gives reasonable results only for the systems, where $\rho(\mathbf{r})$ doesn't modify substantially at distances $\sim k_F^{-1}$. Nevertheless, in practice the results obtained in LDA for many other systems of atoms and molecules give quite precise agreement with the experiment, than it was expected a priori (see Ref. [58] for review of successful applications of LDA).

Generalized gradient approximation (GGA) is still local but also take into account the gradient of the density at the same coordinate:

$$E_{xc}[\rho] = \int d\mathbf{r}\varepsilon(\rho_\uparrow, \rho_\downarrow, \nabla\rho_\uparrow, \nabla\rho_\downarrow)\rho(\mathbf{r}). \tag{2.19}$$

Using GGA very good results for molecular geometries and ground-state energies have been achieved.

2.2 Solving the Kohn-Sham equation

The Kohn-Sham equation (2.15) can be written in the following form:

$$\hat{H}_{KS}\Psi_i = \epsilon_i\Psi_i \tag{2.20}$$

the Kohn-Sham eigenvector Ψ_i can be described in terms of a basis set:

$$\Psi_m(\mathbf{r}) = \sum_{p=1}^{P} c_p^m \phi_p(\mathbf{r}) \tag{2.21}$$

Having choose a basis (and hence a finite value for P), we realize that we can tackle equation (2.20) numerically as an eigenvalue problem. Thus we have equation:

$$\begin{bmatrix} \cdots & \cdots & \cdots \\ \vdots & \left\langle \phi_i|\hat{H}_{KS}|\phi_j \right\rangle - \epsilon \left\langle \phi_i|\phi_j \right\rangle & \vdots \\ \cdots & \cdots & \cdots \end{bmatrix} \begin{bmatrix} c_1 \\ \vdots \\ c_P \end{bmatrix} = \begin{bmatrix} 0 \\ \vdots \\ 0 \end{bmatrix} \tag{2.22}$$

We recognize here the matrix elements of the Kohn-Sham Hamiltonian in the basis states, and the overlap matrix elements S_{ij}.

The overlap matrix is defined as:

$$S(\mathbf{R}) = \langle \phi_1|\phi_2 \rangle = \int \phi_1^*(\mathbf{r})\phi_2(\mathbf{r}-\mathbf{R})d\mathbf{r} \tag{2.23}$$

where the integral is over all space and ϕ_1, ϕ_2 are basis function.

Diagonalization of the Hamiltonian matrix will lead to P eigenvalues and P sets of coefficients that express each of the P eigenfunctions in the given basis (if more eigenfunctions are needed, P must be increased). The larger is P, the better is the approximation of the eigenfunction, but is more time-consuming the diagonalization of the matrix in equation (2.22).

Solution of equation(2.22) gives the density matrix as:

$$D = \sum_{l}^{N_{E_F}} |\Psi_l\rangle \langle\Psi_l| = \sum_{l}^{N_{E_F}} \sum_{i} \sum_{j} c_l^i c_l^{j*} |\Psi_l\rangle \langle\Psi_l| \tag{2.24}$$

where N_{E_F} is the number of occupied states up to the Fermi level.

Therefore the matrix elements of the density matrix expressed over the basis set ϕ_p are equal to

$$D_{ij} = \sum_{l} c_l^i c_l^{j*} f(\varepsilon_l - E_F) \tag{2.25}$$

The electron charge density is just the diagonal elements of the density matrix in the real-space representation

$$\langle \mathbf{r}|D|\mathbf{r}\rangle = n\mathbf{r} = \sum_{i,j} \phi_i(\mathbf{r}) D_{ij} \phi_j(\mathbf{r}) \tag{2.26}$$

The steps presented above are iterated until a self-consistent solution for the charge density is obtained. In other words, we start with a initial charge density n_0 which is used to calculated the effective potential $V_{eff}(\mathbf{r})$. We then calculate the Hamiltonian elements H_{ij}. By diagonalizing this Hamiltonian we find the Kohn-Sham eigenstates $|\Psi_l\rangle$ which provide a new density matrix calculated using equation(2.24). This density matrix is subsequently projected onto the basis set to calculate a new electron charge density n_1. This procedure is repeated until the convergence criteria is satisfied

$$\left\| n^j - n^{j+1} \right\| < \delta, \tag{2.27}$$

where δ is a tolerance parameter.

2.3 Pseudopotential methods

In most DFT implementations one uses pseudopotentials to get rid of the core electrons. The idea is to replace the true atomic potential and the chemically inert core electrons with an effective potential (the pseudopotential). The pseudopotential yields very smooth tails of wavefunctions inside the atom, and continuously evolves into the true potential in the outer regions of the atom, which provides the same description for the valence electrons. As a result the computations simplify since one just has to solve for the valence electronic structure.

2.3.1 Vienna Ab-initio Simulation Package (VASP)

Even with the simplifications introduced by DFT the development of efficient and accurate algorithms required for solving Kohn-Sham equations for dominant number of systems is a non-trivial task. An important step was made by George Kresse and co-workers, who developed for these purposes the Vienna Ab-initio Simulation Package, better known as VASP [59, 60, 61, 62]. VASP is a package for performing ab initio quantum mechanical molecular dynamics and molecular static calculations using either Vanderbilt pseudopotentials [63], or the Projector Augmented Wave Method and a plane wave basis set [64]. The calculations are performed within the DFT formalism. All functionals are employed in VASP code in a spin-degenerate and spin-polarized versions. LDA and GGA are the most frequently used functionals. Usually, a LDA functional give the over-binding tendency of an atom-atom interaction, that leads to underestimated lattice constant of a studied system. On the contrary, GGA corrects the over-binding tendency of LDA and yields a correct answer in a certain number of cases, where LDA fails (for example, prediction of the correct ground-state of Fe (ferromagnetic) and Cr (anti-ferromagnetic), which are both predicted by LDA to be non-magnetic)) [65].

The Kohn-Sham equations within VASP code are solved iteratively, using an expansion of the orbitals in terms of the plane wave basis set:

$$\Psi^n_{\mathbf{K}} = \sum_{\mathbf{K}} c^{n,\mathbf{k}}_{\mathbf{K}} e^{i(\mathbf{k}+\mathbf{K})\cdot\mathbf{r}} \tag{2.28}$$

In practice we cannot work with an infinite basis set, and will have to limit it somehow. For plane waves, this can be easily done by limiting the set of all $\mathbf{K}$ with $K \leq K_{max}$. Instead of K_{max}, often the free electron energy corresponding to K_{max} is specified, and is called the *cut-off energy*:

$$E_{cut} = \frac{\hbar^2 K^2_{max}}{2m_e} \tag{2.29}$$

The number of plane waves is determined by the smallest length scales that are to be described in real space. In an atom, near the nucleus, the wavefunction shows steep behavior. In order to describe the sharp part between 0 and the minimum at 0.1Å plane waves with a period as well as roughly an order magnitude less than this distance are needed (0.01Å or 10^{-12} m). It needs about 10^8 plane waves, and would require diagonalization of ($10^8 \times 10^8$)-matrices, which is far beyond the capability of even supercomputers.

The plane-wave (PW) basis-set introduced in VASP offers two advantages: (i) control of convergence, which is crucial for the accurate calculations (and in particular for the prediction of pressures, forces, and stresses) and (ii) the calculation of the forces acting on the atoms and of the stresses on the unit cell using the Hellmann-Feynman theorem. This opens an opportunity to quantum ab-initio molecular dynamics simulations for studying the time-development of a system.

An additional and very important feature of VASP code is ultra-soft (US) pseudopotentials [63], implemented together with PAW functionals. US functionals do not need an explicit treatment of the strongly bound and chemically inert core-electrons. As a result, it leads to saving of the computational demands and time.

The direct approach to the solution of the Kohn-Sham equations suggests the straightforward diagonalization of the Kohn-Sham Hamiltonian [66]. This is inefficient for large systems and plane-wave basis sets. As a rule, 100-150 plane waves per atom are required to achieve basis-set convergence [66]. Hence for systems with a few hundred atoms per cell, the size of the Hamiltonian matrix varies between 10^4x10^4 and 10^5x10^5. In addition, not all eigenvalues, but only those of the occupied and of the lowest empty eigenstates are requiredand this is no more than 10 percent of the total number of eigenvalues [66]. For this reason, iterative variational approaches are to be preferred over direct diagonalization. The successful strategy adopted in VASP is based on a band-by-band optimization of the eigenstates via a minimization of the norm of the residual vector to each eigenstate [61, 62]. Minimizing the residual vector instead of the eigenvalue has the advantage that it is free of orthogonality constraints. After updating all required eigenstates, re-orthogonalization by sub-space diagonalization is sufficient and easy [66]. Together with an optimized preconditioned charge- and spin-density mixing, residual minimization is a very stable and efficient strategy for solving the Kohn-Sham equations [61, 62].

2.3.2 The SIESTA method

In this section, some of the main aspects in the SIESTA (Spanish Initiative for Electronic Simulations with Thousands of Atoms) code are briefly describe below. SIESTA using standard norm-conserving pseudopotentials and a flexible, numerical linear combination of atomic orbitals (LCAO) basis set, which includes multiple-ζ and polarization orbitals[67]. The basis set in SIESTA is a numerical basis orbital obtained by solving the Schrödinger equation of the isolated atom immersed in a hard-wall potential. For each atom I positioned at $\boldsymbol{R}_I$,

$$\phi_{Ilmn}(r) = R_{Inl}(\mathbf{r}_I)Y_{lm}(\mathbf{r}_I) \tag{2.30}$$

where $\mathbf{r}_I$=$\mathbf{r}$-$\mathbf{R}_I$. R_{nl} is the radial function for orbital n and Y_{lm} is the spherical harmonic for the orbital angular momentum l and magnetic quantum number m. The radial part of the wavefunction satisfies the normalization relation:

$$\int |R_{nl}(r)|^2 \, r^2 dr = 1 \tag{2.31}$$

The angular momentum (labelled by l,m) may be arbitrarily large and there will be several orbitals (labelled by n) with the same angular dependence, but different radial dependence, which is called a "multiple-ζ" basis. Each ζ orbital retains the same spherical harmonics as the original atomic orbital, but the radial form is given by a new function constructed with the "split-valence" method[68]. Using this method, the radial part of the second-ζ functions $\phi_l^{2\zeta}$ have the same tail as the first-ζ orbitals $\phi_l^{1\zeta}$ but change to a simple polynomial behavior inside a 'split radius' r_l^s:

$$\phi_l^{2\zeta} = \begin{cases} r^l(a_l - b_l r^2) & \text{if } r < r_l^s \\ \phi_l^{1\zeta}(r) & \text{if } r \geq r_l^s \end{cases} \tag{2.32}$$

where a_l and b_l are determined by imposing the continuity of value and slope at r_l^s. Each radial function may have a different cutoff radius (r_c) and the wavefunctions go to zero for $r > r_c$.

To achieve well converged results, in addition to the atomic valence orbitals, it is generally necessary to also include polarized orbitals, to account for the deformation induced by bond formation. The radial function $R_{nl}(r)$ remains unchanged while one takes the spherical harmonic with higher orbital angular momentum. The polarization orbitals are then added to the basis set:

$$\phi_{n,l+1,m}(r) = R_{n,l+1}Y_{l+1,m} \tag{2.33}$$

In SIESTA one generally uses norm-conserving pseudopotentials according to the Troullier-Martin parameterization[69]. The pseudopotential is initially written in semilocal form (a different radial potential for each angular momentum) from a data file that user can fill with their preferred choice, and then it is transformed to its full non-local form as proposed by Kleinman and Bylander(KB)[70].

Within the pseudopotential framework it is important to keep the consistency between the pseudopotential and the form of the pseudotaomic orbitals in the core region. This is done by using as basis orbitals the solution of the same pseudopotential in the free atom. The shape of the orbitals at larger radii depends on the cutoff radius and on the way the localization is enforced. Two proposals have been adopted:

one is to add a soft confinement potential to the atomic Hamiltonian used to generate the basis orbitals: it smooths the kink and contracts the orbital as variationally suited[71, 72, 73]. However, this method present its won inconveniences. First, there is no radius at which the the orbitals become strictly zero, they have to be neglected at some point. Second, these confinement potentials affect the core region spoiling its adaption to the pseudopotential. An alternative scheme to avoid the kink has also been proposed[74]: Instead of modifying the potential, it directly modifies the orbitals of the atom.

In SIESTA, a new soft confinement potential is proposed. It is

$$V(r) = V_0 \frac{e^{-(r_c - r_i)/(r - r_i)}}{r_c - r} \tag{2.34}$$

As shown in Fig.2.1. It is flat (zero) in the core region, starts off at some internal radius r_i with all derivatives continuous, and diverges at r_c ensuring the strict localization there.

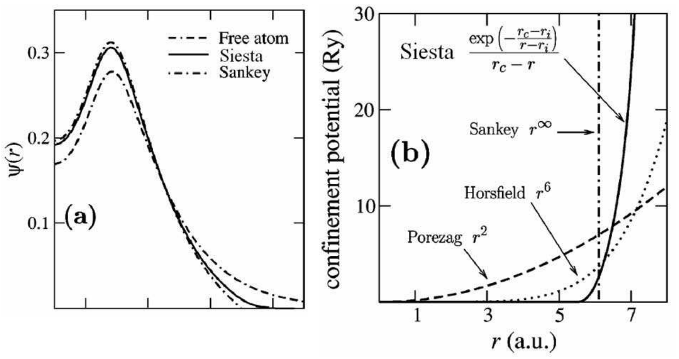

Figure 2.1: Shape of the 3s orbitals of MgO for the different confinement schemes (a) and corresponding potentials (b).

Recently, a number of extensions to SIESTA, which include different approximations for the exchange-correlation potential (LDA+U[75], SIC (Self-interaction correction)[76], Spin-Orbit coupling[77]) have been appeared. Moreover, a DFT implementation based on an LCAO basis set is consistent with the derivation of the Nonequilibrium Green Function methods (NEGF). Several codes (TranSiesta[78] and Smeagol[79, 80, 81]) based on the SIESTA have been developed to calculate the transport properties of nanoscale systems using NEGF method.

2.4 Nonequilibrium Green function method-Smeagol code

Understanding the electron transfer through atomic scale junctions is of great importance for the miniaturization of future electronic devices. A typical system of such a problem is a two-probe device, shown in figure.2.2(a), which consists of two bulk leads and a central region, like a molecule, a surface, or an interface.

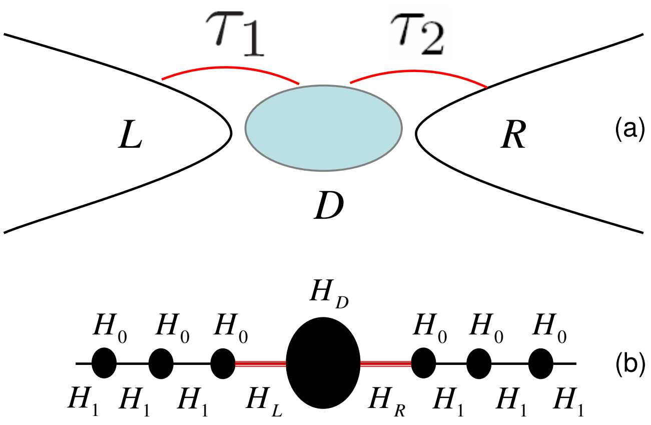

Figure 2.2: (a) Schematic representation of the transport problem. T_1 and T_2 are the strength of the coupling between the left- and right-hand leads with the central devices. (b) quantum mechanical perspective of the transport problem.

Smeagol is a package developed by the collaboration of the Trinity college Dublin and universities of Lancaster and Oviedo. Smeagol has been designed to calculate transport properties of atomic scale devices [79, 80, 81]. Smeagol is based on a combination of the density functional theory and the nonequilibrium Green's function transport method. The Kohn-Sham Hamiltonian provided by the Siesta code[67] is used in Smeagol to calculate the nonequilibrium charge density of an open system via Green's function.

The system under investigation can be described in terms of Hamiltonian as an infinite-dimensional non-periodical Hermitian problem, which can be solved in Green's function formalism:

$$[\varepsilon^+ S - H]G^R(E) = I \tag{2.35}$$

Here G^R is the retarded Green's function for the whole system, I is an infinite identity matrix, $\varepsilon^+ = \lim_{\delta\to 0} E + i\delta$, and E is the energy.

The equation (2.35) can be rewritten with the Hamiltonian and the overlap matrix as:

$$\begin{pmatrix} \varepsilon^+ S_L - H_L & \varepsilon^+ S_{LD} - H_{LD} & 0 \\ \varepsilon^+ S_{DL} - H_{DL} & \varepsilon^+ S_D - H_D & \varepsilon^+ S_{DR} - H_{DR} \\ 0 & \varepsilon^+ S_{RD} - H_{RD} & \varepsilon^+ S_R - H_R \end{pmatrix} \begin{pmatrix} G_L & G_{LD} & G_{LR} \\ G_{DL} & G_D & G_{DR} \\ G_{RL} & G_{RD} & G_R \end{pmatrix} = \begin{pmatrix} I & 0 & 0 \\ 0 & I & 0 \\ 0 & 0 & I \end{pmatrix} \tag{2.36}$$

Where the Green's function G^R is divided into different parts: G_L and G_R describe the infinite blocks of the left- and right-hand side leads, G_{LD} and G_{RD} describe the interaction between the leads and the device, G_{LR} is the direct scattering between the left- and right-hand leads, and G_D describes the device. The matrices H_L, H_R, H_{LD}, H_{RD} and their corresponding overlap matrix blocks S_L, S_R, S_{LD}, S_{RD} are the left- and right-hand-side leads Hamiltonian and the coupling matrix between the leads and the device. The infinite matrices H_L and H_R have the following form:

$$H_L = \begin{pmatrix} \ddots & \ddots & \ddots & \ddots & \vdots \\ 0 & H_{-1} & H_0 & H_1 & 0 \\ \cdots & 0 & H_{-1} & H_0 & H_1 \\ \cdots & \cdots & 0 & H_{-1} & H_0 \end{pmatrix} \tag{2.37}$$

with similar expressions for H_R and the corresponding overlap S matrix. Let us introduce the concept of a principal layer. The principle layer is the smallest unit that repeats itself periodically in the direction of transport and it only interacts with its nearest neighbour principle layers. In other words, all elements in the matrix belongs to two non-adjacent principle layers vanish. The H_0 in equation (2.37) is a matrix describing all interaction within a principle layer and H_1 describing interactions between two principle layers, as shown in figure.2.2 (b). Since the device only interacts with the last principle layer of the leads, all elements in the coupling matrices between the leads and the device are zero except the last one:

$$H_{LD} = \begin{pmatrix} \vdots \\ 0 \\ h_{LD} \end{pmatrix} \tag{2.38}$$

The final expression for G_D^R has the form [82]

$$G_D^R(E) = \left[\varepsilon^+ S_D - H_D - \Sigma_L^R(E) - \Sigma_R^R(E)\right]^{-1} \tag{2.39}$$

where the retarded self-energies for the left- and right-hand side lead

$$\Sigma_L^R(E) = (\varepsilon^+ S_{DL} - H_{DL}) G_L^{0R}(E) (\varepsilon^+ S_{LD} - H_{LD}) \tag{2.40}$$

and

$$\Sigma_R^R(E) = (\varepsilon^+ S_{DR} - H_{DR}) G_R^{0R}(E) (\varepsilon^+ S_{RD} - H_{RD}) \tag{2.41}$$

To some extend, we can say that the effect of leads on the device is expressed by two self-energies forms added to the device Hamiltonian: since when we calculate the Green's function on the device we just calculate the Green's function for the effective Hamiltonian

$$H_{effective} = H_D + \Sigma_L^R(E) + \Sigma_R^R(E)$$

Finally, the current I can be calculate using[83]

$$I = \frac{e}{h} \int dE \; Tr \left[\Gamma_L G_D^{R\dagger} \Gamma_R G_D^R\right] \left(f(E - \mu_L) - f(E - \mu_R)\right) \tag{2.42}$$

where

$$\Gamma_\alpha = i\left[\sigma_\alpha^R(E) - \sigma_\alpha^R(E)^\dagger\right], (\alpha = L, R)$$

The transmission coefficient is

$$T(E, V) = Tr\left[\Gamma_L G_D^{R\dagger} \Gamma_R G_D^R\right] \tag{2.43}$$

2.5 Molecular dynamics

Pseudopotentials-based ab initio codes like Siesta or VASP are widely used to obtain relaxed atomic configurations of various systems. Unfortunately, despite the recent breakthrough in power of available computer facilities, often it is not possible to relax fully ab initio systems consisting of more than a hundred of atoms. Thus it is essential to have a good approximation of ab initio approaches allowing to relax larger systems.

2.5.1 Many-body interatomic potentials

Generally speaking approximate method should, on the one hand, describe the forces acting on each atom, and, on the other hand, it should take into account changes in the electronic structure of atoms caused by bonding to their neighbors. Finnis and Sinclair suggested for *3d*-transition metals functional form of interatomic potentials based on the second moment approximation of the tight-binding theory [84, 85].

Energy of each atom i in the system can be represented as the sum of the attractive bond energy $E^B_{(i)}$ and the repulsive pair interactions $E^R_{(i)}$:

$$E_i = E^B_{(i)} + E^R_{(i)} \tag{2.44}$$

Attractive bond energy is a measure of energy gain caused by formation of bonds between atoms. When atoms get close to each other and start to form bonds, their valence electrons join to the same cloud and initial atomic levels are broadend to bands. Valence electrons are, thus, allowed to occupy states with energies lower than the energy of initial atomic levels. Valence electrons of $3d$-transition metals are represented by delocalized *4*s^2 electrons and partially occupied $3d$-shells. The density of *4*s electrons is distributed over the wide energy range, while d-band is localized in a narrow energy window. Therefore it is reasonable to assume that cohesive properties of $3d$ transition metals are determined mostly by their *3d* states. If we fix the initial atomic level to the center ε_d of d valence band, the attractive bond energy can be written as:

$$E^B_{(i)} = \int^{E_F} (\varepsilon - \varepsilon_d)\, d_{(i)}(\varepsilon)\, d\varepsilon, \tag{2.45}$$

where $d_{(i)}(\varepsilon)$ is the density of d states of atom i. This density, which has in ab initio calculations rather complex form, can be approximated for each atom i by a Gaussian of the form:

$$d_{(i)}(\varepsilon) = \frac{10}{\mu_{(i)}\sqrt{2\pi}} \exp\left(-\frac{(\varepsilon - \varepsilon_d)^2}{2\mu^2_{(i)}}\right). \tag{2.46}$$

The Gaussian (2.46) is centered at ε_d and its width is determined by the second moment (or dispersion) $\mu_{(i)}$ [84, 85]. It is known from the moments theorem [84, 85], that the second moment $\mu^2_{(i)}$ describes all the possible ways of the hopping of an electron from initial site i to all adjacent sites j and backwards:

$$\mu^2_{(i)} = \int_{-\infty}^{\infty} (\varepsilon - \varepsilon_d)^2\, n_{(i)}(\varepsilon - \varepsilon_d)\, d\varepsilon = \sum_{j \neq i} \xi^2_{ij}(r), \tag{2.47}$$

where $\xi^2_{ij}(|\mathbf{r}_i - \mathbf{r}_j|)$ is an average square of hopping integrals between atomic d states on atoms i and j depending on the distance between these atoms [86]. If we assume that each atom in the system is electrically neutral, then $\frac{(\varepsilon-\varepsilon_d)^2}{2\mu_{(i)}^2}$ is the same on all sites and the bond energy can be written as:

$$\begin{aligned} E^B_{(i)} &= constant \times \left(\sum_{j\neq i} \xi^2_{ij}(r) \right)^{\frac{1}{2}} = \\ &= -\left(\sum_{j\neq i,\ |\mathbf{r}_i-\mathbf{r}_j|<r_c} \xi^2_{ij} \exp\left[-2q_{ij} \left(\frac{|\mathbf{r}_i-\mathbf{r}_j|}{r_{0_{ij}}} - 1 \right) \right] \right)^{\frac{1}{2}}, \end{aligned} \tag{2.48}$$

The repulsive part $E_R^{(i)}$ of (2.44) is introduced as a sum of modified Born-Mayer ion-ion repulsions:

$$E^R_{(i)} = \sum_{j\neq i\ |\mathbf{r}_i-\mathbf{r}_j|<r_c} \left[A^1_{ij} \left(\frac{|\mathbf{r}_i-\mathbf{r}_j|}{r_{0_{ij}}} - 1 \right) A^0_{ij} \right] \exp\left[-p_{ij} \left(\frac{|\mathbf{r}_i-\mathbf{r}_j|}{r_{0_{ij}}} - 1 \right) \right] \tag{2.49}$$

where parameter p_{ij} is related to the bulk modulus of the material.

Parameters $P_{\alpha\beta} = \{A^1_{\alpha\beta}, A^0_{\alpha\beta}, p_{\alpha\beta}, \xi_{\alpha\beta}, q_{\alpha\beta}, r_{0_{\alpha\beta}}\}$ of potentials (2.48) and (2.49) for particular atomic species α and β are usually fitted to reproduce a set of experimental and theoretical ab initio values, for instance: lattice constants of species α and β, their cohesive energies, bulk modulus. Binding energies of embedded and ad-clusters of different sizes, geometry and composition are also used to fit parameters of potentials. Surface-related phenomena are described by potentials fitted additionally to the interatomic Hellman-Feynman forces known from ab initio calculations [87, 88, 89, 90, 91, 92, 93].

2.5.2 Algorithm for atomic relaxation

Many-body interatomic potentials describe the energy of the system build of $3d$-transitional metal atoms as a function of position of these atoms. A simplified Hamiltonian describing such a system can be formulated as:

$$H = \sum_i \frac{\mathbf{p}_i^2}{2m_i} + \sum_{j\neq i} E_{(i)[P_{\alpha(i)\beta(j)}]}(|\mathbf{r}_i - \mathbf{r}_j|), \tag{2.50}$$

where $\mathbf{p}_i$ is an impulse of i^{th} atom, m_i is its mass and $P_{\alpha(i)\beta(j)}$ denotes a set of fitted parameters describing interaction between atoms of species α and β situated at sites i and j, respectively. This Hamiltonian results in a system of Newtonian motion equations:

$$\frac{d^2\mathbf{r}_i(t)}{dt^2} = -\sum_{j\neq i} \frac{1}{m_i} \nabla E_{(i)[P_{\alpha(i)\beta(j)}]}(|\mathbf{r}_i - \mathbf{r}_j|). \tag{2.51}$$

Analytical solution of (2.51) for a time moment τ is performed by double integration over time t from 0 up to τ. The first integration yields velocities of each atom, the second – their coordinates. A numerical solution of equations (2.51) can be performed by molecular dynamics (MD) simulations. Particular realizations can be different but MD provides a trajectory of each atom in a phase space. Below we give a brief review of the Verlet algorithm used in our MD code.

At first initial positions $\mathbf{r}_i^1$ and velocities $\mathbf{v}_i^1$ are defined. The initial velocities are usually set to zero and initial positions are adopted from the ideal crystal structure of studied materials.

1. Forces $\mathbf{F}_i$ acting on each atom at time step n are calculated as:

$$\mathbf{F}_i^n = -\sum_{j \neq i} \frac{1}{m_i} \nabla E_{(i)[P_{\alpha(i)\beta(j)}]}(|\mathbf{r}_i^n - \mathbf{r}_j^n|) \tag{2.52}$$

2. New velocities $\mathbf{v}_i^{n+1}$ are calculated as:

$$\mathbf{v}_i^{n+1} = \frac{1}{2}\left(\mathbf{v}_i^n + \frac{\mathbf{F}_i^n}{m_i \delta t}\right), \tag{2.53}$$

   where δt is a real time increment between consequent time moments n and $n+1$.

3. New coordinates $\mathbf{r}_i^{n+1}$ are calculated as:

$$\mathbf{r}_i^{n+1} = \mathbf{r}_i^n + \frac{\mathbf{v}_i^{n+1}}{\delta t}, \tag{2.54}$$

   and the procedure is repeated from the first point.

Usually MD simulations are performed to model microcanonical ensembles of particles, when the total energy of the system preserves. Slight modifications allow to employ MD in investigations of systems at constant temperatures or pressures. Our aim is to find relaxed positions of all the atoms in the system, when all the atoms are immobile and all the forces in the system, therefore, are equal to zero. Such a "frozen" system can be treated as a system at a zero temperature.

The general approach used in MD to fix the temperature of the system is to control kinetic energy of the whole system:

$$\frac{1}{2}\sum_{i}^{N} m_i v_i^2 = \frac{3N}{2} k_B T_{fix} = const. \tag{2.55}$$

Such a renormalization of velocities is performed at each step of MD simulations (so called isokinetic MD).

Although this method is designed to keep a system at any temperature T_{fix}, it should be slightly modified to study a system at $T_{fix} = 0$. In this particular case all the velocities at each step are cancelled by renormalization and system remains static. It is not suitable, because atoms anyway should be moved to minimize potential energy of the static system at $T_{fix} = 0$. To avoid this contradiction, we apply so called quenching procedure, when the velocity vector $\mathbf{v}_i$ of atom i is cancelled only if it points in the opposite direction than the force $\mathbf{F}_i$ acting on this atom, i.e. if a scalar product $\left(\mathbf{r}_i^{n+1} - \mathbf{r}_i^n, \mathbf{F}_i\right)$ becomes negative. It should be stressed, that in this procedure the total kinetic energy of the system and, therefore, its temperature are gradually reduced to zero. Accordingly, the relaxed static configuration configuration is achieved when the actual temperature of the relaxed system becomes zero, or in another words, when all the forces in the system are vanished and potential energy can not be transferred into kinetic. If this condition is satisfied, than the resulting static system possesses the minimal energy and can be treated as the relaxed one.

Chapter 3

Molecule-adatom junctions on a metal surface

In this chapter we study the interaction between the magnetic adatoms adsorbed on a metal surface and the molecule. We demonstrate that electronic and magnetic properties of adatom-molecule junctions on metal surface can be manipulated by varying the tip-substrate distance. The effect of the STM tip at lateral positions on the junctions' electronic and magnetic properties is also discussed.

3.1 Interaction of magnetic atoms with a benzene molecule

Recent advances in the field of molecular spintronics have enabled the manipulation of spins in molecules with control down to a single spin. Magnetic states of atoms have been found to change significantly in metal-molecule clusters and sandwiches[94, 95, 96, 97, 98]. Here, we provide systematic studies of the equilibrium geometry, electronic and magnetic properties of 3d-transition metal atoms supported on a benzene molecule.

The geometry of the atom-molecule complex is shown in Fig.3.1. The magnetic atoms are placed above the gravity center of the molecule. All the atomic positions of the cluster are relaxed without any constraint. The bond distances separating the transition metal atoms and the benzene plane as well as those of C-C and C-H are listed in Table 3.1. Our results coincide with those reported by Jena *et al.*, very well[94]. We note that the C-C and C-H bond lengths remain practically unchanged from their respective values 1.40 Å and 1.1 Å[94], in a pure benzene molecule. However, the adatom-benzene distance changes nonmonotonically along 3d elements in the periodic table.

The most interesting result is the modification of the magnetic moment of the M-benzene complexes with increasing the atomic number of 3d atom (cf. Fig.3.2). In Fig.3.2, three interesting trends can be observed:

(1) The magnetic moment of the Cr atom on benzene molecule remains nearly unchanged from its free atom value.

(2) Elements, such as Sc, Ti and V, experience an enhanced magnetic moment compared to free atom values.

(3) The magnetic moment of Mn, Fe and Co adatoms are strongly decreased due to the interaction with the molecule. The magnetic moment of the Ni atom is completely quenched.

In order to get a deep insight into these results, the projected density of states (PDOS)

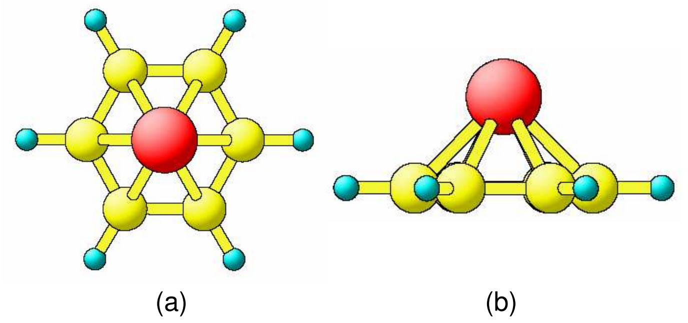

Figure 3.1: Magnetic adatom adsorbed on a benzene molecule forming a M-benzene complex. (a) top view, (b) side view.

Table 3.1: Bond distances between magnetic atoms and the gravity center of the benzene ring (M-BZ), C-C, and C-H.

	M-BZ (Å)	C-C (Å)	C-H (Å)
Sc	2.05	1.42	1.11
Ti	1.93	1.42	1.11
V	1.95	1.42	1.11
Cr	2.08	1.42	1.11
Mn	1.50	1.42	1.11
Fe	1.47	1.42	1.11
Co	1.42	1.42	1.11
Ni	1.44	1.42	1.11

of the Co adatom in Co-benzene complex is plotted in Fig.3.3 (a). It can be seen that Co 3d states strongly hybridize with the 2p states of the benzene molecule. Due to the hybridization, the spin up 3d states of Co are occupied and split into three main peaks. The spin down 3d states of Co also consist of three peaks: two of them are occupied and the one is found to be at the Fermi level. However, the spin up and spin down 4s states lie approximately at 0.9 eV and 1.1 eV above Fermi level. It indicates that the 4s orbital of Co adatom is totally empty. The PDOS illustrates that there is a charge transfer of approximately two electrons from 4s states of free Co atom to 3d states in the Co-benzene complex. As we know, the valence electron configuration of a free Co atom is $3d^7 4s^2$, i.e. there are three unpaired electrons. So its magnetic moment is 3 μ_B. However, for the Co atom in the Co-benzene complex, two electrons jump from 4s states to 3d states and there are 9 electrons in 3d orbital of the Co atom. Consequently, the magnetic moment is reduced from 3 μ_B for the isolate Co atom to 1 μ_B for the Co adsorbed on the benzene molecule. The magnetic moment of the C atoms is 0.01 μ_B per atom and it is 0.003μ_B per atom for H atoms in the Co-benzene complex.

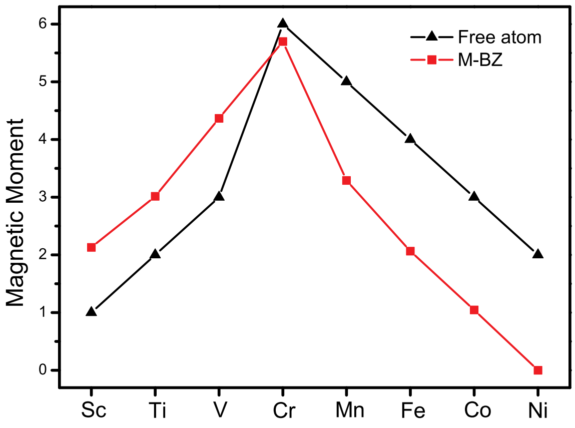

Figure 3.2: Magnetic moment (μ_B) of transition metal atoms-free and supported on benzene.

The PDOS for Fe atom adsorbed on the benzene molecule is plotted in Fig.3.3 (b). The transfer of the Fe 4s electrons to 3d states can be also observed. The valence electronic configuration for a free Fe atom is $3d^6 4s^2$ and it changes to $3d^8 4s^0$ because two electrons jump from the 4s orbital to the 3d orbital. There are only two electrons unpaired in 3d orbital. Therefore, magnetic moment of the Fe reduces from 4 μ_B in a free Fe atom to 2 μ_B in a Fe-benzene complex.

Since the Cr ($3d^5 4s^1$) 4s orbital is not full, all the electrons would occupy spin up channels, and hence its magnetic moment changes only slightly. As for elements Sc, Ti and V, which lie at the left side of Cr in the periodic table, there is nearly one 4s electron transfers to the 3d orbital. The valence electronic configuration for them are $3d^1 4s^2$, $3d^2 4s^2$ and $3d^3 4s^2$. Due to the transfer of electrons from 4s orbital to 3d orbital, their magnetic moments increase from 1 μ_B, 2μ_B and 3μ_B in free atoms to 2 μ_B, 3 μ_B and more than 4μ_B in M-benzene complexes.

Table 3.2: Structural and magnetic properties for Fe and Co atoms adsorbed on the benzene (denoted as MBZ) and the graphene (denoted as MGr). The properties listed are the binding energy ΔE (eV), adatom-carbon distance d_A (Å) and magnetic moment per adatom of the adatom-molecule system M_A (μ_B)

.

	ΔE	d_A	M_A
FeBZ	0.98	1.47	2.00
FeGr[99]	1.02	2.09	2.00
FeGr[100]	0.86	2.46	2.03
CoBZ	1.12	2.06	1.0
CoGr[99]	1.27	2.10	1.0

Finally, it is interesting to compare magnetic moments of 3d atoms on benzene with

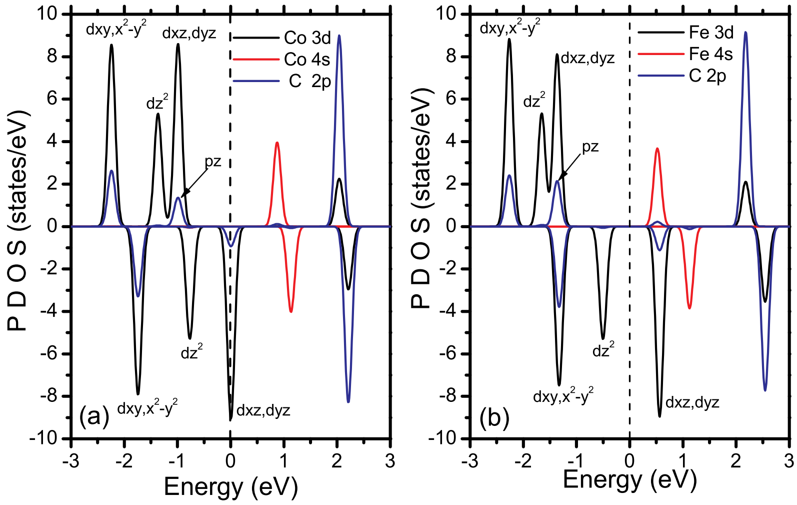

Figure 3.3: (a) PDOS on the Co 4s, 3d and 2p states for C in Co-benzene complex. (b) PDOS on the Fe 4s, 3d and 2p states for C in Fe-benzene complex

their magnetic moments on graphene. After the synthesis of isolated single graphene[101], much research interest has shifted to its unique properties due to a possible applications in electronics and spintronics. Understanding of the interaction between the metal atoms and graphene is essential for fabricating new electronic devices. Benzene molecule, which is the smallest organic molecule with a carbon ring, can be regarded as the unit cell for other complex molecules, nanoscale carbon tubes or even graphene. Here, we compare our results with other theoretical works[99, 100] of the adsorption of magnetic adatoms on the graphene, see Table.3.2. Although binding energies and adsorption heights are different, the magnetic moment of the Co and Fe are the same on the benzene molecule and on graphene.

3.2 Molecule-magnetic adatom sandwiches on Cu(001)

It is believed that in future applications the spin of the magnetic molecules should be coupled to a substrate. To address the problem of the interaction of molecules with a substrate, we first place a magnetic adatom on a Cu(001) surface, then put a benzene molecule above it, forming a planar sandwich configuration: C_6H_6/M/Cu(001) (M=Mn, Fe, Co and Ni). This structure is different from other magnetic molecules, such as cobalt phthalocynine (CoPc)[44] or MnPc[48], where the magnetic atoms are the part of the molecule. For molecule sandwiches C_6H_6/M/Cu(001), the magnetic atoms are just inserted between the Cu surface and the benzene molecule. Such structure is stable and can be formed by placing a benzene molecule above the a magnetic adatom adsorbed on Cu(001) surface using STM tip. It has been recently demonstrated that a large HB-HPB molecule ($C_{66}H_{78}$)[102], consisting of a central benzene ring connected to six-phenyl groups and six t-butyl lateral groups attached to a phenyl ring, can be dragged by a STM tip and put above Cu adatoms. Recent theoretical study has proved that a single benzene molecule adsorbed on a Cu(110) surface can be manipulated by dynamic force microscopy using a clean silicon tip[103].

3.2.1 Adsorption of a benzene molecule on a Cu(001) surface

The adsorption of organic molecules on metal surfaces has attracted a lot of attention in order to understand the interaction mechanism at organic/metal interface. Serving as a model system for more complicated molecules, benzene molecule has been intensively studied in both experimental investigations and theoretical calculations [94, 95, 96, 97, 98].

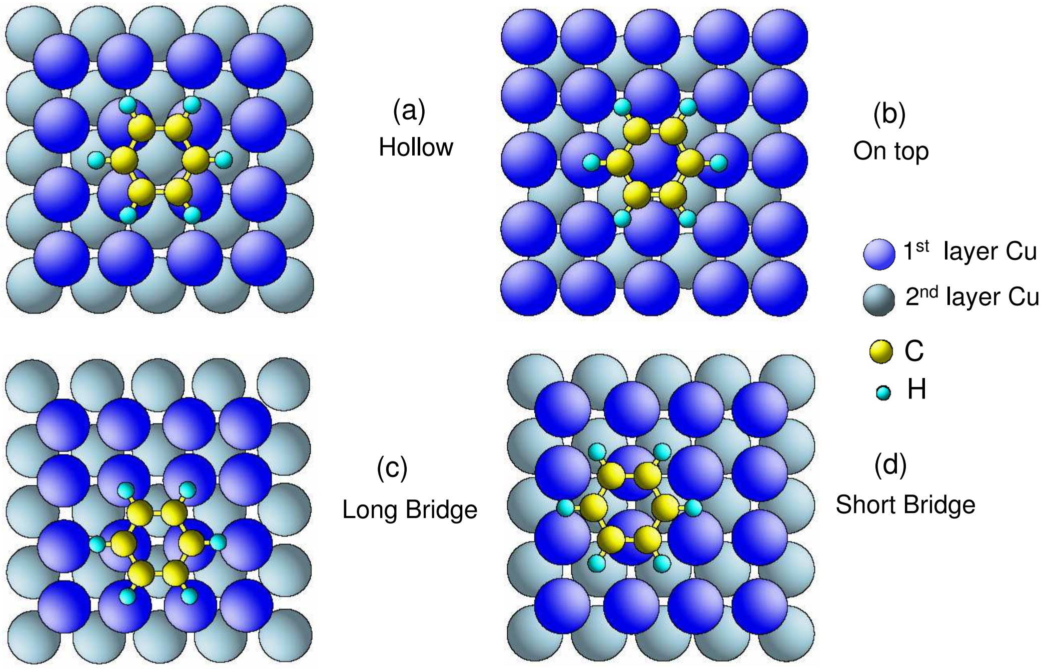

Figure 3.4: Possible positions for the benzene molecule adsorbed on the Cu(001) surface (top view).

A molecule adsorbed on metal surfaces can occupy several high symmetrical positions, in which the center of the carbon ring is classified as being either above top, bridge, or hollow sites on a surface. For the benzene molecule adsorbed on the Cu(001) surface, the calculations employ a 4×4 supercell, which contains 16 Cu atoms per layer. Due to the high symmetry of the surface, there are only four positions for the benzene molecule to occupy, defined as hollow, atop, long-bridge and short-bridge, as shown in Fig.3.4. The difference between the long-bridge and the short-bridge site is that: in the former case, two carbon atoms in the ring are nearly at the atop site above Cu atoms , while in the later case, the Cu atoms beneath the benzene molecule situate between the C-C bonds, as shown in Fig.3.4 (c),(d), respectively.

In order to find the minimum energy configuration for the adsorbed molecule, we have performed *ab initio* calculations (by means of the SIESTA code) in a fully relaxed geometry for the benzene molecule and for the first two layers of the copper surface. We have calculated the adsorption energy E_{adsorp}, as the difference between the total energy of a molecule on surface system ($E_{benzene/Cu(001)}$) and the energy of the isolated molecule ($E_{benzene}$) and of the clean substrate($E_{Cu(001)}$):

$$\Delta E = E_{benzene/Cu(001)} - E_{benzene} - E_{Cu(001)} \tag{3.1}$$

The most favorable adsorption site of the benzene molecule on Cu(001) surface is the hollow site, with an absorption energy of -0.65 eV, followed by the bridge site (the long-bridge site is energetic more favorable than the short-bridge by about of 0.1 eV), and then the atop site. The benzene molecule with its gravity center over the hollow site of the Cu(001) surface is shown in Fig.3.4(a). The carbon ring remains parallel to the surface at a height of 2.26 Å. Four carbon atoms are 2.34 Å away from the first-layer copper atoms and the other two carbon atoms are 2.63 Å away from the copper atoms. The carbon bonds in the benzene ring expand from 1.398 Å to 1.414 Å and 1.419 Å, depending on the location of the pair of C atoms. The six hydrogen atoms are nearly in the same plane but about 0.15 Å higher than the benzene ring, and the carbon-hydrogen bond length is nearly unchanged, about 1.1 Å. As for Cu atoms in the substrate, we find that the four Cu atoms lying beneath the benzene ring are vertically shifted away from the surface by 0.12 Å, which represents 3% of the relaxed lattice parameter, and elongate horizontally to 2.617 Å, a change is about 1.5%. Our results are in good agreement with the previous calculations[104].

3.2.2 Single magnetic adatoms on Cu surfaces

Here, we present our results for a single magnetic adatoms on Cu(001) surface. In order to check the pseudopotentials generated by ourself, we calculate the electronic and magnetic properties of single 3d magnetic adatoms on Cu(001) surface, and compare our results with calculations performed by means of Korringa-Kohn-Rostoker(KKR) Green's function method [105]. For the generation of pseudopotentials we use following electronic configurations $3d^5 4s^2$, $3d^6 4s^2$, $3d^7 4s^2$ and $3d^8 4s^2$ for Mn, Fe, Co and Ni, respectively. Such electronic configuration are used for both local density approximation (LDA) and general gradient approximation (GGA) calculations.

A 4×4 supercell is used for Cu(001) surface, which contains 16 Cu atoms for each layer. The magnetic adatom is positioned at the hollow site. Therefore, the distance between the adatom and other adatom in its neighbor cell is larger than 10 Å , so interactions between them can be neglected. The geometry is optimized until all residual forces acting on each atom are less than 0.01 eV/Å.

The magnetic moment of adatoms are plotted in Fig.3.5. It can be observed that Siesta results are in a good agreement with those obtained by means of the KKR Green's function method[105]. Note that, for the KKR method, the lattice relaxations are not included. We have also performed calculations with SIESTA method for a relaxed positions of adatoms adsorbed on Cu(001) surface and found only small changes in magnetic moments.

3.2.3 Benzene-adatom sandwich on Cu(001)

In the C_6H_6/M/Cu(001) sandwich, the benzene molecule is parallel to the Cu(001) surface. Such structure is experimentally feasible and can be produced using the STM manipulation. Recently, S-W.Hla et al., have deposited ferrocene molecule on Au(111) surface[106]. Each ferrocene molecule contains one Fe atom and two cyclopentadienyl (C_5H_5, cp) rings. By means of lateral manipulation with the STM tip, the ferrocene molecule has been split into

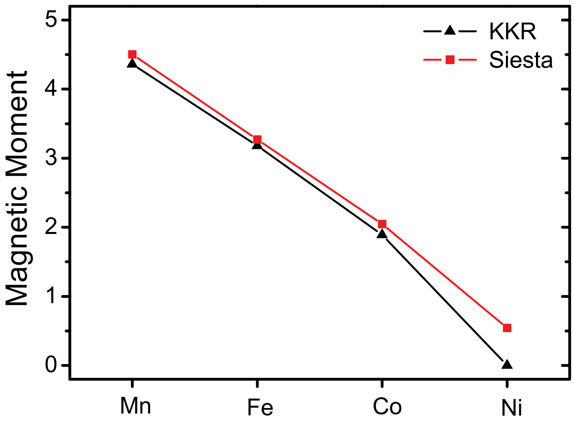

Figure 3.5: Magnetic moment (μ_B) of adatoms adsorbed on Cu(001) surface calculated by the Siesta and the KKR method. All calculations are performed in ideal geometry.

two parts, a cp ring and a Fe-cp complex. The Fe-cp complex was adsorbed on Au(111) surface with cp ring parallel to the surface, similar to the benzene molecule in C_6H_6/M/Cu(001) sandwich.

Table 3.3: Structural and magnetic properties of magnetic adatoms in C_6H_6/M/Cu(001) sandwich. The properties listed are the vertical distance between the Cu(001) surface and the magnetic adatom d_{SA}, distance from the adatom to the gravity center of the benzene molecule d_{AB}, magnetic moment per atom on magnetic adatom M_A, magnetic moment per carbon atom in the benzene molecule M_C.

	d_{SA} (Å)	d_{AB} (Å)	M_A (μ_B)	M_C (μ_B)
Cr	1.70	2.04	3.79	0.015
Mn	1.50	1.60	2.32	0.010
Fe	1.45	1.54	0.77	0.004
Co	1.46	1.53	0	0
Ni	1.47	1.55	0	0

In order to check the stability of the benzene-magnetic adatom sandwich, a possible inclination of the benzene molecule above the magnetic adatom towards the Cu(001) surface plane has been considered as well. We have slightly rotated the benzene molecule to form a 5 degree angle between the molecule plane and the Cu(001) surface. After relaxation, we have found that benzene molecule is adsorbed parallel to the Cu(001) surface again.

The initial distance between the adatom and the benzene molecule is the same as that in M-benzene complex. The relaxed geometries and the magnetic moments of the magnetic adatoms in C_6H_6/M/Cu(001) sandwich are listed in Table.3.3.

For the M-benzene complexes, the vertical distance between adatoms and surface and the vertical distances between benzene and adatoms decrease from Cr to Ni. Compared to a single magnetic adatom on Cu(001) surface, the distances between adatoms and Cu

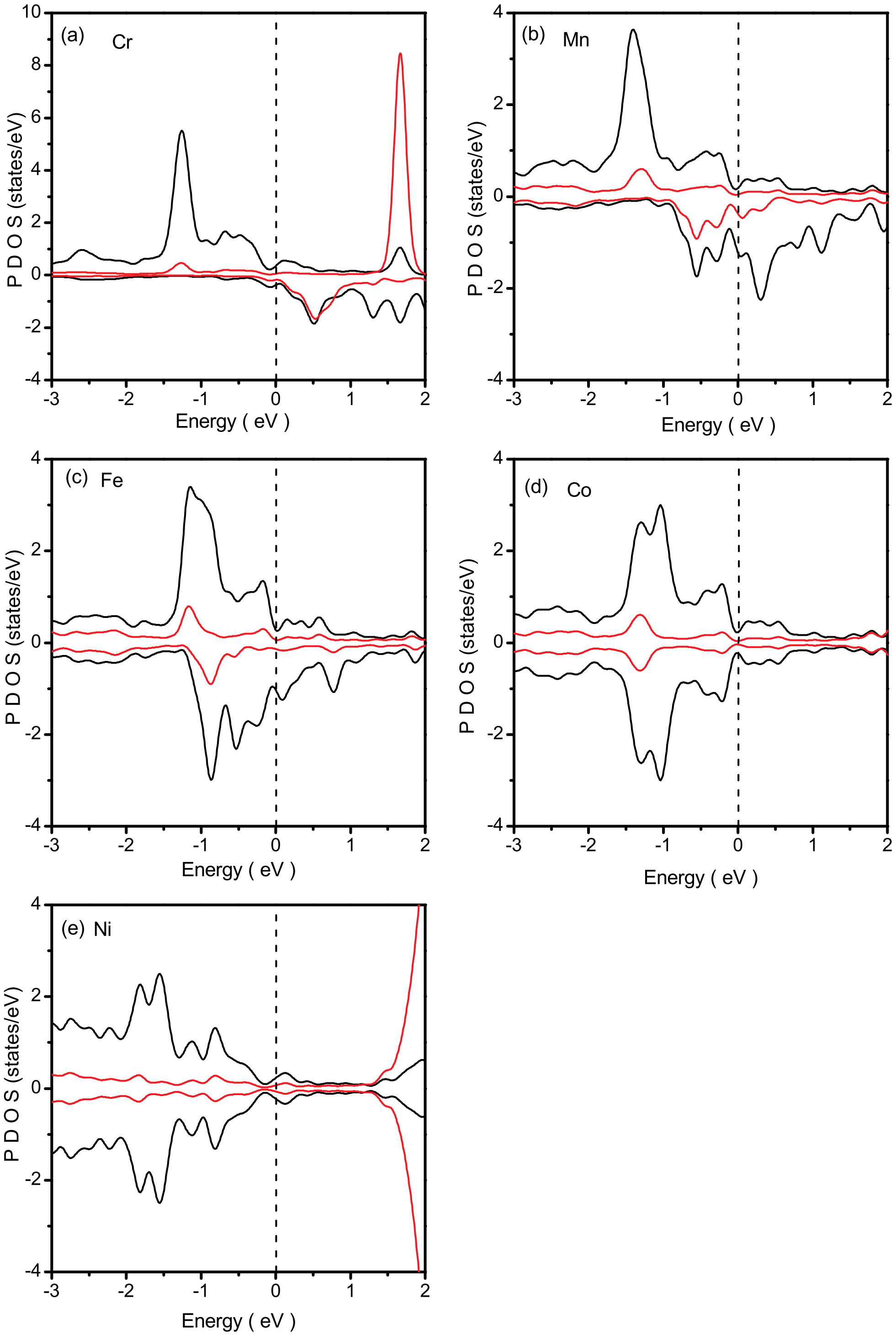

Figure 3.6: (a)-(e):PDOS on magnetic atoms d states (black curves) and on C 2p states (red curves) in C_6H_6/M/Cu(001) sandwiches (M= Cr, Mn, Fe, Co, Ni).

surface decrease, while all the distances between magnetic adatoms and benzene molecule in C_6H_6/M/Cu(001) sandwich increase. For example, the distance between Co adatom and Cu surface decreases from 1.51 Å in Co/Cu(001) system to 1.46 Å in C_6H_6/Co/Cu(001) sandwich, while the distance between Co atom and benzene molecule increase from 1.42 Å in Co-benzene complex (as shown in Fig.3.1) to 1.53 Å in C_6H_6/M/Cu(001) sandwich. For all sandwiches, the C-C and C-H bond length remains unchanged.

Interestingly, comparing the magnetic moment of a single adatom adsorbed on Cu(001) surface (Fig.3.5) and in M-benzene complex (Fig.3.2), one can find that that the magnetic moment of atom in C_6H_6/M/Cu(001) sandwich greatly decreases, especially for the Co atom (see Table.3.3). As we know, the magnetic moment for a single Co adatom on Cu(001) surface is about $2\mu_B$ and it is $1\mu_B$ in Co-benzene complex. However, the magnetic moment for a Co atom in C_6H_6/M/Cu(001) sandwich is totally quenched.

The PDOS of atoms in C_6H_6/M/Cu(001) sandwich are plotted in Fig.3.6. From the figure, some interesting trends can be noticed:

(1) For all atoms, their 3d states are strongly hybridized with the 2p states of the carbon atoms in the benzene molecule. In the majority part of the Cr *d* states, its main peak is about 1.3 eV below the Fermi level, and strongly hybridizes with the 2p states of the C atoms in the benzene molecule, while the hybridization between them near the Fermi level is weak. For the minority part, there is a very strong hybridization between Cr 3d states (about 0.5 eV above the Fermi level) and C 2p states. Starting from Mn atom, the intensity of the hybridization between the majority part of the 3d states of the adatom and C 2p states near the Fermi level increases.

(2) Because of the hybridization, the width of both spin up and spin down parts increases and spreads for several eV, which means that the crystal field splitting increases.

(3) The majority part of 3d states of the adatoms moves to Fermi level and increases its population, while the minority part of 3d states shifts towards the lower energy. Therefore, the spin splitting (energy difference between the center of the majority part and the minority part) of PDOS of the adatom decreases. As the result, the magnetic moment is strongly suppressed. For the Cr sandwich, its spin up part is about 1.2 eV below the Fermi level and its spin down part is about 0.5 eV above the Fermi level. The spin up part of the Mn sandwich is only about 0.1 eV below the Fermi level, while half of the spin down part moves below the Fermi level and is occupied. Especially for the Co sandwich, most of its spin down part is below the Fermi level and exactly the same as the spin up part, resulting in a quenched magnetic moment.

(4) The magnetic moment of carbon atoms in the benzene molecule decrease from Cr to Ni and these magnetic moments have the same trend as those of the adatoms. For Cr adatom, the spin splitting in PDOS is much larger than for other adatoms, such as Co and Ni. Due to the hybridization between the Cr and the benzene molecule in C_6H_6/Cr/Cu(001) sandwich, the spin splitting of the Cr adatom strongly decreases. However, the spin split of the Cr is still much larger than for other magnetic sandwiches. Since 2p states of the C atoms are strongly hybridized with 3d states of the Cr adatom, the spin splitting of the C atom in C_6H_6/Cr/Cu(001) sandwich is also enlarged and larger than that in other adatom sandwiches. The spin direction of the C atoms is parallel with the spin direction of the Cr adatom in Cr sandwich, however, they would prefer to be antiparallel in Mn, Fe sandwiches. Moreover, in Co and Ni sandwiches, the magnetic moment of the C atoms are also quenched.

As we have already discussed in Fig.3.2, when a single Co atom is adsorbed on a benzene molecule, the two 4s electrons of the Co atom jump to 3d orbital, leading to a reduction of the magnetic moment to $1\mu_B$. Since the magnetic moment of the Co atom is quenched to $0\mu_B$ in C_6H_6/Co/Cu(001) sandwich, the role of the 4s electron should be discussed in details. The 4s states of the Co in three systems: (1) Co atom adsorbed on a Cu(001) surface (Fig.3.7 a) , (2) on a benzene molecule (Fig.3.7 b) and (3) in C_6H_6/Co/Cu(001) sandwich (Fig.3.7 c) are plotted in Fig.3.7. From the figure, one can see that the 4s states of the Co atom in C_6H_6/Co/Cu(001) sandwich spread over the whole energy range and look similar to electronic states of the Co atom adsorbed on Cu surface. Therefore, the 4s electrons are not the main reason for the sharp decrease of the magnetic moment of the Co adatom.

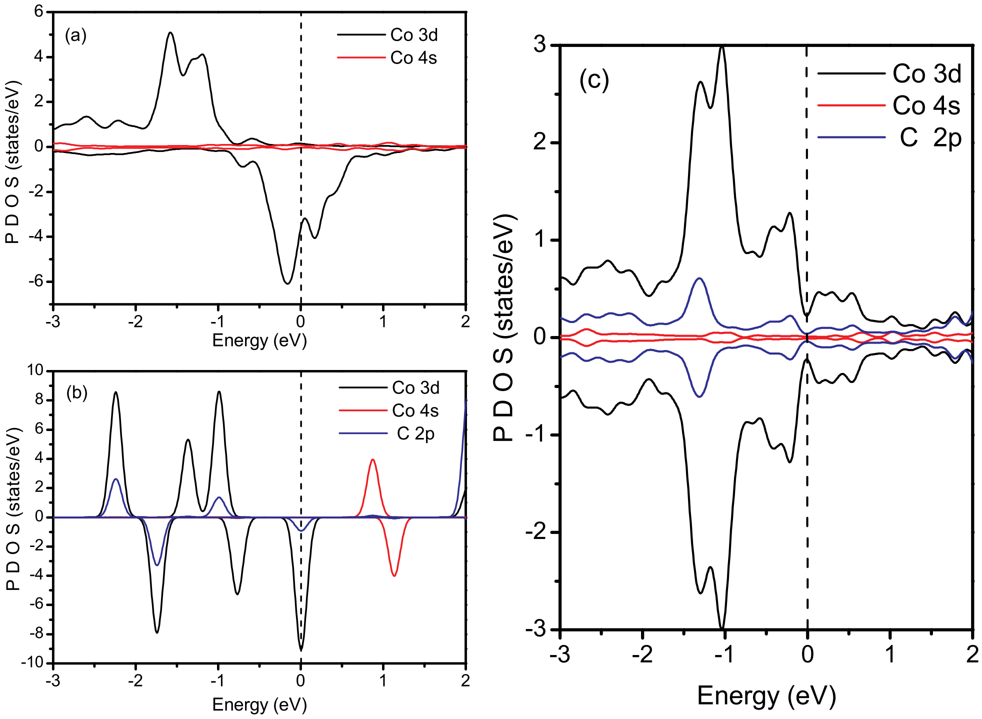

Figure 3.7: (a) 3d and 4s states of the Co adatom on Cu(001) surface, (b) 3d, 4s states of the Co and 2p states of the C atoms in the Co-benzene complex, (c) 3d, 4s states of the Co and 2p states of the C atoms in C_6H_6/Co/Cu(001) sandwich.

It can also be observed from Fig.3.7 (b) that the C 2p states are only partially hybridized with the Co 3d states. The d electrons of the 3d transition metal atom orbital according to their symmetries can occupy one $d\sigma(d_{d^2})$, two $d\pi$ (d_{xz},d_{yz}) and two $d\delta$ ($d_{x^2-y^2}$,d_{xy}). However, up to now, we do not know which orbitals hybridized with the C 2p orbital. These orbitals are plotted in Fig.3.8. For a single Co atom adsorbed on Cu(001) surface, the majority part of the $d\sigma$ and $d\delta$ orbitals are nearly at the same position (about 0.5 eV lower than $d\pi$ orbitals), while the minority part of them is located at the Fermi level and exhibit some small splitting. In C_6H_6/Co/Cu(001) sandwich, all these orbitals are split. Since the Co atom is nonmagnetic in this configuration, the majority part is exactly the same as the minority part. The dσ orbitals are about 1 eV below the Fermi level and by about 0.5 eV closer to the Fermi level than the dδ orbital, while the dπ orbital is only about 0.1 eV below the Fermi level. The C 2p$_z$ states (p$_x$,p$_y$ states are not in the energy range presented in Fig.3.7) are also plotted in the figure. As shown in figure, the C 2p$_z$ states are strongly hybridized with the Co dπ (d$_{xz}$,d$_{yz}$) and dδ (d$_{x^2-y^2}$,d$_{xy}$) orbitals, while they are only weakly hybridized with the Co dσ(d$_{d^2}$) states.

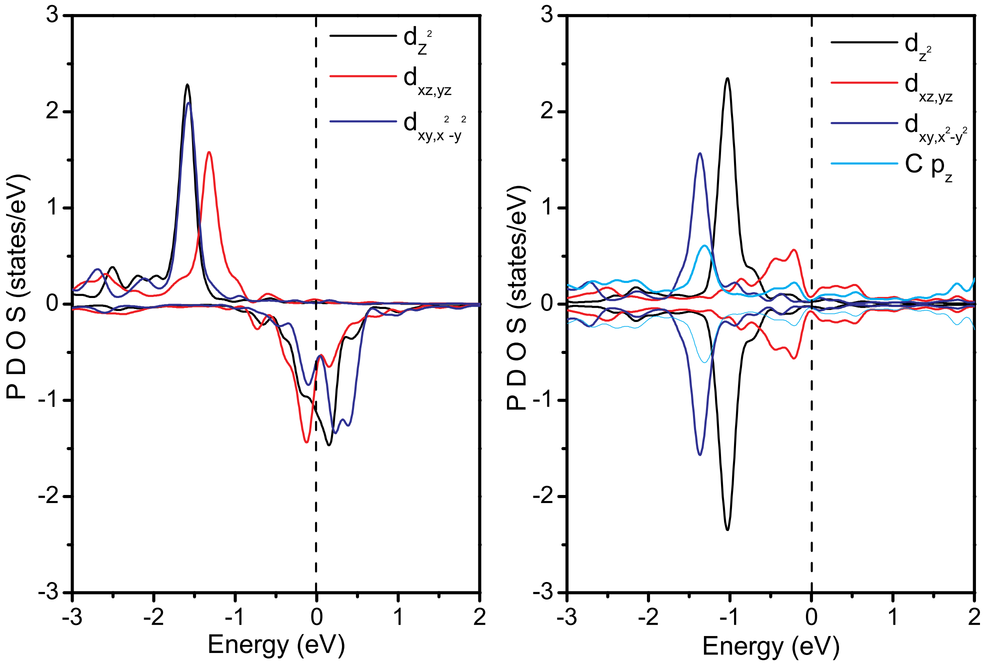

Figure 3.8: (a) d orbitals for the Co atom on Cu(001) surface, (b) d orbitals of the Co and p$_z$ orbital of the C in C_6H_6/Co/Cu(001) sandwich.

3.3 Manipulating magnetism of a molecule-adatom junction on a metal surface

The ability to control the spin-state of an isolated magnetic atom has been recently demonstrated [6, 107]. By placing an iron or manganese atom at a specific location on the copper-nitride thin film, Hirjibehedin et al., [6] determined the orientation and strength of the anisotropies of individual magnetic adatoms. Atoms in their experiment can hold a specific magnetic direction, which may allow them to store data. Yayon et al.,[107] have used the direct exchange interaction between a single magnetic atom and a nanoscale magnetic island to fix the spin of an adatom. The above results are of great importance for future atomic-scale technologies and single-atom data storage.

Recent experiments of Wahl *et al.*, have demonstrated the ability to tune the spin states of a single magnetic adatom by the controlled attachment of a molecule ligand[43]. The

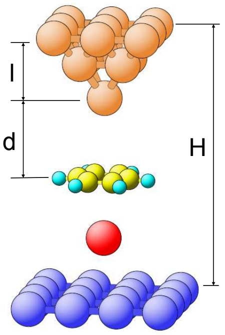

Figure 3.9: Setup for the calculation. H is the distance between the magnetic STM tip and the substrate. l is the length of the tip, and d is the distance between the benzene molecule and the STM tip.

Kondo temperature of a Co adatom on a Cu(100) surface was found to significantly increase with the number of CO molecules attached to the adatom. The magnetic moment of a free standing CoPc molecule is about 1.09 μ_B, when it is adsorbed on a Au(111) surface, its magnetic moment is quenched to 0 μ_B. However, Zhao *et al.*,[44] and Crommie [49]have revealed that the magnetic state of a CoPc molecule on Au(111) can be manipulated by the dehydrogenation of the ligand by voltage pulses from the STM tip. After removing eight hydrogen atoms from its four lobes, the magnetic moment of the molecule is recovered to 1.03 μ_B.

The STM tip is usually considered as a tool to modify the structure of the molecule or the detector of the magnetic states of the molecule. However, the influence of the STM tip on the electronic and magnetic properties of the molecule is not included in the experiment. Theoretical and experimental studies have shown that electronic and magnetic properties of a single adatom on metal surfaces significantly depend on the tip-surface distance[108, 109, 110].

3.3.1 Vertical manipulation

One of the most delicate aspects in modeling the STM experiments is the geometry used for the tip. Ideally, the tip should consist of thousand of atoms to mimic the tips used in real experiments. However, in practice one is limited by the computational resources required for the calculation. Fortunately, the chemical and magnetic interaction between the tip and sample is dominated by the foremost atoms due to the exponential decay of the wavefunctions. In calculations, there are two main approaches in order to model a metal tip:

i) the cluster model, where the shape and the atomic arrangements could play a role in determining the electronic properties of the apex atom.

ii) an extended substrate model (as 3D supercell or 2D slab systems), where the metallic properties of the system are better represented.

In spin-polarized STM experiments, the tip is often made from the nonmagnetic material coated by thin films of antiferromagnetic (AFM) or ferromagnetic (FM) materials [107, 111]. In our calculations, we use a cluster model for our tip. We model the tip by a pyramid consisting of 13 Cu atoms and one Cr atom for the tip-apex, as shown in Fig.3.9.

At different tip-substrate distances, the benzene molecule and the Co atom show different relaxation behaviors, summarized in Table.3.4. When the tip-substrate separation is in the range between 8.6 Å and 9.3 Å, the benzene molecule, Co adatom and the substrate under the adatom are pulled up, while the Cr tip-apex is pulled down. At this stage the attractive interactions between the tip and the benzene molecule, and between the Co atom and the substrate are the driving forces for the observed atomic relaxations. However, at a closer tip-substrate separation (between 8.6 Å and 8.1 Å), the repulsive interactions between the tip and the benzene molecule, and between the molecule and the Co atom begin to play an important role. It can be observed that the benzene molecule, Co adatom and the substrate are pushed down, while the tip-apex is pushed up.

The changes of the magnetic moment of the Co adatom during the approach of the STM tip are also summarized in Table.3.4. When the tip-substrate separation is larger than 10.1 Å, the tip has very weak interaction with the benzene molecule. The magnetic moment of the Co in the C_6H_6/Co/Cu(001) system is quenched to $0\mu_B$ because of the hybridization between the C 2p states and the Co 3d states. When the tip-substrate separation decreases from 9.3 Å to 8.1 Å, the magnetic moment of the Co atom increases from 0.16 μ_B (0.08 μ_B, LDA) to 0.96 μ_B (0.58 μ_B, LDA); on the contrary, the magnetic moment of the Cr tip-apex decreases from 4.61 μ_B (4.61 μ_B, LDA) to 3.67 μ_B (3.51 μ_B, LDA).

Table 3.4: Displacements and magnetic moments of the system at different tip-substrate separations. H is the tip-substrate distance, as shown in Fig. 3.9. $\Delta l = l - l_0$ is the change of the tip length, where l and l_0 are the tip length with and without tip-benzene interaction. $\Delta d = d - d_0$ is the distance difference between the Cr tip-apex and the benzene molecule along z axis after and before full relaxation. The ideal benzene-Co and Co-substrate distances without tip-benzene interaction are 1.53 Å and 1.46 Å. The last two columns are the magnetic moment of the Cr tip-apex and Co adatom calculated with the GGA(LDA) method.

H (Å)	Δl (Å)	Δd (Å)	M_{Cr} (μ_B)	M_{Co} (μ_B)
>10.1	0	0	4.75(4.68)	0(0)
9.3	0.12	-0.14	4.61(4.61)	0.16(0.08)
8.6	-0.05	0.07	4.24(4.05)	0.64(0.38)
8.1	-0.25	0.28	3.67(3.51)	0.96(0.58)

Table 3.5: Bond length of C-C and C-H and the magnetic moment per C atom in the benzene molecule at different tip substrate distances.

H (Å)	C-C (Å)	C-H (Å)	M_C (μ_B)
9.3	1.453	1.106	0.011
8.6	1.458	1.106	0.027
8.1	1.460	1.106	0.032

Since the Cr tip is an AFM tip, we replace the second Cu layer in the tip by a Cr layer and set its spin direction to be antiparallel to the Cr tip apex. For the tip-substrate separation of 9.3 and 8.1 Å, the magnetic moments of the Cr tip apex are 4.13 μ_B and 2.98

μ_B, respectively; while they are 0.14 μ_B and 0.74 μ_B for the Co adatom. Although the magnetic moment of the Cr tip apex is different for the different tips, the switching off/on of the magnetic moment of the Co adatom can be also observed.

In the calculations, a small magnetic moment changes of the C atoms in the benzene molecule can also be observed and their spin directions are antiparallel to the tip-apex and the Co atom. They are given in Table.3.5. At a short tip-substrate distance, the increased C-C bond length is due to the increased interaction between the tip and benzene molecule. For all the cases, the C-H bond length remains unchanged.

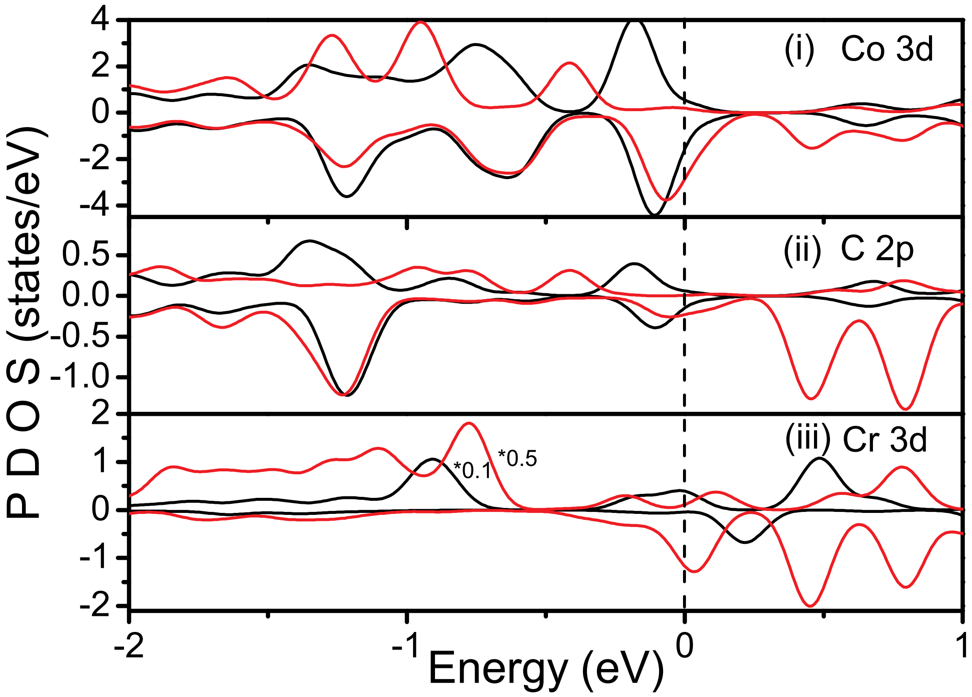

Figure 3.10: The PDOS of the Co, C and Cr atoms in C_6H_6/Co/Cu(001) junction at two different tip-substrate distances, 9.3 Å and 8.1 Å. The black lines are the PDOS at a larger tip-substrate distance 9.3 Å and the red lines are the PDOS at a closer tip-substrate distance 8.1 Å. (i) 3d states of the Co atom, (ii) 2p states of the C atoms in the benzene molecule, (iii) 3d states of the Cr tip-apex.

Partial density of states (PDOS) of the Co atom, C atoms in the benzene molecule and the Cr tip-apex for two different tip-substrate distances, 9.3 Å and 8.1 Å, are plotted in Fig. 3.10. At a larger tip-substrate distance of 9.3 Å, the hybridization between the 3d states of the Cr atom and the 2p states of the C atoms is weak. Meanwhile, the hybridization between the 2p states of the C atoms and the 3d states of the Co atom is still very strong. The minority part of the Co 3d states is slightly shifted to the Fermi level. Therefore, the magnetic moment of the Co atom slightly increases. However, it can be observed from Fig. 3.10 that, at a closer tip-substrate distance (8.1 Å), the 2p states of the C atoms in the molecule are strongly hybridized with the 3d states of the Cr and Co atoms. Fig. 3.10

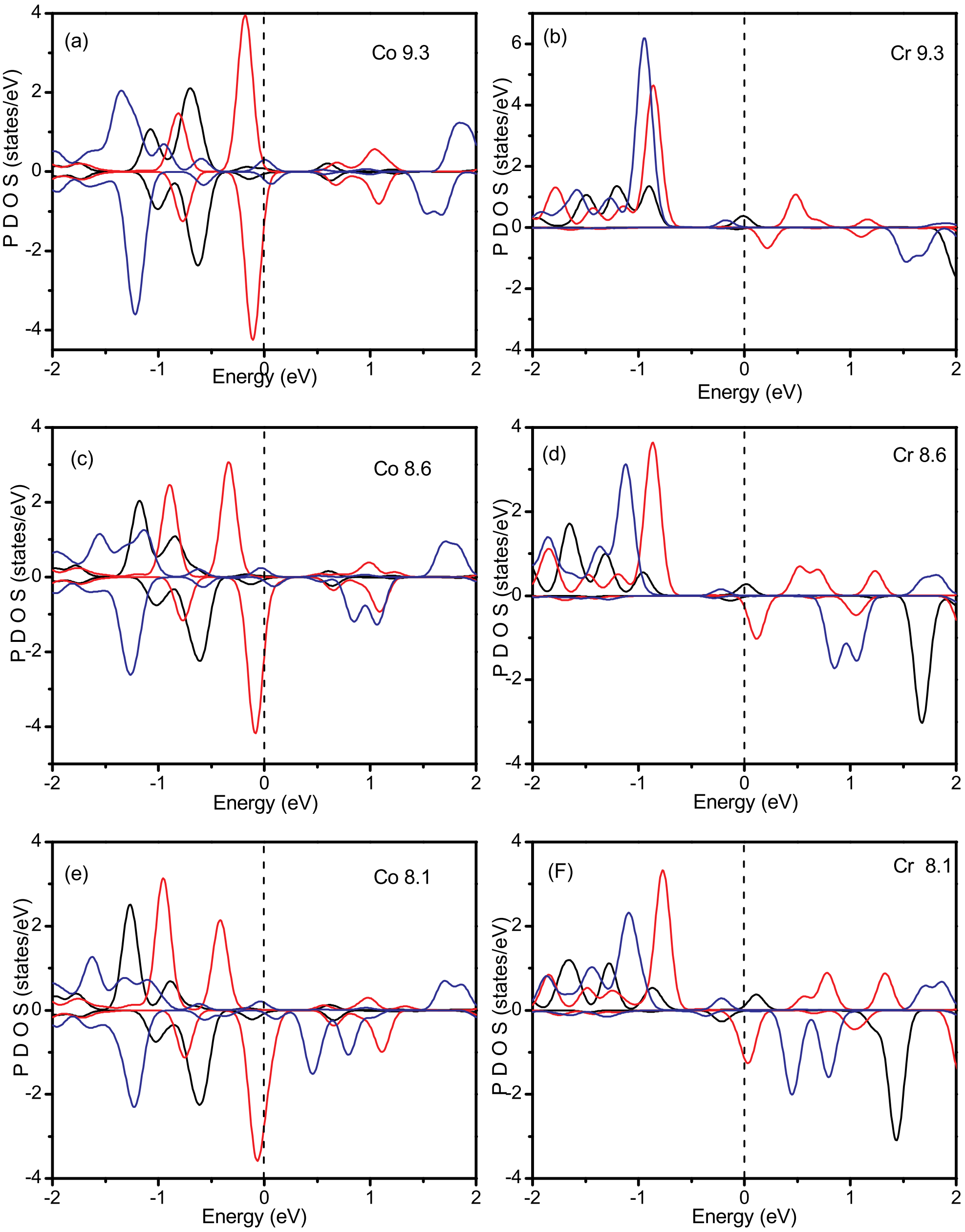

Figure 3.11: The d orbitals of the Co (left) and Cr atoms (right) in the adatom-molecule junction for three different tip-substrate distances, 9.3 Å , 8.6 Å and 8.1 Å. The black curves are d_{d^2} orbital, the red curves are d_{xz},d_{yz} and blue curves are $d_{x^2-y^2}$,d_{xy} orbitals.

shows that at a closer tip-substrate distance the hybridization between the C 2p states and Cr 3d states is much stronger than that for the larger tip-substrate distances. The increased interaction between them pushes the minority 3d states of the Cr atom to the Fermi level and increases their population. Therefore, the magnetic moment of the Cr tip-apex reduces from 4.61 μ_B to 3.67 μ_B. However, one can also observe that the hybridization between C 2p states and the Co 3d states at a closer tip-substrate distance is weaker than that at a larger tip-substrate distance. Therefore the majority part of the Co 3d states in Fig. 3.10 moves far away from the Fermi level. The magnetic moment of the Co atom at a closer tip-substrate distance recovers from 0.16 μ_B to 0.96 μ_B. In all of our calculations, the spin direction of the tip-apex and Co atom prefer parallel alignment.

The PDOS for five d orbitals of the Co atom and Cr tip-apex are plotted in Fig.3.11. At a large tip-substrate distance, both of the majority and minority parts of the Co d_{xz},d_{yz} are near the Fermi level and the spin splitting between them are very small. For the Cr tip-apex, in the majority part there is only a small d_{d^2} peak at the Fermi level, while for the minority part, there is no peak at Fermi level and the d_{xz},d_{yz} orbital is about 0.2 eV above the Fermi level. Therefore, at a large tip-substrate distance, the Co atom only has a small magnetic moment. At a short tip substrate distance, the minority part of the Co 3d states slightly shifts towards Fermi level, while the majority part strongly moves to the lower energy. As for the Cr tip-apex, its majority remains unchanged, however, the minority part of d_{xz},d_{yz} states moves to the lower energy and centered at the Fermi level. So the magnetic moment of the Co atom increases and the magnetic moment of the Cr tip-apex decreases. In conclusion, the changes of the magnetic moment of the C_6H_6/Co/Cu(001) sandwich is caused by the interaction between the Co d_{xz},d_{yz} orbital and the Cr d_{xz},d_{yz} orbital via C $2p_z$ orbital.

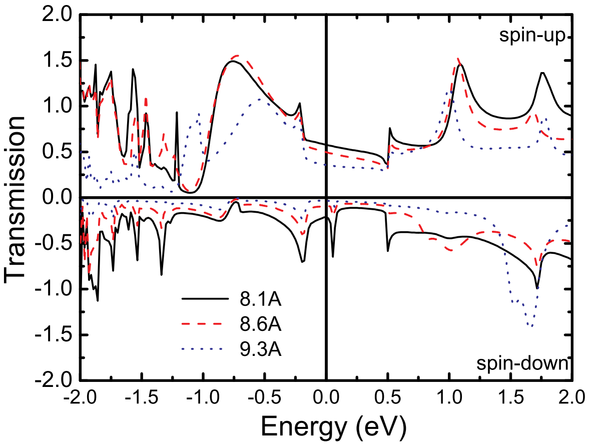

Figure 3.12: The transmission spectra for three different positions of the STM tip. Positive values related for the spin-up channel and negative correspond to the spin-down.

To gain detailed insight into the effect of the tip on the transport properties of the junction, we have performed transport calculations using the TranSiesta [78] code (in cooperation with Prof I. Mertig's group), where the non-equilibrium Green function method is implemented. Details of transport calculations can be found in [78].

Fig. 3.12 shows spin-resolved transmission probabilities through the Co-benzene molecule for three different positions of the STM tip. One can see that with decreasing the distance between the tip and the substrate the transmission at zero bias increases. Increasing the distance between the tip and the molecule leads to quenching of the transmission for the spin-down channel. These results clearly show that such junctions can be used as a well controlled spin-filter.

3.3.2 Lateral manipulation

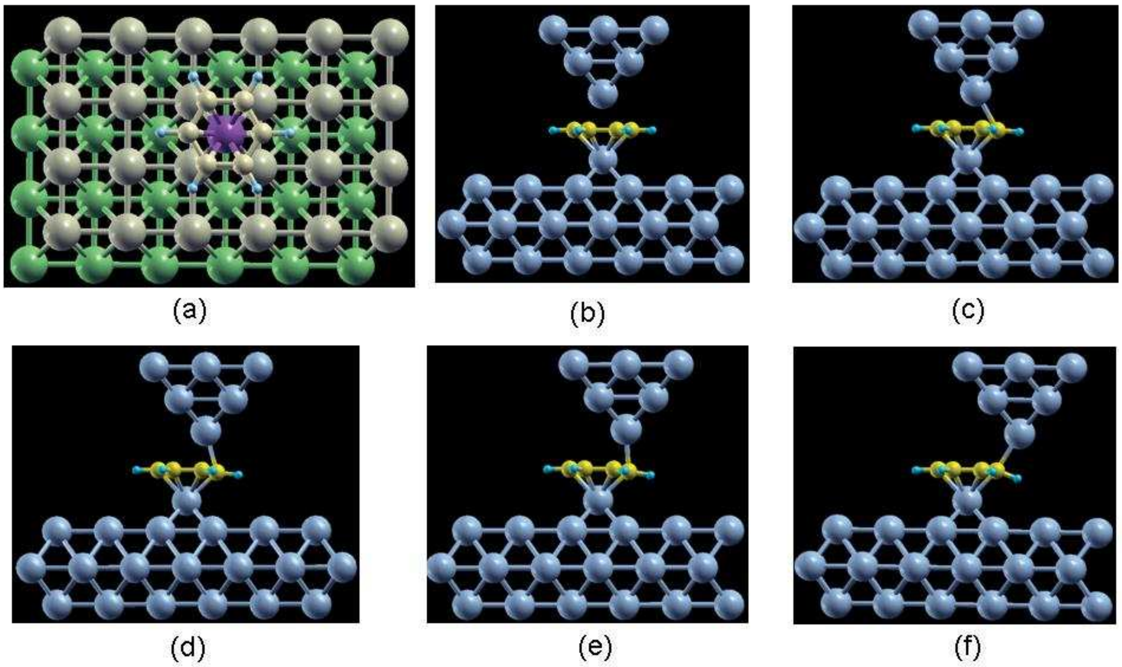

Figure 3.13: (a) Top view of the sample (without tip). From (b) to (f) are the relaxed geometries in our calculations at different lateral distances L_{TA}. L_{TA} is defined as the lateral displacement between Cr tip-apex and Co atom. (b) L_{TA}=0 Å, (c) L_{TA}=0.5 Å, (d) L_{TA}=1.0 Å, (e) L_{TA}=1.4 Å, (f) L_{TA}=2.5 Å.

There are two modes for STM operation: one is the vertical motion, and the other one is the lateral motion. As we have discussed above, the electronic and magnetic properties of the C_6H_6/Co/Cu(001) sandwich can be strongly affected by the vertical manipulation with the STM tip. Up to now, we do not know what would happen with electronic and magnetic properties of the C_6H_6/Co/Cu(001) sandwich by approaching the STM tip along the lateral direction. The set up for our calculations is shown in Fig.3.13. In order to simulate the lateral movement of the STM tip, a 6×4 supercell is used for our calculation which includes 24 Cu atoms in each layer. Since the magnetic moment of the Co atom in C_6H_6/Co/Cu(001) sandwich increases to $0.96\mu_B$ at a tip-substrate separation 8.1 Å, in the calculations we have fixed this vertical distance and shifted the STM tip towards the right side. Lateral distance (L_{TA}) is defined as the lateral displacement between the STM tip-apex and the Co atom. During the calculations the benzene molecule, Co atom and the top layer of the Cu are allowed to relax, while the bottom layers of the substrate are fixed. Figs.3.13 (b)-(f) represent the relaxed structure at different lateral displacements L_{TA} from 0 to 2.5 Å.

The total energy of the system, magnetic moment of the Co atom and Cr tip-apex at different lateral displacements L_{TA} are plotted in Fig.3.14. Moving tip from a short L_{TA} to a large L_{TA}, the total energy of the system increases. When the tip is just put above the Co atom, there is a very strong interaction between the tip and the molecule, thus the total energy is the lowest. When we increase the lateral separation, the interaction between the tip and the benzene molecule decreases, and hence the total energy of the system increases. At a short L_{TA}, similar to those we have discussed above, the strong interaction between the tip and the molecule decreases the magnetic moment of the Cr tip-apex and the weak interaction between the molecule and the Co atom increases the magnetic moment of the Co atom, while at a large L_{TA}, the magnetic moment of the Co atom decreases and the Cr tip-apex increases, as shown in Fig.3.14.

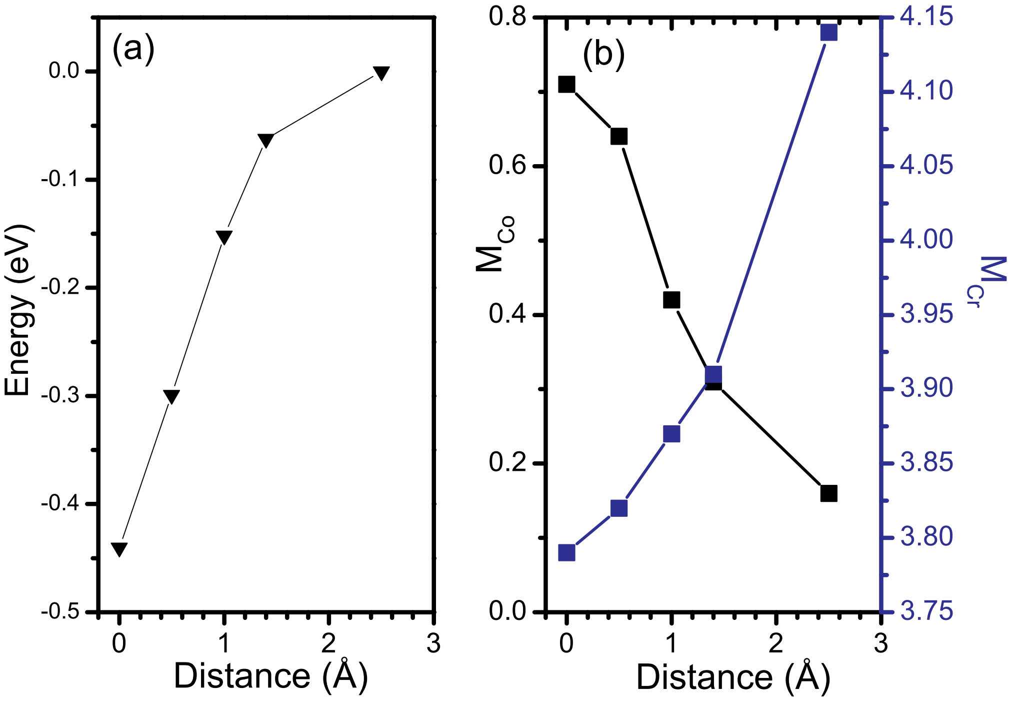

Figure 3.14: (a) Total energy of the system at different L_{TA}, (b) Magnetic moment of the Cr tip-apex and Co atom as a function of L_{TA}.

Chapter 4

Interaction of the STM tip with single adatoms on metal surfaces

In this chapter, we demonstrate the effect of the STM tip on electronic and magnetic properties of single magnetic adatoms on metal surfaces. We present theoretical studies supported by experiments showing the importance of structural relaxations in the tip and at the surface for understanding the Kondo effect on a single magnetic adatoms. Effect of the STM tip on an adatom dynamics on metal surfaces is discussed.

4.1 Controlling the Kondo temperature with the STM tip: experimental motivation

The location of the STM tip at the proximity of surfaces and adatoms can cause perturbations due to the tip-sample interaction[110, 112]. Even a small change in the tip-sample distance can significantly affect the tunneling current, since it depends exponentially on the distance. Recent theoretical studies have shown that the tip can strongly change positions of adatoms above the surface and could affect their electronic and magnetic properties[108]. Ab initio calculations and the molecular dynamics simulations have revealed that the Cu tip strongly changes the position of Co adatoms above the Cu(001) surface. Atomic relaxations in the tip and the substrate have been found to significantly depend on the tip-surface distance [108]. It has been found that approaching the tip towards the Co adatom from the tunneling regime to the contact regime, the minority d states of the Co adatom are slightly shifted to lower energies, while the majority d states move to the Fermi level and deplete their population. Therefore the magnetic moment of the Co adatom has been found to be strongly suppressed due to the hybridization between d states of the adatom and the s states of the tip-apex and the Cu atoms in the substrate. Since the Kondo effect is caused by the interaction of a magnetic impurity with the conduction electrons of a surrounding metal host, the changes of the LDOS could lead to measurable changes in the Kondo temperature. Such scenario has been recently confirmed by experiments of Néel *et al.,*[109]. Approaching a tip towards a cobalt adatom on Cu(001) surface from the tunneling regime to the contact regime the Kondo temperature of the system has been found to increase from 78 K to more than 130 K[109]. Motivated by the above mentioned works we have addressed the following questions: What is the effect of the atomic geometry in the contact and tunneling regimes on the electronic and magnetic properties of a single adatom? It is a priori not evidence if the Kondo temperature strongly depends on the tip-surface distances for closed-packed substrates as has been seen for (100) surfaces[109]. In other words, the question which we are going to address is what is the interplay between structural relaxations due to the tip-adatom interaction and the Kondo temperature? We have performed a theoretical investigations in order to support experimental results of the tip-adatom interactions on a Cu(111) surface.

Experiments have been performed in the group of Prof. Klaus Kern (MPI Stuttgart) using a home built scanning tunneling microscope operated at 6K in ultra high vacuum (UHV) with a base pressure of 1×10^{-11}mbar. Cu(111) single crystal have been cleaned in UHV by cycles of Ar^+ ion sputtering and annealing. Co single atoms were deposited on the Cu surface at 20K from a thoroughly degassed Co wire wound around a W filament. This resulted in a coverage of about 10^{-3}ML of isolated immobile Co adatoms. The STM tip, chemically etched from tungsten wire, was treated in vacuo by electron field emission and soft indentation into the copper surface. This assured a spectroscopically featureless tip near the Fermi energy. Given this preparation, the tip was most likely covered by copper atoms deriving from the substrate.

The inset in Fig.4.1 shows the conductance of a single Co adatom at various tip-sample displacements. This has been achieved by recording the current while approaching the tip towards the atom, in open feedback conditions. As the tip sample distance is reduced the current increases smoothly from the tunneling to the point contact regime following the exponential dependence with the tip-substrate distance (z) characteristic of the electron tunneling process $I(z) = I_0 exp(-Az)$ (where A is proportional to the work function of tip and substrate). As the point contact regime is reached the current is found to exhibit a characteristic quantization plateau with only a weak dependence on the distance. The plateau is observed to be $1G_0$ where G_0 is the conductance quantum $G_0 = 2e^2/h$ (h is the Planck constant) in agreement with studies on Co/Cu(100)[109]. Topographic images acquired before and after the tip was approached and retracted from the point contact configuration confirm that the contact region as well as the tip have not changed during the tip displacements.

Information on the Kondo resonance has been obtained recording the dI/dV spectra on top of the Co adatom at various tip-sample displacements. In Fig.4.1, the spectra obtained at the tip-substrate separation indicated by the circles in the inset are shown. All the curves obtained in the range from the initial tunneling ($\Delta Z = -2$Å) to the point contact ($\Delta Z = 0.2$Å) condition show a characteristic dip in the local density of states at an energy close to the Fermi level. This dip, which is due to the Kondo resonance can be characterized according to its width ΔE, which is proportional to the Kondo temperature T_K, ΔE=$2k_B T_K$, where k_B is the Boltzmann constant[32, 113].

The Kondo temperature can be extracted from these curves by fitting the experimental spectra with a Fano line function according to:

$$dI/dV \propto \frac{(q+\epsilon)^2}{(1+\epsilon)} \tag{4.1}$$

with

$$\epsilon = \frac{(eV-\epsilon_K)}{k_B T_K} \tag{4.2}$$

where q and ϵ_K define the asymmetry of the curve and the energy position of the resonance with respect to the Fermi energy [115]. The obtained Kondo temperature T_K is presented in Fig.4.1. for each sampled tip position. As can be seen, the Kondo temperature for the Co on Cu(111) system is constant, within the experimental error, from the tunneling to the

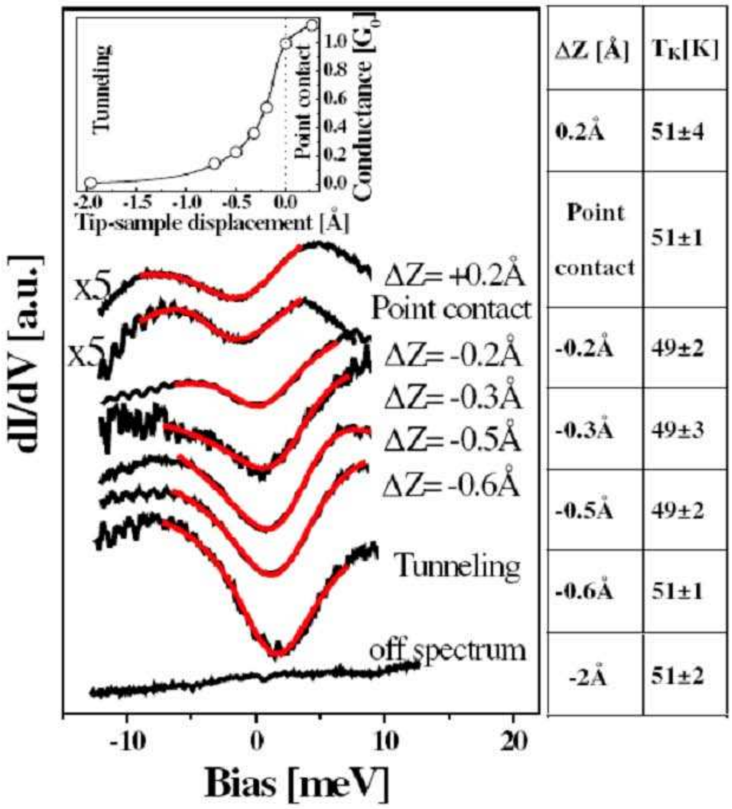

ΔZ [Å]	T_K[K]
0.2Å	51±4
Point contact	51±1
-0.2Å	49±2
-0.3Å	49±3
-0.5Å	49±2
-0.6Å	51±1
-2Å	51±2

Figure 4.1: Conductance and dI/dV spectra for isolated Co atoms on a Cu(111) surface achieved at different tip-substrate distances ΔZ from tunneling to point contact. Prior to the point contact measurements the tip was stabilized at a defined sample distance, setting the tunneling conditions at 8 meV and 5 nA. In the inset a representative current vs tip displacement is shown. dI/dV spectra have been recorded at the positions indicated by circles in the inset. The curves are normalized to the tunneling current at the tip height location and a vertical offset has been added for a better visualization. The Kondo temperature T_K given on the right side of the image has been obtained fitting the curves with a Fano line shape (light line),see Ref[114].

point contact regime. These results have been reproduced with different tips and different tip treatments which assured a spectroscopic featureless tip in the energy range at the Fermi level.

The observed behavior of the Kondo temperature on the Cu(111) surface contrasts with the behavior previously reported for the Co/Cu(100) system, where a considerable increase of the Kondo temperature (from 70-90K in tunneling to 150K in point contact) was observed [109]. As will be shown below this difference can be ascribed to the sensitivity of the Kondo effect to the local atomic geometry.

4.2 Atomic-scale simulations and ab initio studies of the effect of the STM tip on the electronic properties of magnetic adatoms

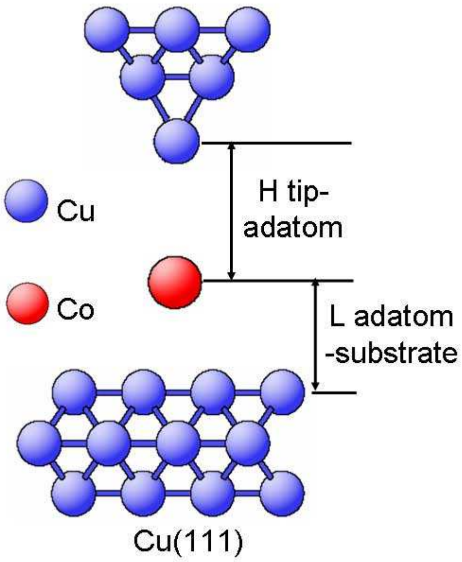

Figure 4.2: Setup for MD and DFT calculations. H is the tip-adatom distance and L is the adatom-substrate separation.

To demonstrate the interplay between the structure of the junction and its electronic and magnetic properties first, we performed atomic-scale simulations of the structure for the different tip-substrate distances. Then, we considered the effect of structural relaxations on electronic properties of Co adatoms performing *ab initio* calculations. Reducing the tip-substrate separation can induce a local perturbation on the atomic arrangement of the junction which can influence the coupling between the orbitals of the electrodes and of the Co atom, and can consequently affect the electronic and the magnetic properties of the system. To simulate the nanoscale-junction on the atomic scale, we have performed molecular dynamics (MD) calculations using many-body interatomic potentials fitted to the spin-polarized *ab initio* calculations[116]. In these simulations the tip has been represented as a pyramid consisting of 10 Cu atoms arranged in fcc(111) stacking order, as shown in Fig.4.2. Fig.4.3 shows the variation of the tip-adatom and the adatom-substrate separations during the tip displacement [panels Fig.4.3(a) and Fig.4.3(b), respectively]. On a first glance one can see that beside an initial region, the tip-Co adatom as well as the Co adatom-substrate distances are not linearly proportional to the tip displacement. As the tip-substrate distance is reduced, the atomic order at the junction relaxes: the atoms of the tip, the Co impurity as well as the atoms of the substrate move to new equilibrium positions. The real tip-substrate distance is then a dynamic variable according to the specific location of the tip and to its attractive and repulsive interaction with the surface and the impurity. Specifically, up to the minimum distance of 5.3Å, the tip-Co adatom distance is almost linear with the tip displacement. Approaching further, the distance between the opposite sides of the nanometer scale junction is reduced to a larger extent than the effectively applied tip displacement due to an attractive interaction (up to 4.7 Å). By reducing the tip-substrate distance below 4.7 Å, the interaction becomes repulsive. At such tip proximity, the adatom-substrate distance (defined as the vertical distance between the Co adatom and its first nearest neighbor) is strongly reduced while the distance between the tip and adatom is only slightly decreased. This implies that the Co adatom shifts towards the substrate. As a consequence when the point contact configuration is reached, the Co-Cu(111) surface distance is greatly decreased comparing to the equilibrium distance predicted for the tunneling condition [dotted line in panel 4.3(b)].

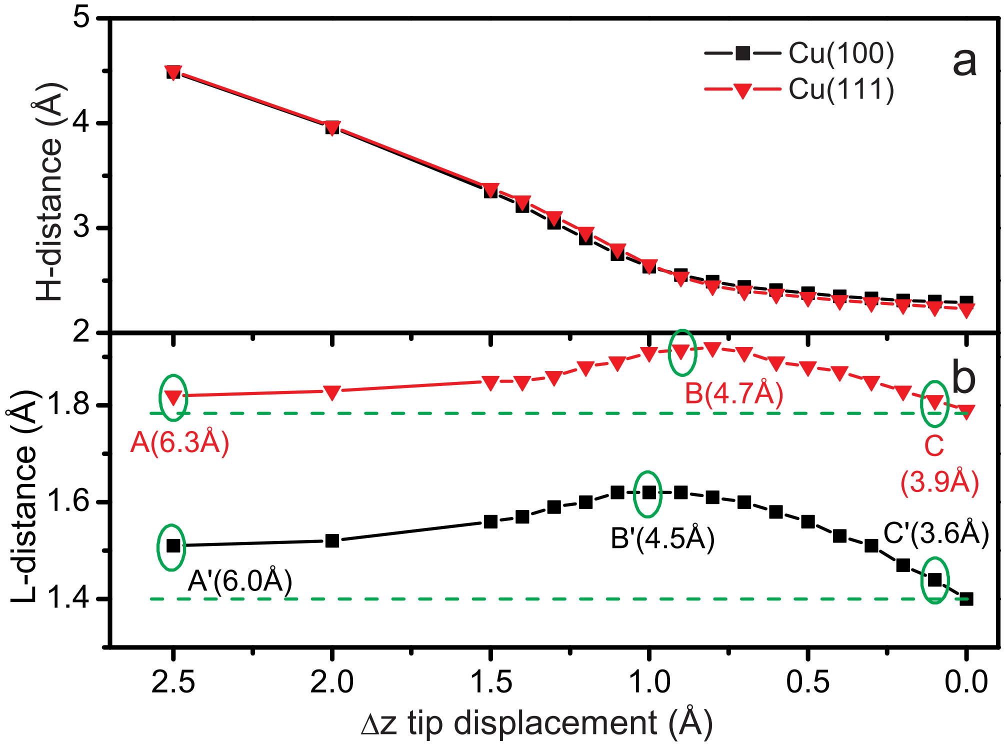

Figure 4.3: Atomic relaxation at the single Co atom junction as a function of the tip displacement. The initial tip-adatom distance (H) is the same for Cu(111) and Cu(100) surfaces. The adatom-substrate (L) distances for Co adatom on the two surfaces is shown in panel (b). Δz is the displacement of the STM tip. The dashed lines show the Co-substrate distance in point contact conditions. (A), (B), and (C) indicate the position where the LDOS shown in Fig. 3 have been calculated; the values in the brackets are the tip-substrate distances for these three positions.

It is important to compare atomic relaxations in junctions on the closed-packed Cu(111) surface with those on the Cu(100) surface. These results are presented in Fig.4.3. The general trend of attractive and repulsive interaction of tip-adatom and surface can be observed in both cases. However, differences in the atom dynamics under the influence of the tip and in the adatom-surface distance are obvious. Specifically, under the influence of the tip the Co impurity is pushed deeper towards the Cu (100) surface in the point contact regime [dotted line in panel Fig.4.3(b)] than that in the tunneling regime. Therefore, the hybridization between d states of the Co adatom with the sp states of the surface increases. Considering that a reduction in tip-adatom distance by 1 Angstrom typically results in ten-fold increase of the tunneling current, it can be concluded from the above discussed results that the dynamics of the relaxations caused by the tip must have profound influence on STM and STS results.

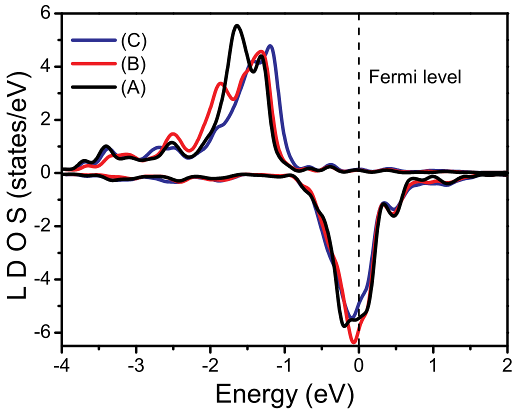

Figure 4.4: Spin-polarized LDOS for d states of the Co adatom on the Cu(111) surface. The curves are calculated tip-substrate displacements as denoted in Fig.4.3

.

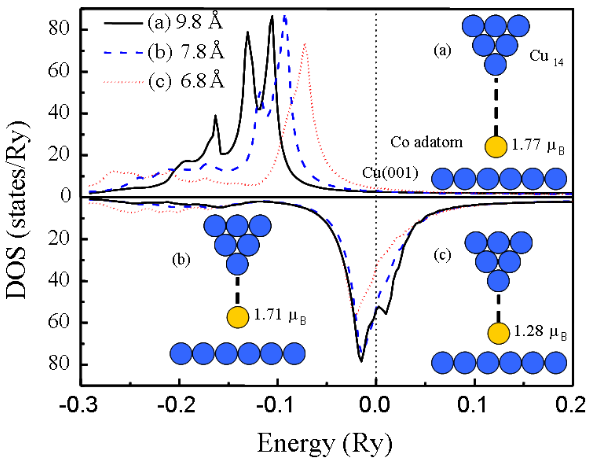

Figure 4.5: Influence of the tip proximity on d states of Co adatom on Cu(001) at three different tip-substrate separations. The figure is taken from[108].

.

To demonstrate the effect of the tip on electronic properties of single magnetic adatoms, we have performed *ab initio* calculations of the local density of states (LDOS) in a fully

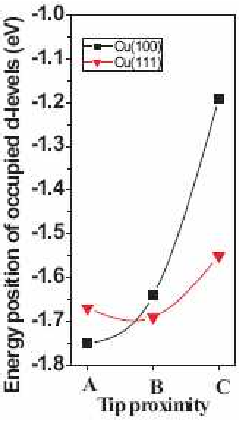

Figure 4.6: Influence of the tip proximity on the d levels center of Co atoms on Cu(001) and Cu(111) surfaces. The lines connecting the points are a guide to the eye.

.

relaxed geometry for three different tip-adatom distances denoted as A, B and C in Fig.4.3. Spin-polarized calculations were performed within LCAO formalism by means of density functional theory implemented in SIESTAÅ[67]. The geometry was optimized by SIESTA until all residual forces on each atom are smaller than 0.01 eV/. LDA has been used for the exchange and correlation potentials, and a 250 Ry energy cutoff is used to define real-space grid for numerical calculations involving the electron density. Core electrons of all elements are replaced by nonlocal norm-conserving Troullier-Martins pseudopotentials. Valence electrons of the Cu substrate are described using a double-ζ plus polarization atomic orbital basis set, and a triple-ζ plus polarization atomic orbital basis sets for the Co adatom. The displacements of the Co adatom at three tip-adatom distances calculated by the MD method are 0.02, 0.21, and 0.05 Å, respectively. They are 0.01, 0.26, and 0.08 Å obtained from SIESTA code, coinciding with the MD results very well. Relaxation of the atoms in the tip is also taken into account in our calculations.

In Fig.4.4, d states of the Co adatom on Cu(111) are shown for different tip-substrate separations with the energies given with respect to the Fermi level. For comparison, we also present d state on the Co adatom on Cu(100) at different tip-substrate separations[108], as shown in Fig.4.5. It can be seen that only d states of the Co adatom on Cu(111) are slightly affected by the tip-adatom interaction. In contrast, for the Co adatom on Cu(100) at distances between 4.5 and 3.5 Å, the majority of d states are drastically influenced by the interaction between the tip and the adatom.

Moreover, on Cu(111) surface, the energy differences U between the center of the occupied spin-up states (or majority states) and the center of the partially unoccupied spin-down states (or minority states) at three tip-substrate separations are nearly the same. Consequently, the magnetic moment of the Co adatom (1.99 μ_B, 1.96 μ_B, and 1.78 μ_B, respectively) at these three tip-substrate separations are only slightly affected by the tip proximity. On the contrary, a large energy shift of d states is seen for the Co adsorbed on Cu(100) surface (Fig.4.5), which leads to a strong reduction of the magnetic moment of the

Co adatom on Cu(100) (down to about $1.2\mu_B$ in the contact regime). A comparison of the energy position of the occupied d levels is shown in Fig.4.6. On both surfaces the position of the occupied d levels shifts towards higher energies under the influence of the tip proximity. On the Cu(111) surface this shift is, however, much smaller than that on Cu(001) surface. On Cu(100) the substantial change in the occupation of the d states is reflected by the increase of the Kondo temperature in point contact. The difference in the change of the Kondo temperature on Cu(111) and Cu(100) is caused by different atomic relaxations which occur on both substrates. For all tip positions the distance between the Co adatom and Cu(111) is significantly larger than that that on Cu(100) (see Fig.4.3 (b)). Therefore, the hybridization between d states of Co adatoms with sp electrons of the substrate is weaker on Cu(111). As a result, only very small changes in the LDOS of Co adatoms are found on Cu(111). Accurate calculations of the Kondo temperature for our system are, however, not straightforward. Nonetheless, the theoretical predictions and the experimentally observed Kondo temperature in the point contact regime follows the trend described by the model proposed by Wahl *et al.*[113]. The increase of the occupation of the Co d states effects sensibly the Kondo temperature on Cu(100) and almost negligibly on the Cu(111) surface.

Finally, we comment on calculations of the Kondo temperature for magnetic junctions. The Kondo effect is a genuine many-body phenomenon, and therefore the results of ground state DFT simulations cannot be directly related to the Kondo temperature. In several works the Kondo temperature has been calculated exploiting the Anderson impurity model[34, 117]:

$$T_K \propto \frac{1}{k_B}\sqrt{\frac{2\Delta U}{\pi}}exp\left[-\frac{\pi}{2\Delta}\left(\left|\frac{1}{\epsilon_d}\right|+\left|\frac{1}{\epsilon_d+U}\right|\right)^{-1}\right] \tag{4.3}$$

Within the single-orbital Anderson model, Δ is the width of the impurity state. In the case of several impurity levels, as for the Co adatom, it denotes the broadening due to the crystal field splitting between these levels. The parameter ϵ_d is the energy difference between the occupied d-band center and the Fermi level, and U is the on-site Coulomb interaction between spin-up and spin-down states. The crystal field splitting shows up as the half-width of the spin-up density of states of the d band. Now, the problem is to find the the center of the occupied d band of the impurity, its half-width Δ, and the on-site Coulomb interaction U. The on-site Coulomb interaction can be calculated between spin-up and spin-down states by estimating the center of the d band for occupied and unoccupied states. The crystal field splitting Δ can be obtained by fitting the peaks in the DOS to a Gaussian, which is not very precise and the evaluations of the Kondo temperature T_K would reflect some errors.

Néel *et al.*, [109] used this model to estimate the dependence of the Kondo temperature on the tip-substrate for a Co adatom on Cu(001) surface and found the increase in the Kondo temperature during the tip approaching. However, there is a great difference in the values of the Kondo temperature between the experimental and the theoretical results. From the equation of the Anderson model, it can be seen that the Kondo temperature exponentially depends on the crystal field splitting Δ. Even a small change of the Δ would result in a big difference in the Kondo temperature. To get a precise Kondo temperature, as pointed by Újsághy *et al.*,[34] details of the band structure have to be taken into account in order to reproduce the tip-substrate dependence quantitatively.

4.3 Interaction between the STM tip and adatoms at the atomic scale: tailoring an adatom dynamics

Here, we discuss our results for an adatom motion on metal surfaces caused by the interaction with the tip. We reveal the effect of the STM tip on the surface diffusion of a single Co adatom on a Cu(111) surface. The main goal of this section is to resolve the energy landscape for the diffusion of a Co adatom in the presence of the tip. Atomic-scale calculations by means of MD method and *ab initio* studies are presented. It is known that the STM tip causes modification in the energy landscape in its vicinity which, in turn, controls the characteristic of an atomic manipulation[118]. Detailed knowledge of the energy landscape in the presence of the tip may help control atomistic processes such as chemical reactions, growth and nanostructuring. Several interesting theoretical studies have been already perfomed in this field. For example, a lowering of the activation energy for an Au atom diffusion on Au(100) surface in the presence of a Au tip has been reported[119]. Also a significant lowering of the diffusion barrier for a Cu adatom on Cu(111) with Cu(111) tip toward the surface and increasing the barrier for the motion away from the tip has been found[10]. A simple scenario explaining the effect of the tip on adatom diffusion is the following: at particular heights, the adatom gains new bonds with the tip atoms, which makes its motion more favorable toward the tip than away from it. Another example of the effect of the STM tip on energy landscape has been demonstrated in both calculations and experiments for Ag(111): a Ag adatom can be extracted from a Ag mound by a Ag tip through the pulling mode[21]. Recent molecular dynamics calculations suggest that it could be possible to extract Cu atoms from Cu clusters affecting the energy landscape by the STM tip[118]. A significant influence of the tip on atomic diffusion on the top and the edges of mesosocopic Co islands on Cu(100) has been revealed in MD calculations[120]. It has been shown that for certain tip-surface separations, the hopping diffusion of Co adatoms on the top of Co islands and the upward mass transport at the edge of the islands can be strongly enhanced. The size-dependent strain relief in the islands[121, 122] caused by the tip and the substrate has been shown to play very important role in atomistic processes on islands.

To the best of our knowledge, the effect of the STM on magnetic adatoms on metal surfaces has not been studied yet. Such studies will be of great interest for "atomic engineering" of magnetic nanostructures.

The model for our calculations is presented in Fig.4.7. Co adatom is shown with a red ball, Cu(111) substrate and Cu tip are sketched with blue spheres. The adatom is placed initially aside the tip apex. Then we start to move adatom towards the tip. The direction of this movement is shown with a dashed red line in Fig.4.7 b. The position of the tip apex is pointed with a yellow star. Nearest to adatom absorption sites are marked with numbers. Distances between the Co adatom (red star in Fig.4.7 b) and 1st, 2nd, 3rd and 4th hollow sites are 1.5, 2.5, 3.0 and 3.9 Å, respectively.

At each point the adatom, the Cu substrate and the Cu tip are relaxed and the total energy of the system is calculated. We expect that the energy landscape will depend on the tip geometry and its position. First, we have performed calculations for a sharp tip made of 10 Cu atoms arranged as a pyramid with fcc (111) stacking of atomic planes. Here we describe the tip position with the vertical distance H between the tip and the substrate, and with the vertical distance L between the tip apex atom and the Co adatom (see Fig.4.7).

In our calculations we used the many-body interatomic potentials formulated in the sec-

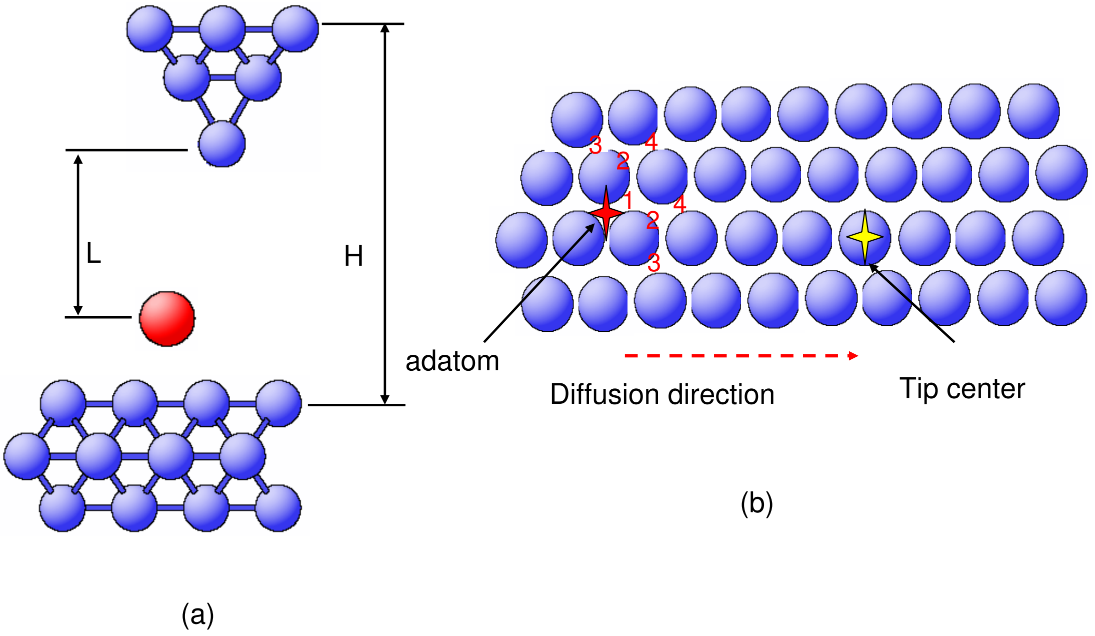

Figure 4.7: Schematic set up for the calculations. (a) H is the vertical tip-substrate distance, L is the vertical tip-apex adatom distance. (b) Top view of the surface. Red star is the initial position of the adatom and the yellow star is the position of the STM tip. Numbers denote the Nth nearest neighbors of the adatom.

ond moment of tight-binding approximation with parameters fitted to *ab initio* calculations[116].

At a short tip-substrate distance 7.9 Å (Fig.4.8 a), the Co adatom jumps from fcc3 site to fcc4 site (these sites are pointed in Fig.4.8 c) with the diffusion barrier of 19 meV. Such atomic event can be operative only at temperature larger than 6 K. If the adatom is closer to the tip apex it moves towards the tip without the barrier. When the tip-substrate distance is increased to 8.5 Å (Fig.4.8 b), the barrier for the Co adatom to jump from fcc3 site to hcp3 is 30 meV. And the barrier for jumping from hcp3 to fcc4 site is only 5 meV. We conclude that in both cases Co adatom can hop from the hcp site to the fcc site towards the tip. The displacement of the adatom in this case is 1.48 Å. The driving force which "pushes" the adatom to move towards the tip is mainly caused by electronic interactions between the adatom and the tip apex. To prove it, we have calculated the tip-adatom interaction by means of *ab initio* KKR Green's function method[123](calculations have been performed together with P. Ignatiev, MPI Halle). The tip constructed of 4 Cu atoms was placed at 2.1 Å, 4.2 Å and 6.3 Å above Cu(111) surface at distances ranging from 0 Å up to $\sim$ 10 Å. The interaction energy was determined from the total energies at short tip-adatom separations and the force theorem and single particle energies were used otherwise[124]. The interaction energies are plotted in Fig. 4.9. It is evident that a strong attraction appears when the tip is situated close to the adatom. This effect can

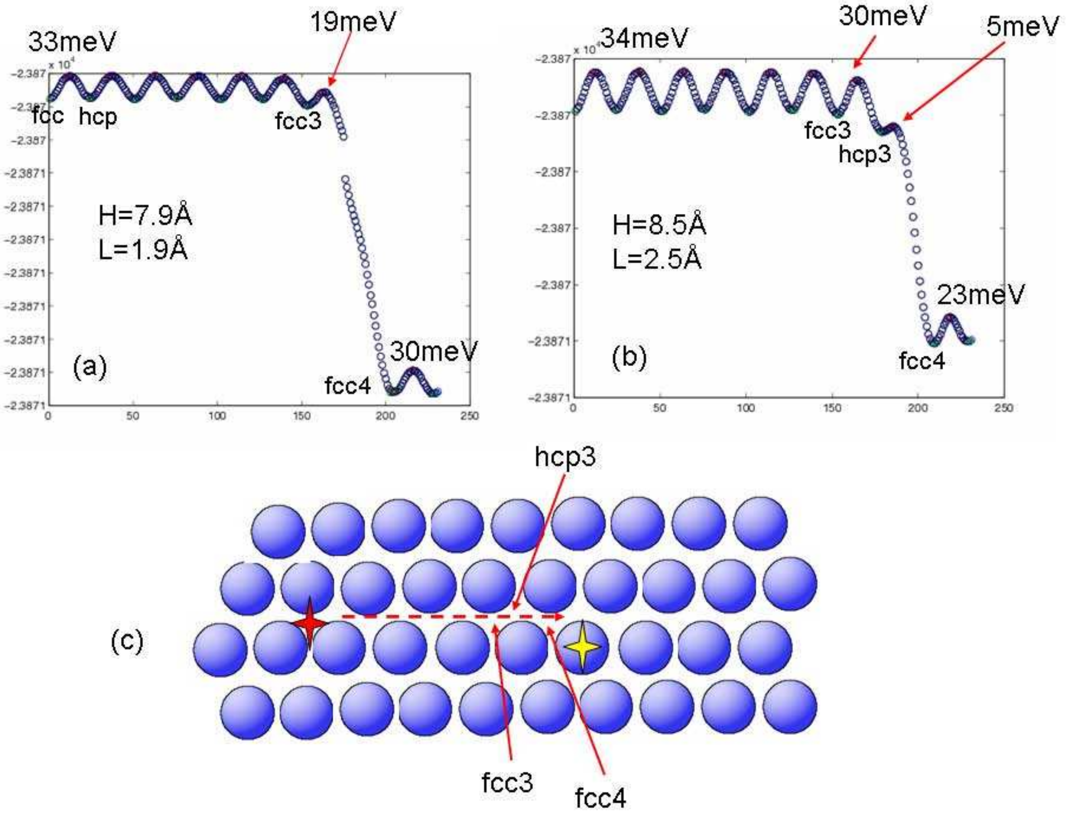

Figure 4.8: Diffusion barriers of the Co adatom under a sharp tip at different tip-substrate distances: (a) 7.9 Å, (b) 8.5 Å. fcc and hcp positions in (a) and (b) are marked in (c). The Y axis is the energy and its unit is eV. In calculations, even for the same tip-substrate distance would have different tip-adatom distance, which is due to the relaxation effect.

be explained by the formation of a direct bond between the adatom and tip atoms. The attraction almost disappears at separations larger than ∼ 6 Å. These results suggest that when the tip approaches the surface all the barriers for adatom jumps between hollow sites situated closer than 6 Å from the tip apex can be drastically reduced. As a result the adatom can move from the tip periphery towards its center. Surface state electrons were found to play a minor role in the studied phenomena due to the density vanishing exponentially to the vacuum.

To extend our study, we have performed calculations with different blunt tips. Our first blunt tip is modeled by a pyramid arranged in fcc(111) stacking with 3 Cu atoms in apex plane (Fig4.10 a). If the tip-substrate distance equals to 7.8Å, the diffusion barrier for the Co adatom jumps from fcc2 to fcc3 site under the tip is 7 meV (Fig.4.10 c). The displacement distance is around 2.55 Å. The further displacement is suppressed by strong adatom-tip repulsive force, which increases the barrier of diffusion from fcc3 site to fcc4 site up to 92 meV. At larger tip-substrate distances, however, this barrier disappears due to significant reduction of adatom-tip interaction. Energy profile for tip-substrate distance of to 8.2Å is demonstrated in Fig.4.10 (d). If adatom has already moved to the site fcc3, the tip retraction pushes it into the site hcp3 (Fig.4.10 (d)) and the total displacement is 4Å.

Another blunt tip which have been probed in our calculations is a pyramid stacked in

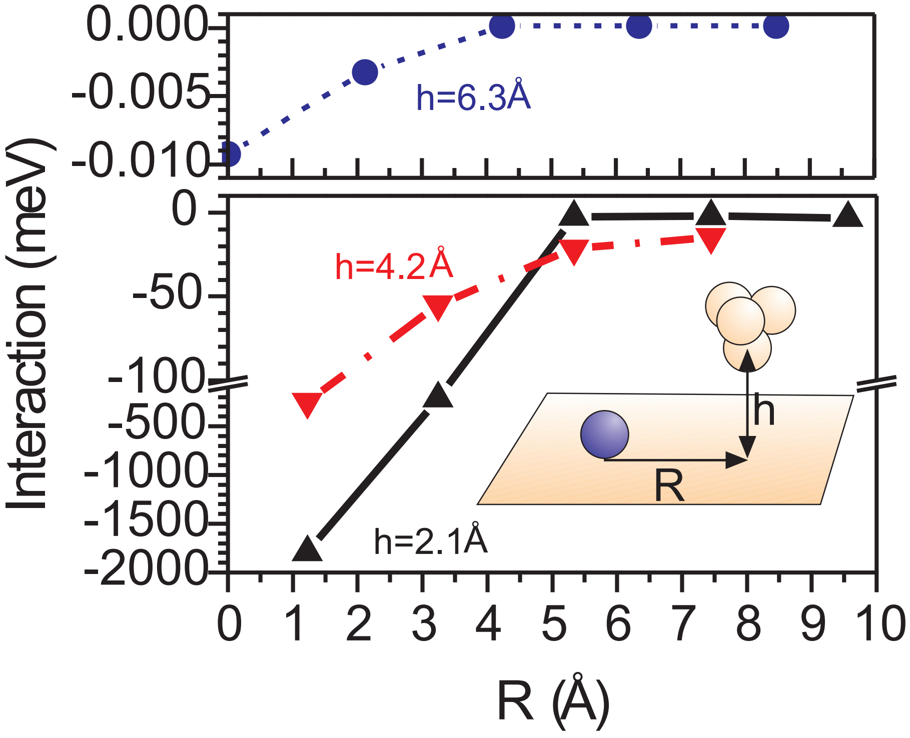

Figure 4.9: Energies of the interaction between the tip and adatom calculated for various tip heights h and various tip-adatom separations R. These plots give a clear evidence of a significant attraction of the adatom to the tip.

fcc(111) order with 6 Cu atoms in the apex plane (Fig.4.11 a). At a short tip-substrate distance (7.9Å), the diffusion barrier for the Co adatom to jump from site hcp1 to site fcc2 is 13 meV. If the adatom is placed closer to the tip center it gets to the point pos1 under the tip without any barrier. The displacement in this case is 2.9Å. The further movement could be blocked at very low temperature by the barrier of 14 meV caused by the adatom-tip interaction. The retraction of the tip from the surface results in the disappearance of this barrier (see Fig.4.11 d for H=8.6Å) and the adatom gets at the tip center. The total displacement in this case is 4Å. These results give a clear evidence that energy landscape for a single adatom on the surface can be ”engineered” by choosing the tip position above the surface and the shape of the tip.

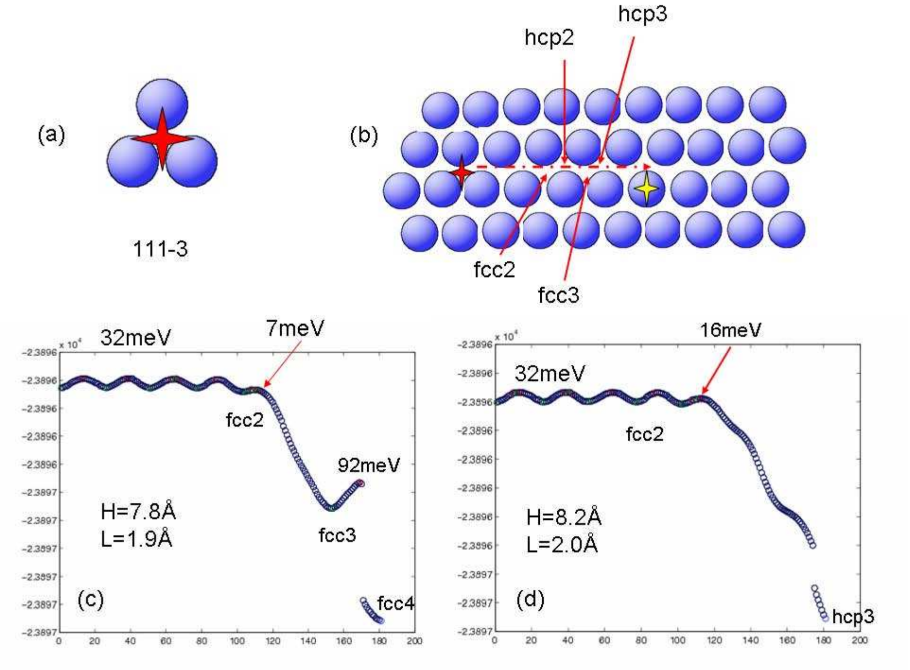

Figure 4.10: (a) Tip apex in the blunt tip and the red star is the center of the tip-apex. (b) Different positions on Cu(111) surface. Diffusion barriers of the Co adatom under the blunt tip at two tip-adatom distances: (c) 7.8Å and (d) 8.2Å.

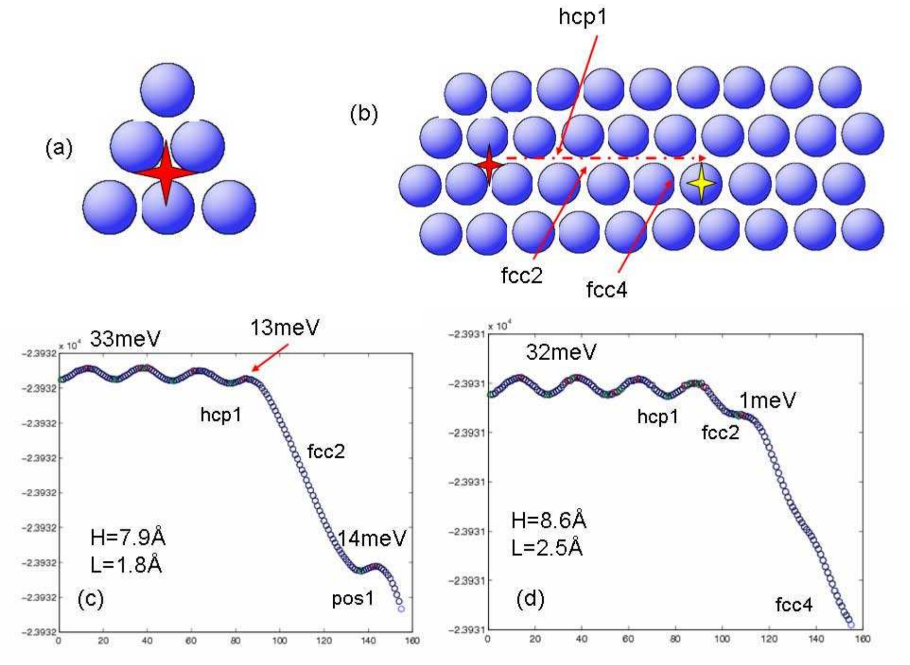

Figure 4.11: (a) Tip apex in the blunt tip and the red star is the center of the tip-apex. (b) Different positions on Cu(111) surface. Diffusion barriers of the Co adatom under the blunt tip at two tip-adatom distances: (c) 7.9Å and (d) 8.6Å.

Chapter 5

Tailoring a single spin on metal surfaces by a magnetic STM tip

The control over magnetic ordering down to a single atomic magnet, such as a single atomic spin on a surface, is of great interest for spintronics devices. The delicate interaction between the adatom and its surrounding, mediated by a supporting substrate or host, determines the resulting behavior of the spin orientation. The spin directions of interacting adatoms can be driven into either parallel (ferromagnetic), antiparallel (antiferromagnetic) alignment, or even noncollinear, depending on the sign of the exchange coupling. Recent scanning tunneling microscopy (STM) experiments demonstrate the ability to measure the exchange coupling between spins[125, 37]. The magnetic exchange interaction can be obtained from the excitation spectra of a magnetic chain with different length [125] or the Kondo resonance of the interacting adatoms at various separations[37]. One can also use the magnetic exchange coupling to control the spin state of a single magnetic adatom by depositing it on an insulating thin film[6] or on magnetic islands[107, 126]. Moreover, Heinrich *et al.,*[127] have observed a spin-flip phenomenon for a single manganese adatom on a metal oxide island. In all the above experiments, the STM tip is only used as a tool probing the status of adatoms on surfaces, but the influence of the STM tip on electronic and magnetic properties of adatoms has not been investigated. However, theoretical and experimental studies have shown that electronic and magnetic properties, as well as the conductance behavior of a single adatom on metal surfaces strongly depend on the tip-surface distance[110, 108, 109, 114].In this chapter we show that exchange interaction between the magnetic STM tip and the magnetic adatom (a single atom junction) can be manipulated by changing the distance between the tip and the surface. We reveal that a direct interaction between d-states of the tip and the adatom at short tip-substrate separations leads to the antiferromagnetic coupling between the tip and the adatom, while at large distances an indirect interaction between d-states of the tip and the adatom via sp electrons leads to a ferromagnetic coupling between them. We perform a comprehensive study of a spin-dependent charge transfer between the tip and the adatom at different positions of the tip above the surface. Our study demonstrates the possibility of controlling a single spin on metal surfaces exploiting the magnetic STM tip. We concentrate on the magnetic Cr tip interacting with 3d adatoms (Cr, Mn, Fe, Co) on Cu(001).

5.1 Description of ab initio calculations

In order to gain insight into the magnetic interactions between the spin polarized STM tip and single magnetic adatoms on Cu(001) surface, we have performed first-principle calculations based on the density functional theory (DFT) within the generalized gradient approximation (GGA) implemented in VASP code[59, 60, 61, 62], with the exchange-correlation function of Perdew and Wang (PW91). In order to describe the ion core electrons, the projector augmented wave (PAW) potentials are used. This approach keeps the computational efficiency of pseudopotentials by substantially reducing the number of plane waves required, but, at the same time, it is an all-electron scheme providing very realistic valence-electrons distributions important for studying the magnetic properties of the system. The electronic states are expanded in terms of plane waves with the number restricted by maximal kinetic-energy cutoff of 400 eV. All parameters in the calculations are chosen to converge the total energy to 10^{-5} eV.

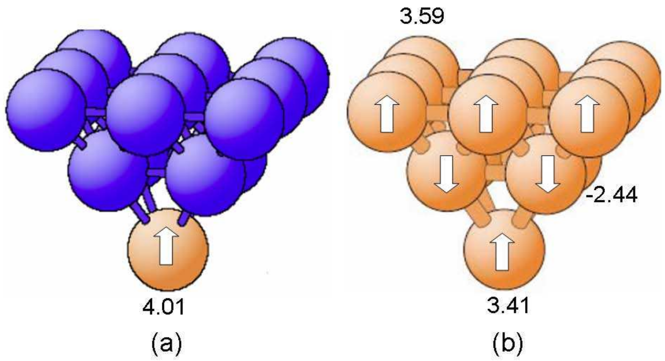

Figure 5.1: Two different types of the STM tips used in calculations. The arrows in the figure are the spin directions of atoms. Presented numbers depict the magnetic moment(μ_B) of the Cr atoms. Blue balls are the Cu atoms and yellow balls are the Cr atoms.

The coupled system consisting of the tip, the adatom and the substrate is calculated in a supercell geometry. In two dimensions (2D) our supercell corresponds to a (4×4) unit cell with respect to the Cu(001) surface. The Cu(001) substrate is modeled by a slab of 5 layers of Cu atoms with 16 Cu atoms in each layer. The Cr adatom is placed above the hollow site of the top Cu layer. In our model the distance between the tip and its image in its neighbor is larger than 10 Å, thus interaction between them is negligible. Three Cu bottom layers of the substrate and the top layer of the tip are fixed, all the other atoms are fully relaxed. The geometries are optimized until all residual forces on each atom are less than 0.01 eV/Å.

One of the most delicate aspects in modeling the STM experiments is the geometry used for the tip. Ideally, the model for the tip should consist of thousands of atoms to mimic tips used in real experiments. However, in practice one is limited by the computational resources required for the calculation. Fortunately, the interaction between the tip and sample is dominated by the foremost atoms of the tip[110] due to the exponential decay of the wavefunctions. There are two main approaches to model a metal tip: i) the cluster model, where the shape and the atomic arrangements can play a role in determining the electronic properties of the apex atom. ii) an extended substrate model (as 3D supercell or 2D slab systems), where the metallic properties of the system could be better represented[110].

In our calculations, we use a cluster model for the tip. The following two approaches for the tip structure have been investigated: (1) the tip is modeled by a pyramid consisting of 13 Cu atoms and one Cr atom at the tip-apex (denoted as single-Cr tip in this work), and (2) by a pyramid consisting of 14 Cr atoms (denoted as 14-Cr tip in this work). These two models are presented in Fig.5.1. The top layer of the tip is fixed while atomic positions for other atoms in the tip are determined by a fully relaxed geometry.

Since the Cr tip has an antiferromagnetic ground state[128], the spin direction of atoms in the second layer of the tip is set to be antiparallel to the spin direction of atoms in other two layers, as shown in Fig.5.1. We restrict ourself only to the collinear magnetic structure of the tip, while a more complicated spin configurations in the tip could exist. Our studies have revealed that the exchange coupling in the single atom junction is mainly determined by the interaction between the adatom and the tip apex. Our calculations have shown that the magnetic moment of the Cr tip apex decreases from 4.01 μ_B to 3.41 μ_B with increasing number of Cr atoms in the tip from a single Cr atom to 14 Cr atoms.

5.2 Exchange interaction between the tip and adatoms

First of all, we perform calculations of the interaction between the single-Cr tip and a Cr adatom on Cu(001) surface. The interaction between the 14-Cr tip with the Cr adatom will be discussed later. The single-Cr tip is approached vertically towards the Cr adatom on Cu(001) surface. In all calculations, the spin direction of the tip-apex is fixed (spin up), while the direction of the spin could be reversed for the Cr adatom (either to be spin up or spin down). At each tip-substrate separation, we perform calculations for parallel (P-configuration, the spin direction of the Cr tip-apex and Cr adatom to be parallel) and antiparallel (AP-configuration), as shown in Fig.5.2 (a). The tip-adatom distance d is the distance between the tip and the adatom without relaxations.

The magnetic interaction between tip and adatom can be inferred directly from the exchange energy E_{ex} defined as:

$$E_{ex}(d) = E_{ap}(d) - E_p(d)$$

and displayed in Fig.5.2 (b).

One can see that the exchange energy changes its sign when the tip approaches to the surface. At large tip-substrate distances, the energy difference between P- and AP-configurations increases and reaches its maximum (91 meV) at about 9.2 Å. At a short tip substrate separations, however, the exchange energy decreases and shows a clear changes in its sign at about 7.9 Å. The exchange energy increases to -42 meV at the tip-adatom distance of 7.7 Å. We did not decrease the tip-adatom distance further, which will increase the exchange energy to an even larger value. The negative value of the exchange energy indicates that the antiparallel alignment is energetically favorable, while for the positive value corresponds to a parallel alignment of spins. The central result of our study is the change of the sign of the exchange energy when the tip approaches the surface.

Now we turn to the discussion of the atomic relaxations in the single-atom magnetic junction.

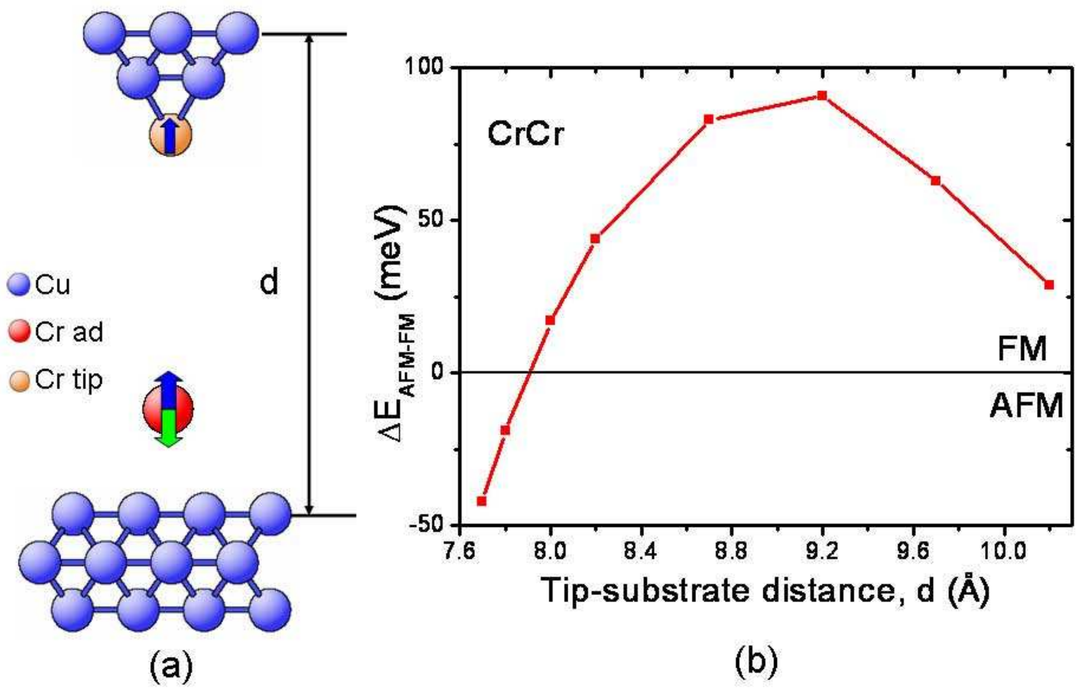

Figure 5.2: (a) Setup for calculations. The upward arrow in the tip-apex means that its spin direction is fixed to be spin up. Two arrows denote that the spin direction of the adatom can be reversed; d is the tip-substrate distance without relaxations. (b) Exchange energy as a function of the tip-substrate separation.

Displacements of the Cr adatom and tip-apex in parallel (P-configuration) and antiparallel (AP-configuration) configurations at different tip-substrate separations are plotted in Fig.5.3. It can be seen that the Cr adatom and the tip-apex show different relaxation behavior. When the distance between the tip and the adatom decreases, both the tip-apex and the adatom exhibit strongly vertical displacements. For the P-configuration, in the range between 10.2 Å and 9.2 Å, the tip-apex is pulled down, while the adatom is pulled up. At this stage the attractive interaction between the tip and the adatom is the driving force for the observed atomic relaxations. However, at a short tip-substrate separation, the repulsive interaction between the tip and the adatom plays an important role. As can be seen from figure, at a short tip-substrate separation, the Cr tip-apex is pushed up while the adatom is pushed down.

Checking Fig.5.3 carefully, one can see that for short tip-substrate distances displacements of the tip-apex and the adatom in P-configuration are larger than those in AP-configuration. As we have already discussed, at a short tip-substrate distances, the interaction between the tip-apex and the adatom is repulsive. Moreover, at a short separation, two electrons with the same spin direction repel each other, while two electrons with the opposite spin direction attract each other. Therefore, at a short tip-substrate distance, the repulsive forces between the tip-apex and the adatom in P-configuration would be stronger

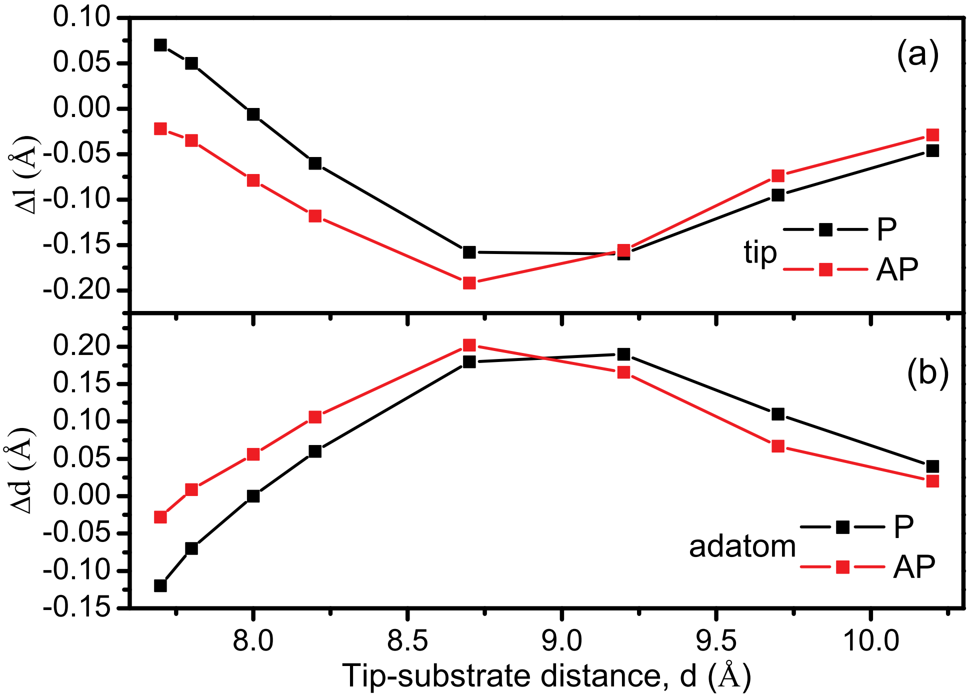

Figure 5.3: Atomic relaxation as a function of the tip-substrate separation for parallel and antiparallel configurations; (a) $\Delta l = l_0 - l$ is the displacement of the tip-apex without and with the tip-adatom coupling; (b) $\Delta d = d - d_0$ is the displacement of the adatom with and without tip-adatom coupling.

than that in AP-configuration. At this stage displacements of the tip-apex and the adatom in P-configuration are larger than those in AP-configuration. To reveal the effect of atomic relaxations on the exchange interaction between the tip and the adatom we have calculated the exchange energy without any relaxations. Results are presented in Fig.5.4. In both P- and AP-configurations, the initial tip-adatom distance is the same. Results for relaxed and unrelaxed geometries look qualitatively similar: the spin direction also changes from the P-configuration to the AP-configuration at the tip-adatom distance about 7.9 Å. Still, antiferromagnetic alignment is energetically favorable at short-adatom separations. However, the exchange energy is quantitatively different. At the tip-adatom distance of 7.7 Å, the exchange energy in the unrelaxed configuration is nearly three times larger than that in the relaxed configuration.

In order to check the influence of the tip size on the exchange energy, we have also carried out fully relaxation calculations for the exchange energies using the tip consisting of 14 Cr atoms (denoted as 14-Cr tip, see Fig.5.1 (b)). At the tip-substrate distance of 9.2 Å, the energy difference between AP- and P-configurations is about 77 meV, while it is -84 meV at 7.7 Å. Although exchange energies are quantitatively different for the single-Cr tip and the 14-Cr tip, the trend for both tip models is the same. For 14-Cr tip, the exchange energy still keeps a negative value at short tip-adatom distances. In other words, at short

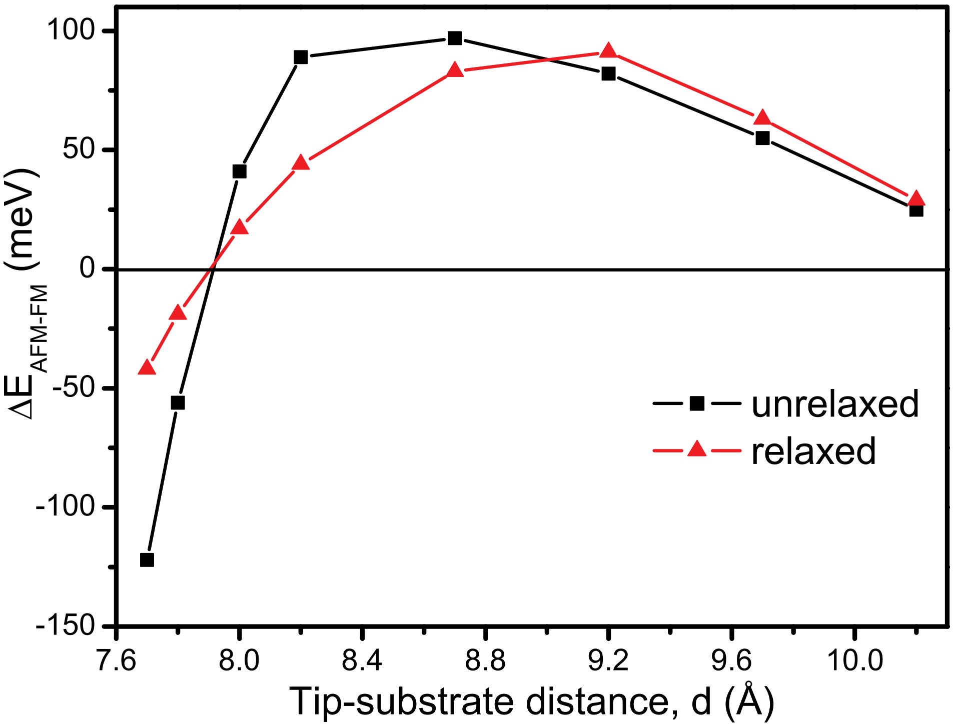

Figure 5.4: Exchange energy as a function of the tip-substrate separation with and without relaxation.

tip-adatom distances, the antiparallel alignment of spins of the tip apex and the adatom is energetically more favorable.

We have also studied the exchange interaction between the Cr tip and other different magnetic adatoms such as Mn, Fe and Co. Results presented in Fig.5.5 reveal the following interesting trends. First of all, for all the magnetic adatoms M (M=Mn, Fe and Co), the exchange energy changes its sign at a short tip-adatom distance. At a large tip-adatom distance, the exchange energy is positive, which means that spin directions of the Cr tip and a magnetic adatom M would prefer to be parallel. A large negative exchange energy at a short tip-adatom separation denotes that an antiparallel configuration is energetically more favorable. These results indicate that it is in general true that the spin direction of a single magnetic adatom can be controlled with a spin polarized STM tip by changing its position above adatoms.

The Fig.5.5 also shows that the Co adatom changes its spin direction at the tip-adatom distance of about 10 Å. Fe and Mn adatoms change their spin directions at the tip-adatom distance in the range between 9.2-9.4 Å and 9.0-9.2 Å, respectively. As it has been discussed before, the Cr adatom changes its spin direction only at a very short tip-adatom distance in the range of 7.8-8.0 Å. In other words, going from Cr to Co adatom, the tip-adatom distance where the adatom changes its spin direction increases.

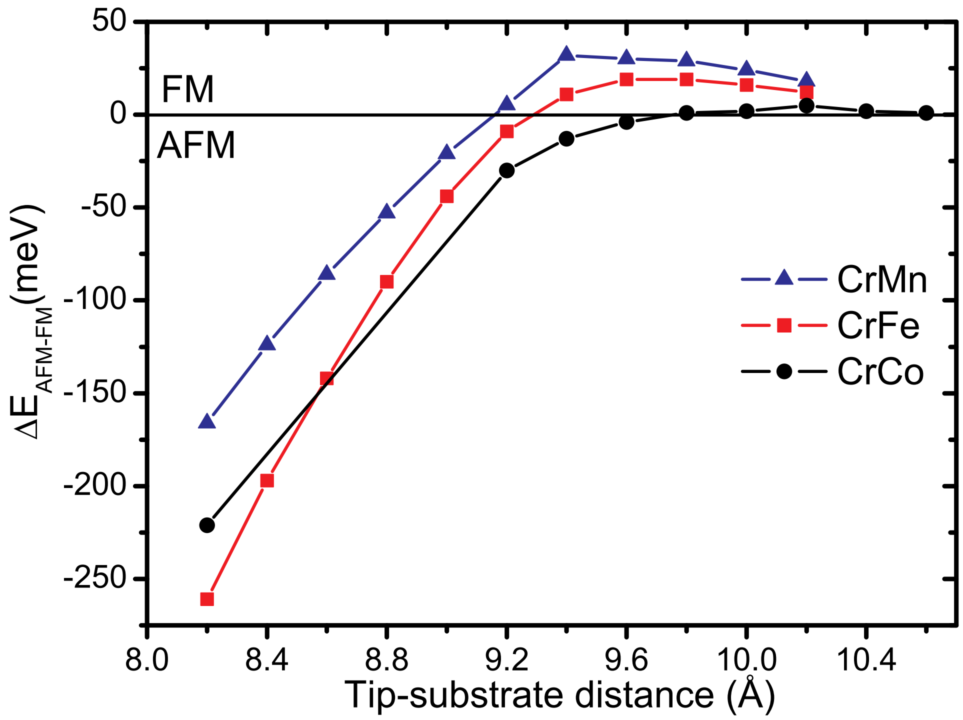

Figure 5.5: Exchange interaction between the Cr tip and magnetic adatoms M (M=Mn, Fe and Co).

This interesting trend is closely related to the spin splitting (energy difference between the center of the spin up and spin down states) of the magnetic adatoms. The spin splitting decreases from the Cr atom to the Co atom. The exchange energy changes its sign due to the charge transfer between the tip and the adatom. To go more deeper insight effects reported above we have done the investigation of the charge transfer between the tip and adatoms as will be discussed in the next section.

5.3 Spin-dependent charge transfer in the magnetic junction

The origin of exchange interactions can be traced to the different electronic structure of the magnetic junction in the P- and AP-configurations. In order to study the nature of these interactions, the charge density difference for these two types of coupling at different tip-adatom separations should be analyzed in detail. We will concentrate on the spin-dependent charge transfer between the Cr tip and the Cr adatom on Cu(001).

The charge density of the Cr tip on Cr adatom at two tip-adatom distances 9.2 Å (P-configuration) and 7.7 Å (AP-configuration) are plotted in Fig.5.6(c), (d), in comparison with that of the isolate Cr tip (Fig.5.6(a)) and a single Cr adatom on Cu(001) surface (Fig.5.6(b)). Obviously, the charge density overlap between the tip and the adatom at a short tip-adatom separation is much stronger than that at a large separation. It is seen

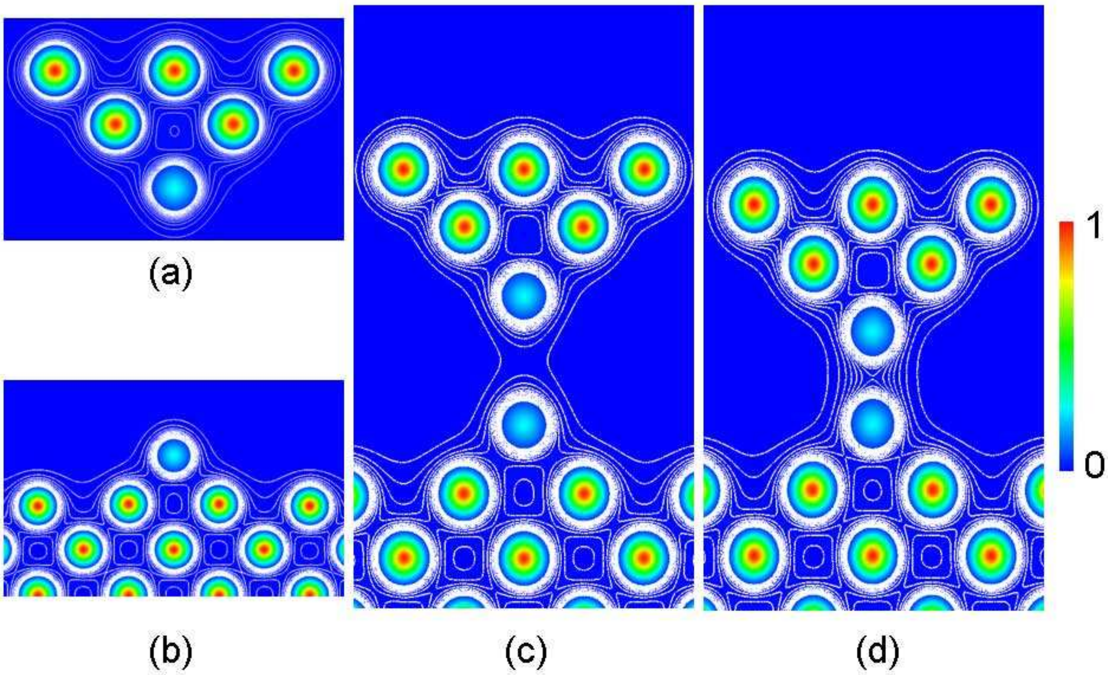

Figure 5.6: Cross-sectional charge density plots along the [110] direction for (a) an isolated Cr tip and (b) for a single Cr adatom on Cu(001) surface, total charge density for the Cr tip interacting with the Cr adatom at two different tip-adatom distances (c) 9.2 Å and (d) 7.7 Å. The slice is cut across the center of the Cr tip-apex and the Cr adatom. Contours in the panel start from $0e/\AA^3$ and change successively in steps of $5 \times 10^{-3} e/\AA^3$.

that the charge accumulation in the center area of the junction is strongly increased, which facilitates the charge transfer between the tip and the adatom. The Fig.5.7(a) shows the total charge density difference plot for the parallel and antiparallel configurations for the tip-adatom distance of 9.2 Å. The charge density difference is calculated by subtracting the charge density of the isolate Cr tip (ρ_{tip}) and that of the Cr adatom on Cu(001) surface ($\rho_{Cr/Cu(001)}$) from the charge density of the Cr tip on Cr/Cu(001) ($\rho_{tip-Cr/Cu(001)}$). At a large tip-adatom separation, in both P- and AP-configurations, the tip-apex and the Cr adatom lose electrons, and there is a small excess charge accumulation between Cr tip-apex and Cr adatom. The charge accumulation in the P-configuration is stronger than that in the AP-configuration which indicate that the P-configuration is more energetically favorable than AP-configuration (as shown in Fig.5.2).

It can be also seen that the charge densities on the nearest-neighbor Cu atoms beneath the Cr adatom and Cu atoms in the second layer of the tip are also slightly redistributed. The charge redistribution on Cu atoms is caused by their small magnetic moments induced by Cr adatom or Cr tip-apex.

Total charge density difference for the parallel and the antiparallel configurations for the tip-adatom distance of 7.7 Å is plotted in Fig.5.7(b). Both the tip and the adatom lose

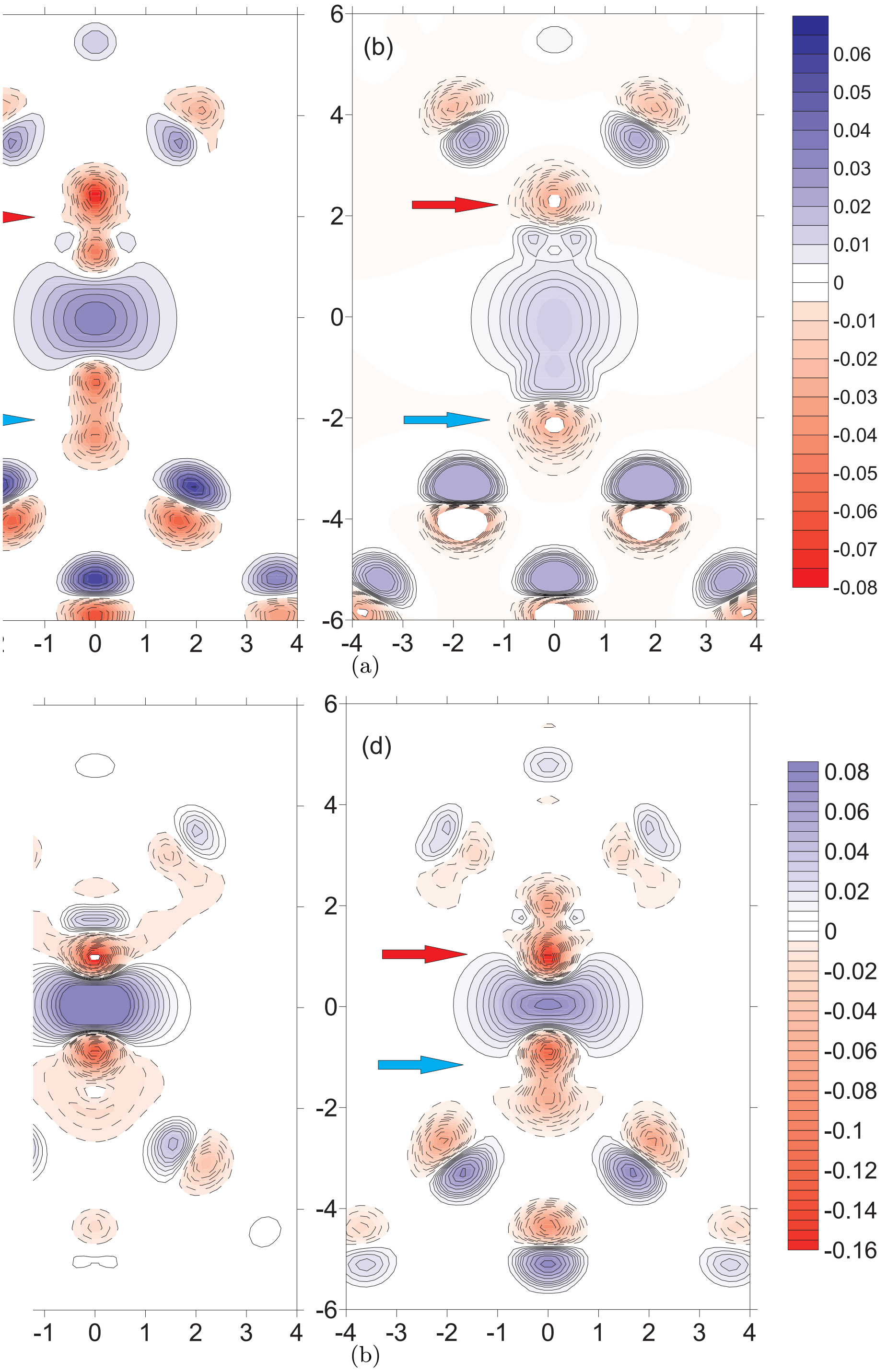

(a)

(b)

Figure 5.7: Charge density difference ($[\rho_{tip-Cr/Cu(001)}]$-$[\rho_{Cr/Cu(001)}]$-$[\rho_{tip}]$) for P- and AP-configurations for two tip-substrate distances; The red and blue arrows in the figure are the positions of the tip-apex and the adatoms, respectively. The slice is cut across the center of the Cr tip-apex and Cr adatom. (a) and (b) for the P- and AP-configurations for the tip-substrate separation of 9.2 Å. Contours in the panel start from $-0.08e/\AA^3$ and change successively in steps of $5 \times 10^{-3}e/\AA^3$; (c) and (d) for the P- and AP-configurations for the tip-substrate distance of 7.7 Å. Contours in the panel start from $-0.16e/\AA^3$ and change successively in steps of $5 \times 10^{-3}e/\AA^3$.

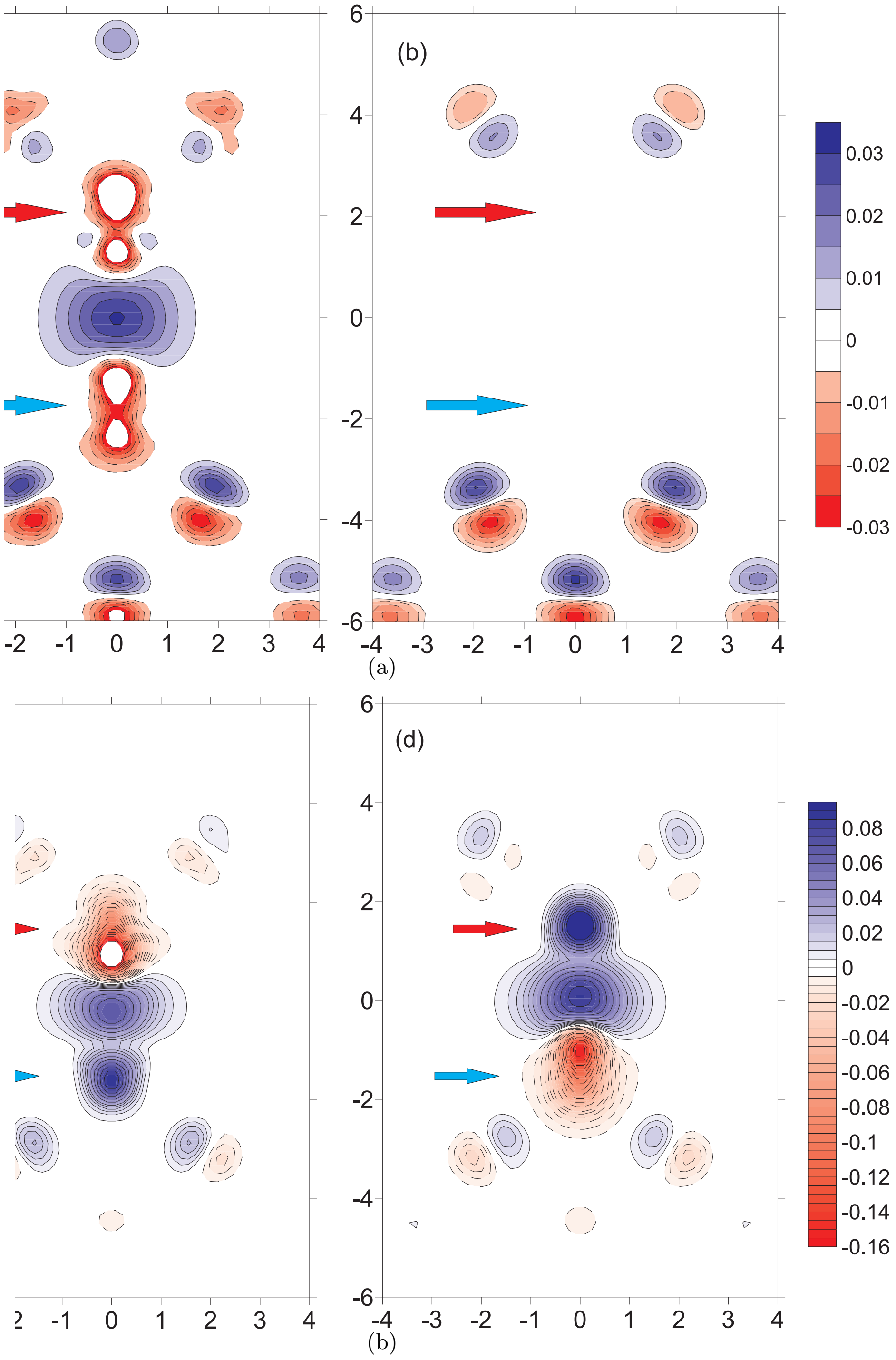

(a)

(b)

Figure 5.8: Spin-dependent charge transfer, $[\rho_{tip-Cr/Cu(001)}] \uparrow (\downarrow)$-$[\rho_{Cr/Cu(001)}] \uparrow (\downarrow)$-$[\rho_{tip}] \uparrow (\downarrow)$, in the junction for the two tip-substrate separations; The red and blue arrows in the figure are the positions of the tip-apex and the adatoms, respectively. The slice is cut across the center of the Cr tip-apex and the Cr adatom. (a) and (b) are the charge densities for the spin up and spin down electrons for the tip-substrate separation of 9.2 Å (P-configuration), respectively. Contours in the panel start from $-0.03e/\AA^3$ and change successively in steps of $5 \times 10^{-3}e/\AA^3$; (c) and (d) are the charge densities for the spin up and spin down electrons for the tip-substrate separation of 7.7 Å (AP-configuration), respectively. Contours in the panel start from $-0.16e/\AA^3$ and change successively in steps of $5 \times 10^{-3}e/\AA^3$.

some electrons. An excess charge strongly accumulates between the tip-apex and the Cr adatom, which implies a strong electronic interaction between them. However, the charge accumulation between the tip-apex and the Cr adatom in AP-configuration is larger than that in P-configuration which indicates that the antiferromagnetic coupling between the tip and the adatom is more energetic favorable, in agreement with the calculation of the exchange energy.

Comparing the total charge density difference for P- and AP-configurations at different tip-adatom distances, one can predict which configuration will be energetically more stable.

To understand the role of different spin channels in the charge transfer in the junction we present in Fig.5.8(a) the charge density difference for majority and minority electrons for the tip-adatom separation of 9.2 Å (P-configuration). We have found the transfer of the spin up electrons of the tip and the adatom to the area between them. However, for the spin down electrons, there is only very weak electron depletion, and the accumulation of the charge between tip and adatom is too weak to be visualized in the figure. When we put the Cr tip above the Cr adatom at large tip-adatom distances, spin down electrons are nearly unaffected, while spin up electrons accumulate in the range between the tip and the adatom. Therefore, there is the spin polarized charge transfer between the tip and the adatom, and this process includes only spin up electrons.

The spin-dependent charge density difference for the tip-adatom separation of 7.7 Å in AP-configuration is plotted in Fig.5.8(b). One can find that majority electrons deplete from the Cr tip-apex and accumulate between the tip and the Cr adatom. However, minority electrons deplete from the Cr adatom and accumulate between the tip and the adatom. In other words, there are two processes in the charge transfer, one is the transfer of majority electrons from the Cr adatom to the Cr tip-apex, and the second is the transport the minority electrons from the adatom to the tip-apex.

In order to make clear which orbitals are involved into the charge redistribution process, the projected density of states (PDOS) of the Cr adatom and the Cr tip-apex at the tip-substrate separation of 9.2 Å (P-configuration) is plotted in Fig 5.9. At a large tip-adatom separation, the direct overlap of the *d* states of Cr atoms is very weak. At the same time, a strong hybridization between the *d* and the *s* states can be observed for both of the tip-apex and the adatom. The interaction between *d*-states of the tip and *d*-states of the Cr adatom occurs via their *s*-electrons. In other words, an indirect interaction between the tip and the adatom determines the exchange coupling between them. Our results can be explained with the classical Zener model[129, 130]. We give a short summary of Zener's model: All unpaired electrons within each atom strive to attain the configuration of the lowest energy, in which according to Hund's rule, all spins are parallel to one another. Since the conduction electrons carry along their own spins unchanged as they wander from atom to atom, they are able to move within an environment of parallel spins only if the spins of all the d-shells are pointing in the same direction. This indirect coupling via the conduction electrons will therefore lower the energy of the system when the spins of the d-shells are parallel. This is so called a double exchange process. Ferromagnetism is possible only when the indirect coupling dominates over the direct coupling between adjacent d-shells. In the case of the magnetic junction considered in our work, the indirect coupling between the tip apex and the Cr adatom via sp-electrons promotes the ferromagnetic coupling at large tip-adatom separations. Now, let's discuss the results presented in Fig.5.5, as has been found that the ferromagnetic alignment in the junction is stable for Cr adatom for considerably smaller distance between tip and adatom, compared to Mn, Fe and Co. The results can be explained by the fact that wavefunctions are becoming more localized from Cr to Co. That

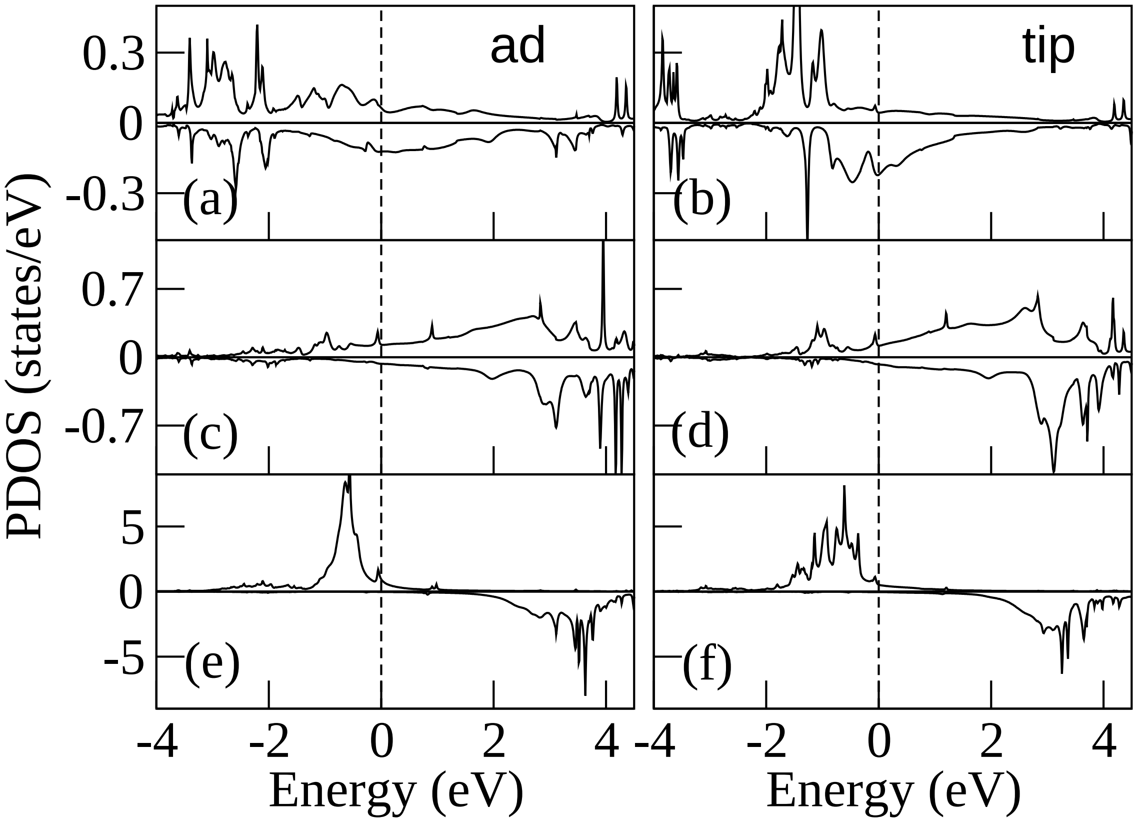

Figure 5.9: Projected density of states for the Cr adatom (left panels) and the Cr tip-apex (right panels) at 9.2 Å separation between them (P-configuration); a), b) $4s$ states; c), d) $4p$ states; e), f) $3d$ states.

means the amount of sp electrons which provide indirect coupling between tip and adatom also reduces going from Cr to Co adatom.

However, at short tip-adatom separations the scenario of the magnetic coupling in the junction is different. In this case a direct interaction between d-states of the tip and the adatom determines the ground magnetic state.

In order to describe the interaction of two magnetic impurities on neighboring sites in a free-electron-like host metal, a model was proposed by Alexander and Anderson[132]. In the framework of this model the virtual bound-state level of the impurity E_0 becomes spin split due to the exchange interaction: $E_0 - \frac{1}{2}\sigma Im$. Here I is the exchange integral and σ denotes the spin direction: σ=+1 for the majority-spin and σ=-1 for the minority-spin direction, and m is the magnetic moment. The corresponding densities of states are sketched schematically in Fig.5.10. For the ferromagnetic case one sees the bonding-antibonding splitting of the single-impurity peaks. In the antiferromagnetic case the single-impurity peaks repel each other and are slightly reduced in intensity. Additional satellite peaks with rather small weights appear at the 'wrong' energy positions; these are due to tunneled-through electrons from the neighboring sites. The effective exchange splitting is reduced so that the peaks are backshifted and appear at the same positions as for the isolated impurities.

According to Alexander-Anderson model, the exchange energies for two magnetic impurities in P-configuration and AP-configuration are[131, 132]:

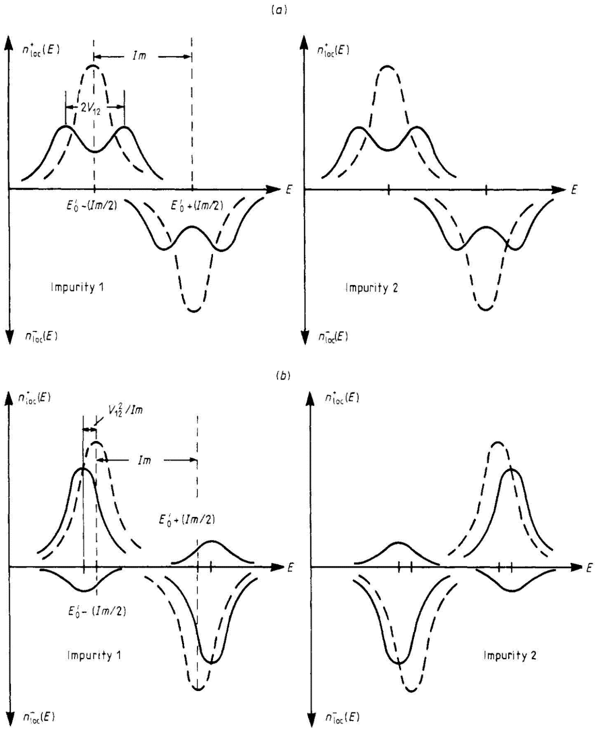

Figure 5.10: Schematic representation of the LDOS for the two configurations of a pair of magnetic impurities: (a) ferromagnetic configuration; (b) antiferromagnetic configuration. Full curves, LDOS of the pair; broken curves, LDOS of the single impurity. The figure is taken from [131].

$$\Delta E_F = -[n_l^{0+}(E_F) + n_l^{0-}(E_F)]V^2 \tag{5.1}$$

$$\Delta E_A = -2V^2/I \tag{5.2}$$

where $n_l^{0+}(E_F)$ is the local densities of states near the Fermi level, V is the overlap matrix element for two impurities on neighboring sites. Thus we can see that the ferromagnetic configuration is especially stable if the single impurity has a large LDOS at Fermi level, i.e. if one of the virtual bound states is located at the Fermi level. It is directly clear from Fig.5.10 (a) that then the bonding-antibonding splitting is quite effective in reducing the total energy. In contrast, ΔE_A is independent of the virtual bound-state positions and arises only from the covalent shift $\pm V^2/Im$. Therefore we expect the antiferromagnetic configuration to be stable if the peaks are away from the Fermi energy.

Our results are in line with the prediction of the Alexander-Anderson model[132]. The *d* states of the Cr adatom and the Cr tip-apex are plotted in Fig.5.11. The shape and the energy position of DOS for the adatom and the tip are strongly different from those for the isolated tip and the single adatom. Due to a strongly increased tip-adatom coupling, two additional peaks appear in majority states, at about -1 eV ($d_{xz,yz}$ and d_{z^2}) and 0.2 eV ($d_{xz,yz}$) with respect to the Fermi level. The intensity of the minority part of the adatom 3d states decreases because of the strong tip-adatom coupling. A small peak ($d_{xz,yz}$ and d_{z^2}) appears at about 0.8 eV below the Fermi level.

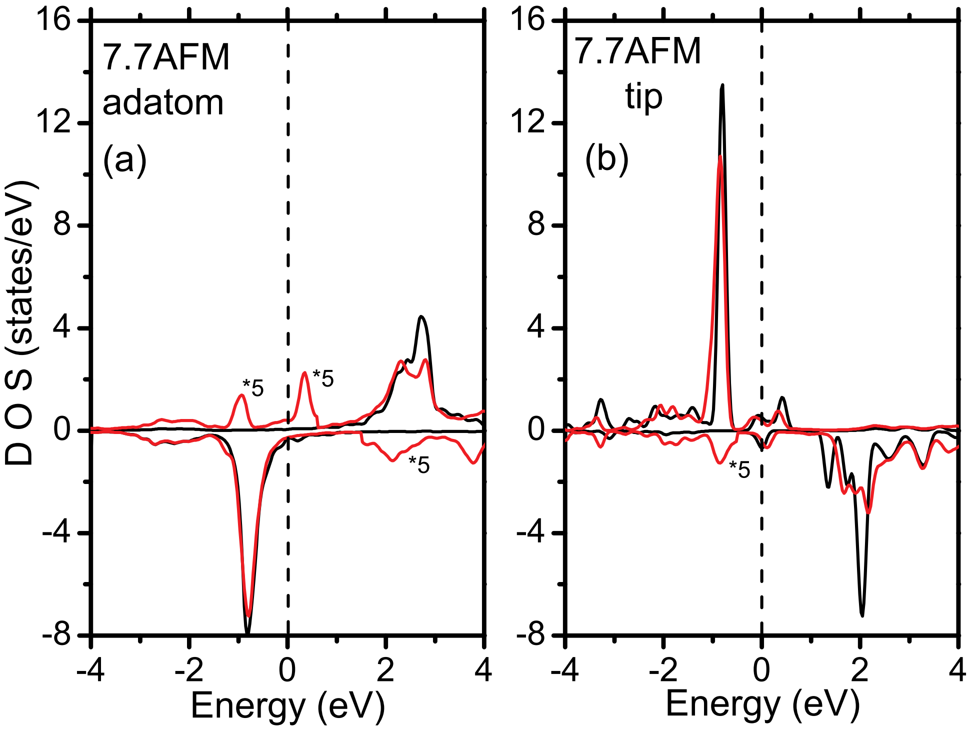

Figure 5.11: Density of states for the Cr adatom and the Cr tip-apex for the tip-substrate separation of 7.7 Å. 3d states of the adatom are plotted in (a). The black lines in the figure are the d states of a single Cr adatom on Cu(100) surface. The values of the majority in the range from -4.0 to 0.8 eV, and the minority in the range from 1.6 to 4 eV are scaled by factors 5. 3d states of the tip-apex are plotted in (b). The black lines in the figure are the d states of the Cr tip-apex in an isolated Cr tip. The values of the minority in the range from -4.0 to -0.5 eV are scaled by a factor 5.

We now analyze how a change of the spin alignment between the tip and the adatom from the P- to the AP-configuration affects the current. The zero bias transmission coefficients for the Cr tip and the Cr adatom at different tip-adatom distances D are presented in Fig. 5.12. The values for D go from 7.7 Å, where the AP-configuration has the lower energy, to 9.2 Å, where the P-configuration is the ground state, and where the ferromagnetic exchange energy is maximal (see Fig.5.4). We first note that the transmission is of the order of 1 for energies around the Fermi energy. This indicates that for the chosen separations the electron transfer rate is large, so that, indeed, a substantial interaction between tip and substrate can occur due to the conduction electrons. One can see that the increasing separation leads to a reduction of the transmission. Moreover the width of the high transmission region is reduced, which is due to the decrease of the hopping between the tip and the adatom with increasing D. The transmission around E_F is in the range of 1 to 2, which shows that more than one channel significantly contribute to the total transmission. One can clearly attribute the various peaks in the transmission to peaks in the PDOS, shown in Fig.

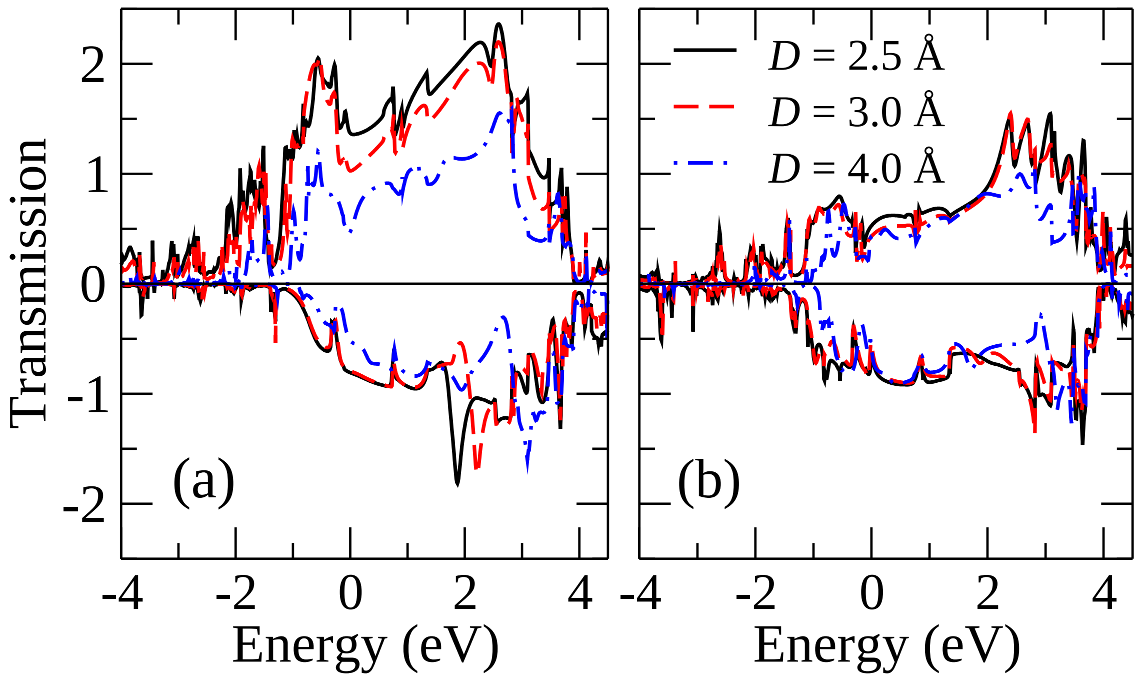

Figure 5.12: (Color online) Zero bias transmission coefficient for the Cr tip and the Cr adatom at different tip-adatom separations, D, for P (a) and AP alignment (b). Positive values are for majority spins, negative values for minority spins.

5.9. For $D = 2.5$ Å in the P configuration the majority transmission is significantly larger than the minority ones for energies up to E_F. This is due to the fact that whereas for the majority there are significant contributions to the DOS from s, p, and d electrons, for the minority spins the contributions from the p and d electrons are very small at these energies. The only available channel for the minority spin electrons is, therefore, the s channel, and this results in a smaller transmission. For $D = 4$ Å ,however the difference in transmission between P- and AP-transmission is much smaller. It indicates that the extended 4s states give the main contribution to the transmission for large separations. For energies up to about 4 eV above E_F the p orbitals also substantially contribute to the transmission. This analysis further supports our model of the double exchange coupling at large distances.

The AP transmission (Fig.5.12(b)) can approximately be seen as a convolution of the majority and minority transmissions. In this case, since the adatom and tip atom are both Cr atoms, it is approximately equal for majority and minority spins. For both spins the AP transmission around E_F is smaller than the one of the P majority spins, but it is larger than the one of the P minority spins. The total transmission for the P configuration is however larger than the one for the AP configuration, the difference becoming larger with decreasing D. Therefore a large magnetoresistance can be expected at small distances. The magnetoresistance ratio is defined as $R_{MR} = (I_P - I_{AP})/I_{AP}$, with $I_P(I_{AP})$ the current in the P- (AP-) configurations. At zero bias R_{MR} can be obtained from the transmission at E_F, and we obtain $R_{MR}(D = 7.7$ Å$) = 73\%$, $R_{MR}(D = 8.2$ Å$) = 64\%$, and $R_{MR}(D = 9.2$ Å$) = 3\%$. We also calculate R_{MR} for the short tip-adatom separation of 7.7Å by calculating the current for an applied bias of 0.2 V, for both the P and the AP configurations. Using the obtained currents we find $R_{MR} = 70\%$, in good agreement with the zero bias prediction. We note that the change of the resistance does not require external magnetic field.

Conclusions

In this work we have performed *ab initio* studies of the interaction of adatoms and molecules on metal surfaces with magnetic and nonmagnetic STM tips.

We have demonstrated that the electronic and magnetic properties of magnetic junctions consisting of 3d adatoms and a benzene molecule on metal surfaces can be tailored by the STM tip. Varying the tip-substrate distance the magnetic moment of adatoms can be manipulated. The physics behind this effect is related to atomic relaxation in the junctions caused by the interaction with the tip.

The effect of the STM tip on adatom diffusion is revealed. We have found that a relative location of the STM tip and the adatom can significantly affect an adatom migration. Our results for the Cu tip and the Co adatom on Cu(111) show that for some positions of the tip near the surface, the diffusion barrier for the Co adatom is strongly suppressed, and the jump of the adatom to the tip can occur. The direct interaction between the tip and the adatom is found to be a driving force for the adatom motion.

We have revealed the interplay between structural relaxations in single atom magnetic junctions and their electronic and magnetic properties. It is found that structural relaxations are of significant importance and determine the Kondo behavior of a single adatom for different tip-substrate separations.

Our *ab initio* studies show the possibility of controlling the spin direction of a single magnetic adatom on metal surfaces exploiting the magnetic STM tip. We reveal a strong dependence of the exchange interaction between the magnetic STM tip and the magnetic adatom on the tip-substrate distance. We have found that a direct interaction between d-states of the tip and the adatom at short tip-substrate separations leads to the antiferromagnetic coupling between the tip and the adatom, while at large distances an indirect interaction between d-states of the tip and the adatom via *sp* electrons leads to a ferromagnetic coupling between them. Based on the spin-dependent transport calculations, we find a magnetoresistance of about 70% at short tip-substrate distance.

Bibliography

[1] G. Binnig, H. Rohrer, Ch. Gerber, and E. Weibel. Tunneling through a controllable vacuum gap. *Applied Physics Letters*, 40(2):178–180, 1982.

[2] G. Binnig, H. Rohrer, Ch. Gerber, and E. Weibel. Surface studies by scanning tunneling microscopy. *Phys. Rev. Lett.*, 49(1):57–61, Jul 1982.

[3] R J Hamers. Atomic-resolution surface spectroscopy with the scanning tunneling microscope. *Annual Review of Physical Chemistry*, 40(1):531–559, 1989.

[4] J. Tersoff and D. R. Hamann. Theory of the scanning tunneling microscope. *Phys. Rev. B*, 31(2):805–813, Jan 1985.

[5] J. Bardeen. Tunnelling from a many-particle point of view. *Phys. Rev. Lett.*, 6(2):57–59, Jan 1961.

[6] C. F. Hirjibehedin, Ch-Y Lin, A. F. Otte, M Ternes, C. P. Lutz, B. A. Jones, and A. J. Heinrich. Large Magnetic Anisotropy of a Single Atomic Spin Embedded in a Surface Molecular Network. *Science*, 317(5842):1199–1203, 2007.

[7] D. M. Eigler and E. K. Schweizer. Positioning single atoms with a scanning tunnelling microscope. *Nature*, 344(6266):524–526, 1990.

[8] M. F. Crommie, C. P. Lutz, and D. M. Eigler. Imaging standing waves in a two-dimensional electron gas. *Nature*, 363(6429):524–527, 1993.

[9] L. Bartels, G. Meyer, and K.-H. Rieder. Basic steps of lateral manipulation of single atoms and diatomic clusters with a scanning tunneling microscope tip. *Phys. Rev. Lett.*, 79(4):697–700, Jul 1997.

[10] Ulrike Kurpick and Talat S. Rahman. Tip induced motion of adatoms on metal surfaces. *Phys. Rev. Lett.*, 83(14):2765–2768, Oct 1999.

[11] W. Chen, T. Jamneala, V. Madhavan, and M. F. Crommie. Disappearance of the kondo resonance for atomically fabricated cobalt dimers. *Phys. Rev. B*, 60(12):R8529–R8532, Sep 1999.

[12] X. Bouju, C. Joachim, and C. Girard. Single-atom motion during a lateral stm manipulation. *Phys. Rev. B*, 59(12):R7845–R7848, Mar 1999.

[13] H. C. Manoharan, C. P. Lutz, and D. M. Eigler. Quantum mirages formed by coherent projection of electronic structure. *Nature*, 403(6769):512–515, 2000.

[14] N. Nilius, T. M. Wallis, and W. Ho. Development of One-Dimensional Band Structure in Artificial Gold Chains. *Science*, 297(5588):1853–1856, 2002.

[15] S-W Hla and K-H Rieder. Stm control of chemical reactions: Single-molecule synthesis. *Annual Review of Physical Chemistry*, 54(1):307–330, 2003. PMID: 12626735.

[16] S-W Hla, K-F Braun, V. Iancu, and A Deshpande. Single-atom extraction by scanning tunneling microscope tip crash and nanoscale surface engineering. *Nano Letters*, 4(10):1997–2001, 2004.

[17] S-W Hla, K-F Braun, B. Wassermann, and K-H Rieder. Controlled low-temperature molecular manipulation of sexiphenyl molecules on ag(111) using scanning tunneling microscopy. *Phys. Rev. Lett.*, 93(20):208302, Nov 2004.

[18] J. A. Stroscio and R. J. Celotta. Controlling the Dynamics of a Single Atom in Lateral Atom Manipulation. *Science*, 306(5694):242–247, 2004.

[19] B. C. Stipe, M. A. Rezaei, and W Ho. Single-molecule vibtational spectroscopy and microscopy. *Science*, 280(0):1732–1735, 1998.

[20] J. K. Gimzewski and C. Joachim. Nanoscale Science of Single Molecules Using Local Probes. *Science*, 283(5408):1683–1688, 1999.

[21] A. Deshpande, H. Yildirim, A. Kara, D. P. Acharya, J. Vaughn, T. S. Rahman, and S.-W. Hla. Atom-by-atom extraction using the scanning tunneling microscope tip-cluster interaction. *Physical Review Letters*, 98(2):028304, 2007.

[22] H. J. Lee and W. Ho. Single-Bond Formation and Characterization with a Scanning Tunneling Microscope. *Science*, 286(5445):1719–1722, 1999.

[23] J. Weckesser, J. V. Barth, and K. Kern. Mobility and bonding transition of $c60$ on pd(110). *Phys. Rev. B*, 64(16):161403, Sep 2001.

[24] M. Abel, A. Dmitriev, R. Fasel, N. Lin, J. V. Barth, and K. Kern. Scanning tunneling microscopy and x-ray photoelectron diffraction investigation of $c60$ films on cu(100). *Phys. Rev. B*, 67(24):245407, Jun 2003.

[25] M. Böhringer, W. D. Schneider, R. Berndt, K. Glöckler, M. Sokolowski, and E. Umbach. Corrugation reversal in scanning tunneling microscope images of organic molecules. *Phys. Rev. B*, 57(7):4081–4087, Feb 1998.

[26] M. Böhringer, K. Morgenstern, W. D. Schneider, R. Berndt, F. Mauri, A. De Vita, and R. Car. Two-dimensional self-assembly of supramolecular clusters and chains. *Phys. Rev. Lett.*, 83(2):324–327, Jul 1999.

[27] X. Lu, M. Grobis, K. H. Khoo, Steven G. Louie, and M. F. Crommie. Spatially mapping the spectral density of a single $c60$ molecule. *Phys. Rev. Lett.*, 90(9):096802, Mar 2003.

[28] X. Lu, M. Grobis, K. H. Khoo, S. G. Louie, and M. F. Crommie. Charge transfer and screening in individual c[sub 60] molecules on metal substrates: A scanning tunneling spectroscopy and theoretical study. *Physical Review B*, 70(11):115418, 2004.

[29] N. Neel, J. Kroger, L. Limot, T. Frederiksen, M. Brandbyge, and R. Berndt. Controlled contact to a c60 molecule. *Physical Review Letters*, 98(6):065502, 2007.

[30] R. C. Jaklevic and J. Lambe. Molecular vibration spectra by electron tunneling. *Phys. Rev. Lett.*, 17(22):1139–1140, Nov 1966.

[31] Jun Kondo. Resistance minimum in dilute magnetic alloys. *Progress of Theoretical Physics*, 32(1):37–49, 1964.

[32] V. Madhavan, W. Chen, T. Jamneala, M. F. Crommie, and N. S. Wingreen. Tunneling into a Single Magnetic Atom: Spectroscopic Evidence of the Kondo Resonance. *Science*, 280(5363):567–569, 1998.

[33] J. Li, W.-D. Schneider, R. Berndt, and B. Delley. Kondo scattering observed at a single magnetic impurity. *Physical Review Letters*, 80(13):2893–2896, Mar 1998.

[34] O. Újsághy, J. Kroha, L. Szunyogh, and A. Zawadowski. Theory of the fano resonance in the stm tunneling density of states due to a single kondo impurity. *Phys. Rev. Lett.*, 85(12):2557–2560, Sep 2000.

[35] N. Knorr, M. A. Schneider, L. Diekhöner, P. Wahl, and K. Kern. Kondo effect of single co adatoms on cu surfaces. *Phys. Rev. Lett.*, 88(9):096804, Feb 2002.

[36] V. S. Stepanyuk, L. Niebergall, W. Hergert, and P. Bruno. Ab initio study of mirages and magnetic interactions in quantum corrals. *Physical Review Letters*, 94(18):187201, 2005.

[37] P. Wahl, P. Simon, L. Diekhoner, V. S. Stepanyuk, P. Bruno, M. A. Schneider, and K. Kern. Exchange interaction between single magnetic adatoms. *Physical Review Letters*, 98(5):056601, 2007.

[38] C. Jayaprakash, H. R. Krishna-murthy, and J. W. Wilkins. Two-impurity kondo problem. *Phys. Rev. Lett.*, 47(10):737–740, Sep 1981.

[39] P. Simon, R. Lopez, and Y. Oreg. Ruderman-kittel-kasuya-yosida and magnetic-field interactions in coupled kondo quantum dots. *Physical Review Letters*, 94(8):086602, 2005.

[40] T. Jamneala, V. Madhavan, and M. F. Crommie. Kondo response of a single antiferromagnetic chromium trimer. *Phys. Rev. Lett.*, 87(25):256804, Nov 2001.

[41] V. Iancu, A. Deshpande, and S-W Hla. Manipulating kondo temperature via single molecule switching. *Nano Letters*, 6(4):820–823, 2006.

[42] V. Iancu, A. Deshpande, and S-W Hla. Manipulation of the kondo effect via two-dimensional molecular assembly. *Physical Review Letters*, 97(26):266603, 2006.

[43] P. Wahl, L. Diekhoner, G. Wittich, L. Vitali, M. A. Schneider, and K. Kern. Kondo effect of molecular complexes at surfaces: Ligand control of the local spin coupling. *Physical Review Letters*, 95(16):166601, 2005.

[44] A. Zhao, Q. Li, L. Chen, H. Xiang, W. Wang, S. Pan, B. Wang, X. Xiao, J. Yang, J. G. Hou, and Q Zhu. Controlling the Kondo Effect of an Adsorbed Magnetic Ion Through Its Chemical Bonding. *Science*, 309(5740):1542–1544, 2005.

[45] L. Gao, W. Ji, Y. B. Hu, Z. H. Cheng, Z. T. Deng, Q. Liu, N. Jiang, X. Lin, W. Guo, S. X. Du, W. A. Hofer, X. C. Xie, and H.-J. Gao. Site-specific kondo effect at ambient temperatures in iron-based molecules. *Physical Review Letters*, 99(10):106402, 2007.

[46] L. Chen, Zh. Hu, A. Zhao, B. Wang, Y. Luo, J. Yang, and J. G. Hou. Mechanism for negative differential resistance in molecular electronic devices: Local orbital symmetry matching. *Physical Review Letters*, 99(14):146803, 2007.

[47] X. W. Tu, G. Mikaelian, and W. Ho. Controlling single-molecule negative differential resistance in a double-barrier tunnel junction. *Physical Review Letters*, 100(12):126807, 2008.

[48] Y. Fu, S. Ji, X. Chen, X. Ma, R. Wu, C. Wang, W. Duan, X. Qiu, B. Sun, P. Zhang, J. Jia, and Q Xue. Manipulating the kondo resonance through quantum size effects. *Physical Review Letters*, 99(25):256601, 2007.

[49] M. F. Crommie. Manipulating magnetism in a single molecule. *Science*, 309(5740):1501–1502, 2005.

[50] P. Hohenberg and W. Kohn. Inhomogeneous electron gas. *Phys. Rev.*, 136(3B):B864–B871, Nov 1964.

[51] W. Kohn and L. J. Sham. Self-consistent equations including exchange and correlation effects. *Phys. Rev.*, 140(4A):A1133–A1138, Nov 1965.

[52] Mel Levy. Universal variational functionals of electron densities, first-order density matrices, and natural spin-orbitals and solution of the v-representability problem. *Proceedings of the National Academy of Sciences of the United States of America*, 76(12):6062–6065, 1979.

[53] L. D. Landau and E. M. Lifshitz. *Theoretical Physics, Vol. 1, Mechanics.*

[54] L. Hedin and B. I. Lundqvist. Explicit local exchange-correlation potentials. *Journal of Physics C: Solid State Physics*, 4(14):2064–2083, 1971.

[55] U von Barth and L Hedin. A local exchange-correlation potential for the spin polarized case. i. *Journal of Physics C: Solid State Physics*, 5(13):1629–1642, 1972.

[56] V. L. Moruzzi, J. F. Janak, and A. R. Williams. *Calculated Electronic Properties of metals.* Pergamon, New York, 1978.

[57] S. H. Vosko, L. Wilk, and N. Nussair. Accurate spin-dependent electron liquid correlation energies for local spin density calculations: a critical analysis. *Can. J. Phys.*, 58(8):1200–1211, 1980.

[58] A. A. Katsnelson, V. S. Stepanyuk, A. Szasz, and O. V. Farberovich. *Computational Methods in Condensed Matter, Electronic Structure.* American Institute of Physics, New York, 1992.

[59] G. Kresse and J. Hafner. Ab initio molecular dynamics for open-shell transition metals. *Phys. Rev. B*, 48(17):13115–13118, Nov 1993.

[60] G. Kresse and J. Hafner. Ab initio molecular-dynamics simulation of the liquid-metal˘amorphous-semiconductor transition in germanium. *Phys. Rev. B*, 49(20):14251–14269, May 1994.

[61] G. Kresse and J. Furthmüller. Efficient iterative schemes for ab initio total-energy calculations using a plane-wave basis set. *Phys. Rev. B*, 54(16):11169–11186, Oct 1996.

[62] G. Kresse and J. Furthmüller. Efficiency of ab-initio total energy calculations for metals and semiconductors using a plane-wave basis set.

[63] David Vanderbilt. Soft self-consistent pseudopotentials in a generalized eigenvalue formalism. *Phys. Rev. B*, 41(11):7892–7895, Apr 1990.

[64] P. E. Blöchl. Projector augmented-wave method. *Phys. Rev. B*, 50(24):17953–17979, Dec 1994.

[65] E. G. Moroni, G. Kresse, J. Hafner, and J. Furthmüller. Ultrasoft pseudopotentials applied to magnetic fe, co, and ni: From atoms to solids. *Phys. Rev. B*, 56(24):15629–15646, Dec 1997.

[66] J. Hafner. Materials simulations using vasp–a quantum perspective to materials science. *Computer Physics Communications*, 177(1-2):6 – 13, 2007.

[67] J. M. Soler, E. Artacho, J. D. Gale, A. García, J. Junquera, P. Ordejón, and D. S. Portal. The siesta method for ab initio order-n materials simulation. *Journal of Physics: Condensed Matter*, 14(11):2745–2779, 2002.

[68] S. Huzinaga. *Gaussian Basis Sets for Molecular Calculations.* Elsevier Publishing Company, Amsterdam, 1991.

[69] N. Troullier and José Luriaas Martins. Efficient pseudopotentials for plane-wave calculations. *Phys. Rev. B*, 43(3):1993–2006, Jan 1991.

[70] Leonard Kleinman and D. M. Bylander. Efficacious form for model pseudopotentials. *Phys. Rev. Lett.*, 48(20):1425–1428, May 1982.

[71] O. F. Sankey and D. J. Niklewski. Ab initio multicenter tight-binding model for molecular-dynamics simulations and other applications in covalent systems. *Phys. Rev. B*, 40(6):3979–3995, Aug 1989.

[72] Andrew P. Horsfield. Efficient ab initio tight binding. *Phys. Rev. B*, 56(11):6594–6602, Sep 1997.

[73] D. Porezag, Th. Frauenheim, Th. Köhler, G. Seifert, and R. Kaschner. Construction of tight-binding-like potentials on the basis of density-functional theory: Application to carbon. *Phys. Rev. B*, 51(19):12947–12957, May 1995.

[74] C Elsasser, N Takeuchi, K M Ho, C T Chan, P Braun, and M Fahnle. Relativistic effects on ground state properties of 4d and 5d transition metals. *Journal of Physics: Condensed Matter*, 2(19):4371–4394, 1990.

[75] M. Wierzbowska, D. Sánchez-Portal, and S. Sanvito. Different origins of the ferromagnetic order in (ga,mn)as and (ga,mn) *n*. *Phys. Rev. B*, 70(23):235209, Dec 2004.

[76] C. D. Pemmaraju, R. Hanafin, T. Archer, H. B. Braun, and S. Sanvito. Impurity-ion pair induced high-temperature ferromagnetism in co-doped zno. *Physical Review B*, 78(5):054428, 2008.

[77] L. Fernández-Seivane, M. A. Oliveira, S. Sanvito, and J. Ferrer. On-site approximation for spin&ndash;orbit coupling in linear combination of atomic orbitals density functional methods. *Journal of Physics: Condensed Matter*, 18(34):7999–8013, 2006.

[78] M. Brandbyge, J. L. Mozos, P. Ordejón, J. Taylor, and K. Stokbro. Density-functional method for nonequilibrium electron transport. *Phys. Rev. B*, 65(16):165401, Mar 2002.

[79] A. R. Rocha, V. M. Garcia-Suarez, S. Bailey, C. Lambert, J. Ferrer, and S. Sanvito. Spin and molecular electronics in atomically generated orbital landscapes. *Physical Review B*, 73(8):085414, 2006.

[80] A. R. Rocha, V. M. Garcia-Suarez, S. Bailey, C. Lambert, J. Ferrer, and S. Sanvito. Spin and molecular electronics in atomically generated orbital landscapes. *Nature Materials)*, 4:335, 2005.

[81] Ivan Rungger and Stefano Sanvito. Algorithm for the construction of self-energies for electronic transport calculations based on singularity elimination and singular value decomposition. *Phys. Rev. B*, 78(3):035407, Jul 2008.

[82] S. Sanvito, C. J. Lambert, J. H. Jefferson, and A. M. Bratkovsky. General green's-function formalism for transport calculations with *spd* hamiltonians and giant magnetoresistance in co- and ni-based magnetic multilayers. *Phys. Rev. B*, 59(18):11936–11948, May 1999.

[83] Yigal Meir and Ned S. Wingreen. Landauer formula for the current through an interacting electron region. *Phys. Rev. Lett.*, 68(16):2512–2515, Apr 1992.

[84] F Cyrot-Lackmann. Sur le calcul de la cohsion et de la tension superficielle des mtaux de transition par une mthode de liaisons fortes. *Journal of Physics and Chemistry of Solids*, 29(7):1235 – 1243, 1968.

[85] F. Cyrot-Lackmann. On the calculation of surface tension in transition metals. *Surface Science*, 15:535–548, 1969.

[86] J. Friedel. Metallic alloys. *Il Nuovo Cimento (1955-1965)*, 7(0):287–311, Sep 1958. 10.1007/BF02751483.

[87] V. S. Stepanyuk, D. I. Bazhanov, A. N. Baranov, W. Hergert, P. H. Dederichs, and J. Kirschner. Strain relief and island shape evolution in heteroepitaxial metal growth. *Physical Review B*, 62(23):15398–15401, Dec 2000.

[88] V. S. Stepanyuk, D. I. Bazhanov, W. Hergert, and J. Kirschner. Strain and adatom motion on mesoscopic islands. *Physical Review B*, 63(15):153406, Mar 2001.

[89] O. V. Lysenko, V. S. Stepanyuk, W. Hergert, and J. Kirschner. Mesoscopic relaxation in homoepitaxial metal growth. *Physical Review Letters*, 89(12):126102, Aug 2002.

[90] N. N. Negulyaev, V. S. Stepanyuk, P. Bruno, L. Diekhöner, P. Wahl, and K. Kern. Bilayer growth of nanoscale co islands on cu(111). *Physical Review B*, 77(12):125437, 2008.

[91] N. N. Negulyaev, V. S. Stepanyuk, W. Hergert, P. Bruno, and J. Kirschner. Atomic-scale self-organization of fe nanostripes on stepped cu(111) surfaces: Molecular dynamics and kinetic monte carlo simulations. *Physical Review B*, 77(8):085430, 2008.

[92] A. L. Klavsyuk W. Hergert V. S. Stepanyuk S. Pick, P. A. Ignatiev and P. Bruno. Structure and magnetic properties of co chains on a stepped cu surface. *Journal of Physics: Condensed Matter*, 19(44):446001 (11pp), 2007.

[93] O. Mironets, H. L. Meyerheim, C. Tusche, V. S. Stepanyuk, E. Soyka, P. Zschack, H. Hong, N. Jeutter, R. Felici, and J. Kirschner. Direct evidence for mesoscopic relaxations in cobalt nanoislands on cu(001). *Physical Review Letters*, 100(9):096103, 2008.

[94] R. Pandey, B. K. Rao, P. Jena, and John M. Newsam. Unique magnetic signature of transition metal atoms supported on benzene. *Chemical Physics Letters*, 321(1-2):142 – 150, 2000.

[95] V. V. Maslyuk, A. Bagrets, V. Meded, A. Arnold, F. Evers, M. Brandbyge, T. Bredow, and I. Mertig. Organometallic benzene-vanadium wire: A one-dimensional half-metallic ferromagnet. *Physical Review Letters*, 97(9):097201, 2006.

[96] H. Xiang, J. Yang, J. G. Hou, and Q. Zhu. One-dimensional transition metal-benzene sandwich polymers: Possible ideal conductors for spin transport. *Journal of the American Chemical Society*, 128(7):2310–2314, 2006.

[97] K. M. Wedderburn, S. Bililign, M. Levy, and R. J. Gdanitz. Geometries and stabilities of 3d-transition metal-cation benzene complexes, m+bzn (m=sc-cu, n=1, 2). *Chemical Physics*, 326(2-3):600 – 604, 2006.

[98] G. Bihlmayer S. Blügel Y. Mokrousov, N. Atodiresei. Magnetic anisotropy energies of metal-benzene sandwiches. *International Journal of Quantum Chemistry*, 106(15):3208–3213, 2006.

[99] H. Sevincli, M. Topsakal, E. Durgun, and S. Ciraci. Electronic and magnetic properties of 3d transition-metal atom adsorbed graphene and graphene nanoribbons. *Physical Review B*, 77(19):195434, 2008.

[100] Kevin T. Chan, J. B. Neaton, and Marvin L. Cohen. First-principles study of metal adatom adsorption on graphene. *Physical Review B*, 77(23):235430, 2008.

[101] K. S. Novoselov, A. K. Geim, S. V. Morozov, D. Jiang, Y. Zhang, S. V. Dubonos, I. V. Grigorieva, and A. A. Firsov. Electric Field Effect in Atomically Thin Carbon Films. *Science*, 306(5696):666–669, 2004.

[102] L. Gross, K-H. Rieder, F. Moresco, S. M. Stojkovic, A. Gourdon, and C. Joachim. Trapping and moving metal atoms with a six-leg molecule. *Nat Mater*, 4:892–895, 2005.

[103] N. Atodiresei, V. Caciuc, S. Blugel, and H. Holscher. Manipulation of benzene on cu(110) by dynamic force microscopy: An ab initio study. *Physical Review B*, 77(15):153408, 2008.

[104] N. Lorente, M. F. G. Hedouin, R. E. Palmer, and M. Persson. Chemisorption of benzene and stm dehydrogenation products on cu(100). *Phys. Rev. B*, 68(15):155401, Oct 2003.

[105] P. Lang, V. S. Stepanyuk, K. Wildberger, R. Zeller, and P. H. Dederichs. Local moments of 3d, 4d, and 5d atoms at cu and ag (001) surfaces. *Solid State Communications*, 92(9):755 – 759, 1994.

[106] K.-F. Braun, V. Iancu, N. Pertaya, K.-H. Rieder, and S.-W. Hla. Decompositional incommensurate growth of ferrocene molecules on a au(111) surface. *Physical Review Letters*, 96(24):246102, 2006.

[107] Y. Yayon, V. W. Brar, L. Senapati, S. C. Erwin, and M. F. Crommie. Observing spin polarization of individual magnetic adatoms. *Physical Review Letters*, 99(6):067202, 2007.

[108] R. Z. Huang, V. S. Stepanyuk, A. L. Klavsyuk, W. Hergert, P. Bruno, and J. Kirschner. Atomic relaxations and magnetic states in a single-atom tunneling junction. *Physical Review B*, 73(15):153404, 2006.

[109] N. Neel, J. Kroger, L. Limot, K. Palotas, W. A. Hofer, and R. Berndt. Conductance and kondo effect in a controlled single-atom contact. *Physical Review Letters*, 98(1):016801, 2007.

[110] W. A. Hofer, A. S. Foster, and A. L. Shluger. Theories of scanning probe microscopes at the atomic scale. *Rev. Mod. Phys.*, 75(4):1287–1331, Oct 2003.

[111] S. Heinze, M. Bode, A. Kubetzka, O. Pietzsch, X. Nie, S. Blugel, and R. Wiesendanger. Real-Space Imaging of Two-Dimensional Antiferromagnetism on the Atomic Scale. *Science*, 288(5472):1805–1808, 2000.

[112] J. Wintterlin, J. Wiechers, H. Brune, T. Gritsch, H. Höfer, and R. J. Behm. Atomic-resolution imaging of close-packed metal surfaces by scanning tunneling microscopy. *Phys. Rev. Lett.*, 62(1):59–62, Jan 1989.

[113] P. Wahl, L. Diekhöner, M. A. Schneider, L. Vitali, G. Wittich, and K. Kern. Kondo temperature of magnetic impurities at surfaces. *Phys. Rev. Lett.*, 93(17):176603, Oct 2004.

[114] L. Vitali, R. Ohmann, S. Stepanow, P. Gambardella, K. Tao, R. Z. Huang, V. S. Stepanyuk, P. Bruno, and K. Kern. Kondo effect in single atom contacts: The importance of the atomic geometry. *Physical Review Letters*, 101(21):216802, 2008.

[115] U. Fano. Effects of configuration interaction on intensities and phase shifts. *Phys. Rev.*, 124(6):1866–1878, Dec 1961.

[116] N. A. Levanov, V. S. Stepanyuk, W. Hergert, D. I. Bazhanov, P. H. Dederichs, A. Katsnelson, and C. Massobrio. Energetics of co adatoms on the cu(001) surface. *Phys. Rev. B*, 61(3):2230–2234, Jan 2000.

[117] P. W. Anderson. Localized magnetic states in metals. *Phys. Rev.*, 124(1):41–53, Oct 1961.

[118] H. Yildirim, A. Kara, and T. S. Rahman. Tip-induced adatom extraction and cluster manipulation. *Physical Review B (Condensed Matter and Materials Physics)*, 75(20):205409, 2007.

[119] M. R. Sørensen, K. W. Jacobsen, and H. Jónsson. Thermal diffusion processes in metal-tip-surface interactions: Contact formation and adatom mobility. *Phys. Rev. Lett.*, 77(25):5067–5070, Dec 1996.

[120] R. Z. Huang, V. S. Stepanyuk, and J. Kirschner. Interaction of scanning tunneling microscopy tip with mesoscopic islands at the atomic-scale. *Journal of Physics: Condensed Matter*, 18(17):L217–L223, 2006.

[121] V. S. Stepanyuk, D. I. Bazhanov, W. Hergert, and J. Kirschner. Strain and adatom motion on mesoscopic islands. *Phys. Rev. B*, 63(15):153406, Mar 2001.

[122] O. V. Lysenko, V. S. Stepanyuk, W. Hergert, and J. Kirschner. Mesoscopic relaxation in homoepitaxial metal growth. *Phys. Rev. Lett.*, 89(12):126102, Aug 2002.

[123] K. Wildberger, V. S. Stepanyuk, P. Lang, R. Zeller, and P. H. Dederichs. Magnetic nanostructures: 4 d clusters on ag(001). *Phys. Rev. Lett.*, 75(3):509–512, Jul 1995.

[124] V. S. Stepanyuk, L. Niebergall, R. C. Longo, W. Hergert, and P. Bruno. Magnetic nanostructures stabilized by surface-state electrons. *Phys. Rev. B*, 70(7):075414, Aug 2004.

[125] Cyrus F. Hirjibehedin, Christopher P. Lutz, and Andreas J. Heinrich. Spin Coupling in Engineered Atomic Structures. *Science*, 312(5776):1021–1024, 2006.

[126] B. W. Heinrich, C. Iacovita, M. V. Rastei, L. Limot, J. P. Bucher, P. A. Ignatiev, V. S. Stepanyuk, and P. Bruno. Spin structure of an atomic protrusion: Probing single atoms on cobalt nanoislands. *Phys. Rev. B*, 79(11):113401, Mar 2009.

[127] A. J. Heinrich, J. A. Gupta, C. P. Lutz, and D. M. Eigler. Single-Atom Spin-Flip Spectroscopy. *Science*, 306(5695):466–469, 2004.

[128] A. Kubetzka, M. Bode, O. Pietzsch, and R. Wiesendanger. Spin-polarized scanning tunneling microscopy with antiferromagnetic probe tips. *Phys. Rev. Lett.*, 88(5):057201, Jan 2002.

[129] C. Zener. Interaction between the d shells in the transition metals. *Phys. Rev.*, 81(3):440–444, Feb 1951.

[130] C. Zener. Interaction between the d-shells in the transition metals. ii. ferromagnetic compounds of manganese with perovskite structure. *Phys. Rev.*, 82(3):403–405, May 1951.

[131] A Oswald, R Zeller, P J Braspenning, and P H Dederichs. Interaction of magnetic impurities in cu and ag. *Journal of Physics F: Metal Physics*, 15(1):193–212, 1985.

[132] S. Alexander and P. W. Anderson. Interaction between localized states in metals. *Phys. Rev.*, 133(6A):A1594–A1603, Mar 1964.

Acknowledgments

I do not know how to start to thank my supervisor Prof. Dr. V.S. Stepanyuk. A whole chapter would not enough. He cared about my studies in every detail and offered nice and efficient suggestions. His great enthusiasm and deep insight in physics and numerous intensive discussions always encourage and help me a lot whenever I encounter any difficulty. Without his support, this work would not appear.

I would like to express my gratitude to Prof. Dr. P. Bruno for his valuable criticism and suggestion I have got during the seminars and discussions.

Many thanks to Prof. Dr. I. Mertig from Martin-Luther-University and her coworkers V.V. Maslyuk. I benefit a lot from the fruitful collaboration with the group of Prof Mertig.

I wish to acknowledge Prof. Dr. K. Kern from MPI-FKF from Stuttgart and his coworkers Dr. L. Vitali, R. Ohmann, Dr. S. Stepanow and Dr. P. Gambardella. The fruitful collaborations with experimental group led by Prof K. Kern broadened my view in science.

Special thanks to Dr. R.Z. Huang, P. Ignatiev, Dr. L. Niebergall, Dr. N. Negulyaev, O. Brovko, Dr. D.I. Bazhanov for their help. I feel deep grateful to our system administrator U. Schmidt and our secretary I. Goffin for their patience and kind help.

I wish to thank Dr. M. Kaempfe and all friends in International Max Planck Research School. We had a lot of hot discussion and experienced unforgettable three years.

I would like to thank my parents, my brothers and my wife Li Xie.

Veröffentlichungen

Teile der vorliegenden Arbeit wurden an folgenden Stellen veröffentlicht:

1. L. Vitali, R. Ohmann, S. Stepanow, P. Gambardella, K. Tao, R. Huang, V. S. Stepanyuk, P. Bruno, and K. Kern
   Kondo Effect in Single Atom Contacts: The Importance of the Atomic Geometry
   Physical Review Letters **101**, 216802 (2008).

2. K. Tao, V. S. Stepanyuk, P. Bruno, D. I. Bazhanov, V. V. Maslyuk, M. Brandbyge, and I. Mertig
   Manipulating magnetism and conductance of an adatom-molecule junction on a metal surface: An ab initio study
   Physical Review B **78**, 014426 (2008)

Tabellarischer Lebenslauf
Kun Tao

Persönliche Daten

Name, Vorname:	Tao, Kun
Geburtsdatum:	4.8.1976
Geburtsort:	Huainan, Provinz Anhui (China)
Nationalität:	Chinesisch
Wohnort:	06120 Halle, Heideallee 8
Familienstand:	ledig

Ausbildung und Qualifikation

7/1992-9/1995	Mittelschule Nr.2 Huainan, Provinz Anhui, China
9/1995-7/1998	Physikdepartament, Huainan Normal College, Provinz Anhui, China
9/2002 -3/2005	Physikstudium, University of Shanghai for Science and Technology, Shanghai, China Abschluss Master of Science
seit 1/2006	Promotionsstudium im Rahmen der International Max Planck Research School for Science and Technology, Halle

Berufsweg

7/1998-9/2002	Lehramt für Physik, Mittelschule Nr.10 Huainan, Provinz Anhui, China
3/2005-12/2005	Versuchsassistent, University of Shanghai for Science and Technology, Shanghai, China

Dienstanschrift

Max-Planck-Institut fr Mikrostrukturphysik
Weinberg 2
D-06120 Halle (Saale)
Tel.: +345 5582613
Email: ktao@mpi-halle.mpg.de

Halle (Saale), April 28, 2010 (Kun Tao)

Erklärung

Ich versichere hiermit, die vorliegende Dissertation

Interaction of the STM tip with adatoms and molecules on metal surfaces: ab initio studies

selbständig und ohne fremde Hilfe verfasst und keine anderen als die von mir angegebenen Quellen und Hilfsmittel verwendet zu haben. Den benutzten Werken wörtlich oder inhaltlich entnommene Stellen sind als solche gekennzeichnet.

Halle (Saale), April 28, 2010 (Kun Tao)

Erklärung

Ich versichere hiermit, dass ich mich an keiner wissenschaftlichen Hochschule im Geltungsbereich des deutschen Grundgesetzes bereits früher um den Doktorgrad beworben habe.

Halle (Saale), April 28, 2010 (Kun Tao)